DOE/ER/40363--T3

Electromagnetic Dissociation of Relativistic ^{28}Si by Nucleon Emission

DOE/ER/40363--T3

DE93 008670

by

Upul Jayasiri Sonnadara

B.Sc. University of Colombo, 1985

M.Sc. University of Pittsburgh, 1990

FG02-87ER40363

Submitted to the Graduate Faculty of
Arts and Sciences in partial fulfillment
of the requirements for the degree of
Doctor of Philosophy

University of Pittsburgh

December 1992

Abstract

Electromagnetic Dissociation of Relativistic ^{28}Si by Nucleon Emission

Upul J. Sonnadara
University of Pittsburgh
November 1992

A detailed study of the electromagnetic dissociation of ^{28}Si by nucleon emission at E_{lab}/A = 14.6 GeV/nucleon was carried out with ^{28}Si beams interacting on ^{208}Pb, ^{120}Sn, ^{64}Cu, ^{27}Al and ^{12}C targets. The measurements were made in the fixed target relativistic heavy ion experiment E814 operating at the Brookhaven National Laboratory. The E814 apparatus consists of detectors in the target area which measure the energy and charged multiplicity, and a forward spectrometer which measures the position, momentum and energy of the reaction fragments.

The exclusive electromagnetic dissociation cross sections for decay channels having multiple nucleons in the final state have been measured with the aid of the E814 apparatus which enables the selection of events produced in pure electromagnetic interactions. The measured cross sections agree well with previous measurements obtained for the removal of a few nucleons with the E814 apparatus as well as with measurements on total charge removal cross sections from other experiments. The dependence of the integrated cross sections on the target charge Z_T and the target mass A_T confirms that for higher Z targets the excitation is largely electromagnetic.

Direct measurements of the excitation energy for the electromagnetic dissociation of ^{28}Si $\rightarrow$ p+^{27}Al and ^{28}Si $\rightarrow$ n+^{27}Si have been obtained through a calculation of the invariant mass in kinematically reconstructed events. The excitation energy spectrum for all targets peak near the isovector giant dipole resonance in ^{28}Si. These distributions are well reproduced by combining the photon spectrum calculated using the Weizsäcker-Williams approximation with the experimental data on the photonuclear reactions ^{28}Si(γ,p)^{27}Al and ^{28}Si(γ,n)^{27}Si.

The possibilities of observing double giant dipole resonance excitations in ^{28}Si have been investigated with cross section measurements as well as with excitation energy reconstruction. Effects due to the surviving peripheral nuclear interactions and the contribution from double interactions on experimental observations are discussed.

To my parents

Gilbert and Karunawathie Sonnadara

Acknowledgments

I would like to express my gratitude to my thesis supervisor Bill Cleland for his guidance and support throughout my graduate student career.

My special thanks to David Kraus who inspired me in many ways as a second supervisor, Helio Takai and Marcia Takagui for their friendship and collaboration on the development of the peripheral analysis techniques, and, Tom Joyce and Brian Lopresti for their work on various software developments.

I would like to thank Bo Yu, Tom Hemmick and Ed O'Brien for their work on the tracking chambers, and, Tom Throwe and Sean McCorkle for their help concerning the data acquisition and data analysis software problems.

I appreciate all the support given by my friends Kithsiri Jayananda, Zhing Zhi Zhang, Murugesu Yoganathan, Arjuna Parakrama, and Sergei Voloshin. I owe much to my wife Romaine Sonnadara for her love and encouragement.

Finally, I wish to express my gratitude to Peter Braun-Munzinger and David Lissauer for their leadership in the experiment E814, and to all the members of the E814 collaboration who made this experiment a success.

Upul J. Sonnadara

TABLE OF CONTENTS

1 Introduction **1**

A Relativistic Heavy-ion Collisions 1

B Electromagnetic Dissociation 3

1 Equivalent Photon Method 3

2 Multipole Theory 6

3 Multi-photon Excitations 8

C Scope of the Thesis 10

2 The Experiment **12**

A Overview of the Experiment 12

1 Physics Programs 12

2 Detectors 13

3 Trigger 17

4 Data Acquisition System 18

B Detectors used in EMD studies 20

1 Forward Scintillators 20

2 U/Cu Calorimeters 23

3 Tracking Chambers 25

3 Detector Studies **29**

A Forward Scintillators 29

1 Noise Corrections 29

2 Charge Measurement 31

3 Saturation Effects 32

4 Time of flight 33

5 Position Measurement 35

B U/Cu Calorimeters 36

1 PM gain drifts 36

2 Noise corrections 37

3 Cluster Finding 38

4 Position Measurement 39

5 Energy Resolution 40

6 Shower Fluctuations 41

C Tracking Chambers 42

1 Pad Section 42
2 Drift Section 46

4 Selection of Electromagnetic Interactions **51**
A Online Selection 51
1 Peripheral Trigger 51
2 Scalers 53
3 Data Sample 53
B Offline Selection 54
1 Good Beam Selection 55
2 Data Selection 57
C Cross Sections for Simple Channels 62
1 Event Characterization 62
2 Cross Section estimates 64

5 Reconstruction of Events **69**
A Track Reconstruction 69
1 Preliminary Selection 69
2 Pattern Recognition in Drift Chambers 71
3 Tracking Details 74
B Reconstruction Studies 76
1 Method of Reconstruction 76
2 Application to Peripheral Events 78
3 Results 82

6 Analysis of Complex Channels **85**
A Cross Section Measurements 85
1 P/Z by Drift Chambers 85
2 Event Classification 86
3 Results 88
B Interpretation of the Data 92
1 Z and A Dependence 92
2 Double Photon Excitations 94
3 Background to the Double Photon Excitation Process 95
C Excitation Energy Reconstructions 97
1 Single Nucleon Emission 97
2 Comparison with Low Energy Data 104

7 Conclusions **108**

LIST OF FIGURES

1.1 Collision between two relativistic heavy ions. 2
1.2 Electromagnetic dissociation. 3
1.3 Photo-absorption cross section of the ^{28}Si nucleus. The virtual photon spectrum generated by the WW approximation for three different beam energies are also shown for comparison. Ref [6] . . 5
1.4 The charge dependence of the EMD cross section for different beam energies. The curves represent the theoretical calculations under the WW approximation. Ref [6] 6
1.5 Effect of photon multipolarities at different beam energies. Ref [6] 8
1.6 Measured excitation energy of the $^{16}O \rightarrow 1p + ^{15}N$ reaction. Ref [22] 11

2.1 Diagram of the E814 apparatus. The beam enters through an aperture in the back of the target calorimeter. Forward going particles pass through the participant calorimeter opening and the two magnets M1 and M2. Track positions are measured in the tracking chambers DC1, DC2 and DC3. Charge is measured in the forward scintillators and energy is measured in the Target calorimeter, the Participant calorimeter and the U/Cu calorimeters. The top two figures show a blowup of the target region detectors. 14
2.2 A block diagram of the E814 trigger system. 18
2.3 A block diagram of the E814 data acquisition system. 19
2.4 A forward scintillator slat. 22
2.5 A U/Cu calorimeter module. Ref [44] 24
2.6 The E814 tracking chambers. (a) A view of the pad chamber DC1 showing the locations of the anode wires and field wires. (b) A view of the drift chamber DC2 (and DC3) showing the chevron pad plane and the drift region. Ref [46] 27

3.1 Noise in forward scintillators. (a) Effect due to the 60Hz ripple. (b) Cross-talk between nearest neighbors. 30
3.2 Measured pulse height in upstream forward scintillators for minimum ionizing particles. 32
3.3 Effect of scintillator saturation. (a) Pulse height in Si downstream vs. measured pulse height in a scintillator. (b) Same after correcting for the scintillator saturation. 34

3.4 Effect due to slewing for time measurement. (a) Pulse height vs. time. (b) 1/sqrt(PH) vs. time demonstrating a linear relationship. 35
3.5 Pitt photomultiplier test facility with data acquisition setup. . . . 37
3.6 Gain drifts in two hamamatsu photomultiplier tubes. 38
3.7 The measured raw energy distributions. (a) Protons. (b) Neutrons. 39
3.8 Position dependence on measured energy. (a) Position vs. energy. (b) Corrected energy distribution. 40
3.9 Shower fluctuations. (a) Maximum cell energy vs. the total energy. (b) Energy after correcting for the fluctuations. 42
3.10 DC1 event display showing two common problems induced by the heavy ions passing through the chamber. (a) Negative signal shift along anode wire. (b) Two δ rays emerging from a heavy ion cluster. Ref [55] 43
3.11 Charge ratio plot. (a) Heavy ions. (b) Protons. 45
3.12 DC1 resolution in the x position measurement. (a) Beam vertex measurement extrapolated to the DC1 plane vs. the DC1 x measurement. (b) The difference between the two measurements. . . . 45
3.13 Measured y position resolution by chevron pads (a) Difference between the DC1 measurement extrapolated to the DC2 plane, and the DC2 position measurement. (b) Same for DC3. 47
3.14 Average TDC hit distributions in drift planes in DC2. (a) Raw distribution. (b) Distribution after cleaning by a comparison with pad hits. 48
3.15 Equipotential and field lines for drift cells used in DC2 and DC3 chambers. Ref [55] 49
3.16 Non linearity in drift time measurement. (a) Track location vs. drift time for DC2. (b) Same for DC3. 49

4.1 Beam scintillator system. (a) Pileup effect in veto counter S1. (b) Same for S3. (c) Pulse height in S1 vs. time after previous beam particle. (d) The average pulse height measurement by S2 and S4. 56
4.2 Silicon upstream detector. (a) Pulse height vs. time after previous beam particle. (b) Pulse height measurement with time after previous beam cut. 57
4.3 Silicon downstream detector. (a) Pulse height vs. time after previous beam particle. (b) Pulse height measurement with time after previous beam cut. 58
4.4 Triple charge measurement. (a) Pulse height in FSCI vs. pulse height in HSCI. (b) Double charge measurement by FSCI and HSCI. (c) Silicon downstream detector vs. double charge. (d) Triple charge measurement by combining all three measurements. 59

4.5 EMD event selection. (a) Energy measured in the PCAL for non-interacting beam events (solid line) and normal peripheral events (dashed line). (b) Same for TCAL. 60
4.6 Charge selection. (a) Measured heavy ion charge for Z=14, Z=13 and Z=12 fragments. (b) The total charge measured in the upstream FSCI. 63
4.7 Energy selection. (a) Energy in the proton calorimeter vs. the neutron calorimeter for Z=13 and Z=14 events. (b) Proton calorimeter energy for selected 1p events with Z=13 and cut on neutron energy. 64
4.8 Measured position of the heavy ion fragments at the downstream horizontal counter for selected channels. 65

5.1 Two bend magnet model used in the preliminary analysis. 71
5.2 Accuracy of the DC1 hit selection. (a) Difference between the predicted and measured heavy ion positions. (b) Same for protons. . 72
5.3 Measured sums of drift times in neighboring anode wires for protons. (a) DC2. (b) DC3. 73
5.4 Second TDC hit vs. the first TDC hit. (a) All hits. (b) Selected hits. 74
5.5 Resolution in the drift chamber DC2 (a) Heavy ions (b) Protons. . 76
5.6 Reconstructed momentum distribution for beam particles. 77
5.7 Selected geometrical parameters for the two body decay. 79
5.8 Effect of multiple scattering. 81

6.1 P/Z reconstruction. (a) Selected Z=13 events. (b) Charge vs. P/Z for different decay channels. 86
6.2 Selection of multi nucleon events. (a) Energy in neutron calorimeters vs. P/Z. (b) Energy in proton calorimeters for selected Z=11 events (solid curve) and selected Z=11 with cuts on neutron energy and the P/Z (dashed curve). 87
6.3 Second charge measurement at the downstream end of the spectrometer. (a) *d* channels. (b) α channels. 88
6.4 Efficiency of limited acceptance arising from the second charge measurement. Plots show the estimated efficiency variations for excitation energies up to 20 MeV. Each curve represents a specific decay channel having (a) *d* and (b) α particle in the final state. 89
6.5 (a) Exclusive cross section vs. Q value of the reaction. (b) Total charge changing cross sections. 92
6.6 Z and A dependence of EMD cross sections for the $^{28}Si \rightarrow {}^{27}Al +$ 1p reaction. Solid curve represents the 3 parameter fit discussed in the text. Contributions of the extracted electromagnetic (dashed) and nuclear (dotted) components are also shown. 93

6.7 Selected nuclear events. (a) Measured energy in PCAL for missing neutrons. (b) Estimated cross sections. Dashed and dotted lines represent the expected behavior for a pure nuclear dependence. . . 94
6.8 (a) Z dependence of cross sections extracted by the three parameter fit discussed in the text. (b) Ratio of nuclear and EMD components for different decay channels obtained with a fixed exponent. 96
6.9 Reconstructed raw excitation energy spectra for 4 different targets. The arrows indicate the kinematic thresholds for each reaction. (a) 1p events. (b) 1n events. 98
6.10 Decay angular distributions for reconstructed 1p events taken with a Pb target. The angles are the (a) polar (b) azimuthal center-of-mass angles of the ^{27}Al ion. 99
6.11 Ratio of excitation energy spectra for (a) Pb/Sn and (b) Pb/Al. Two dotted lines indicate the expected ratios for pure nuclear and pure electromagnetic dependence. Dashed lines represent the theoretical ratio obtained by the WW method. 100
6.12 Estimated cross section distribution of the surviving nuclear induced component of the cross section for the C target, obtained by subtracting the raw Pb data, scaled by a factor $(Z_C/Z_{Pb})^{1.8}$, from the C data. 102
6.13 Nuclear component subtracted excitation energy spectra for reconstructed 1p events taken with 4 targets. The solid curves are obtained from (γ, p) experimental data multiplied by the WW spectrum and simulated through our apparatus. The arrows indicate the kinematic threshold of the reaction. 103
6.14 Monte Carlo simulation of the measured excitation energy distribution (solid curve) and the true excitation energy distribution (dashed curve), obtained by adding the energy of the decay photon to the measured energy. The calculation is for Pb target. 105
6.15 Excitation energy for 1n decay (closed circles). The solid curve represents the (γ, n) multiplied by the WW spectrum and convoluted with our experimental resolution. Arrows indicate the kinematic thresholds. 106
6.16 (a) Excitation energy distributions of 1p, 1n and 2p decay. (b) Sum of the three distributions compared with (γ.abs) spectra. 107

LIST OF TABLES

1.1 Comparison of the measured (σ_{EXP}) and calculated ($\sigma_{W\cdot W\cdot}$) semi-inclusive cross sections at 14.6 GeV/nucleon beam energy. 5
1.2 Calculated cross sections for a single neutron emission from ^{197}Au projectiles on ^{197}Au targets for different beam energies. Here σ_T represents the sum of the cross sections σ_{E1} and σ_{E2}. 9
1.3 Calculated cross sections for multiple photon absorptions. 10

3.1 The extracted parameters A and B using Birk's parametrization for a set of scintillator materials 33

4.1 List of parallel triggers with their downscaling factors. 53
4.2 List of magnetic tapes written for each target and each trigger type. 54
4.3 List of cuts used in EMD selection. The events which produce energy and multiplicity below the values listed here for each detector were taken as good peripheral events. 61
4.4 Estimated efficiency in the offline selection procedure for selecting events produced by the electromagnetic interactions for various targets. 61
4.5 List of cuts used to select 1p and 1n events. These cuts were imposed on selected EMD event samples. The upstream charge sum was calibrated to place the minimum ionizing particles at 100 units. 63
4.6 List of efficiencies for the cuts used to select 1p and 1n events. These efficiency factors can be considered as independent of each other. 67
4.7 List of targets and their properties. 68
4.8 Measured cross sections for 1p and 1n emission by EMD. For comparison, earlier cross section measurements through our experiment are also listed. 68

5.1 List of offset constants extracted by the alignment studies. 75
5.2 History of the event reconstruction code (GRIST) used in this analysis. 78
5.3 Reconstruction resolution for 1p events. 83
5.4 Reconstruction resolution for 1n events. 84

6.1 Estimated efficiencies for selection of multi nucleon events. 90

6.2 Measured exclusive EMD cross sections for channels having neutrons and protons in the final state. The listed errors are only statistical. 90
6.3 Measured exclusive EMD cross sections for channels having d and α in the final state (in addition to the neutrons and protons). Listed errors are only statistical. 91
6.4 Extracted exponents by a 3 parameter fit. 95
6.5 Estimated double scattering contribution on the cross sections. Here, c_{old} and c_{new} represents the old and new (after correcting the cross sections for the double scattering) exponents. 97
6.6 Values of the cross section parameters C_k found in the final fit to the data taken with Pb, Sn, Cu, Al and C targets. 104
6.7 Integrated cross sections in the interval 16.0 to 26.0 MeV. The errors for the simulation are deduced from the available $^{28}Si(\gamma,p)^{27}Al$ photo-absoption cross sections which are used as the input. Errors on the data are statistical. 106

CHAPTER 1

Introduction

The acceleration of atomic nuclei to ultra-relativistic energies in recent years has made possible studies of electromagnetic dissociation (EMD) using the virtual photon field of the target nucleus [1-5]. An important advantage of this technique over the experiments using real photons on a target at rest is that the decay products are given large energies through the Lorentz boost, so that they can be identified and measured. In experiment E814, operating at the AGS at Brookhaven National Laboratory, we have seen the full spectrum of decays of ^{28}Si by this method [31]. This thesis describes the measurement of absolute cross sections, and the complete kinematic reconstruction of a few of these decay channels.

A Relativistic Heavy-ion Collisions

The nucleus-nucleus collisions occur mainly through either the strong or the electromagnetic interactions. At relativistic energies, these two interactions can be classified according to the the distance between the colliding nuclei. [1] Figure 1.1 shows an interaction between a projectile nucleus A_P and a target nucleus A_T. The nucleons which undergo inelastic scattering are called participants and the nucleons which do not participate in the collision are called spectators. The impact parameter plays an important role in deciding the ratio between participants and spectators in any given collision. We can separate the interactions into two major classes, namely those with $b < R_P + R_T$ and those with $b > R_P + R_T$. In the collisions with $b < R_P + R_T$, the overlapping nucleons undergo inelastic collisions and the remains of the projectile move forward essentially undisturbed (nuclear fragmentation). The highest degree of centrality in this case could be achieved when $b = 0$ where a maximum number of nucleons will undergo inelastic collisions (central collisions). The collisions with $b > R_P + R_T$ occur mainly via electromagnetic interactions (peripheral collisions).

The peripheral collisions between two heavy ions can occur via two scattering mechanisms, namely Coulomb scattering, which is the interaction of the projectile with the electromagnetic field of the target nucleus, and hadronic scattering, which is the interaction of the projectile and the target either through nucleus-nucleus in-

[1] impact parameter b

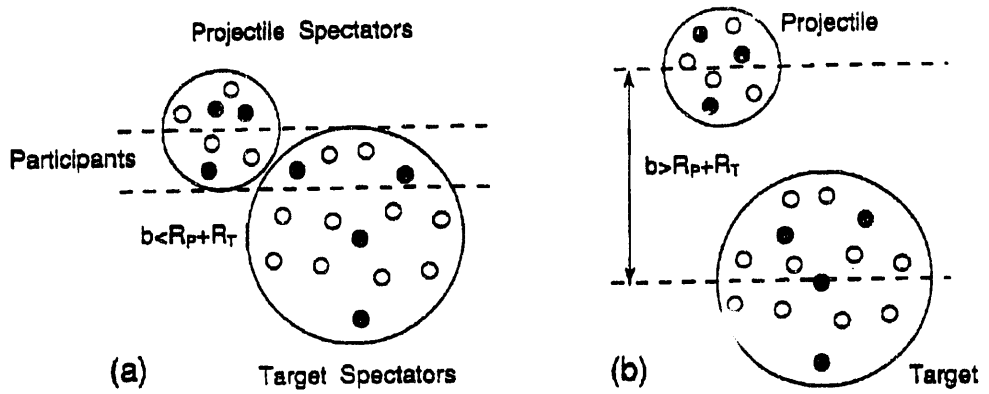

Figure 1.1: Collision between two relativistic heavy ions.

teraction (elastic scattering of the projectile by the target as a whole) or through nucleon-nucleon interaction (inelastic scattering by the individual nucleons at the surface of the colliding nuclei). Both the coulomb and the hadronic scattering can induce excitations in the colliding nuclei, which will decay by emitting either a γ ray or a few nucleons. The differential cross sections of the peripheral heavy ion scattering can be written in the form [6, 7],

$$\frac{d\sigma}{d\Omega} = |f_{coul}(\theta) + f_{had}(\theta)|^2 + \frac{d\sigma_{inel}}{d\Omega}$$

where $f_{coul}(\theta)$ and $f_{had}(\theta)$ are the coulomb and the hadronic elastic scattering amplitudes for the nucleus as a whole and $d\sigma_{inel}/d\Omega$ is the inelastic or quasi-elastic scattering of the individual nucleons at the surface of the colliding nuclei.

The coulomb scattering amplitude for ultra-relativistic energy collisions with heavy ions can exceed the pure geometrical cross section by several orders of magnitude. In addition, at very low momentum transfer collisions, the coulomb scattering becomes the most dominant term, and thus could be used as an experimental tool to select candidates for electromagnetic interactions. The theoretical models behind coulomb scattering will be discussed in more detail in the following section.

The hadronic scattering amplitude, in the presence of a strong coulomb interaction can be described by the behavior of light scattering through a small aperture or the light scattered by a black disk, which has the characteristics of the Fresnel diffraction pattern [8]. This has been observed in heavy ion collisions at low beam energies ranging from a few MeV and extending up to relativistic energies.

The inelastic hadronic scattering of nucleons at the surface of the two colliding nuclei usually induces nuclear fragmentation. This has been observed in nucleon-nucleus (pA) scattering experiments at various beam energies [9].

B Electromagnetic Dissociation

1 Equivalent Photon Method

The equivalent photon method [11] can be considered as the simplest way to describe the reaction mechanism of electromagnetic interactions in relativistic collisions. In the literature, this method is well known as the Weizsäcker-Williams method (WW). A complete description of WW can be found in the textbook of Jackson on classical electrodynamics [10].

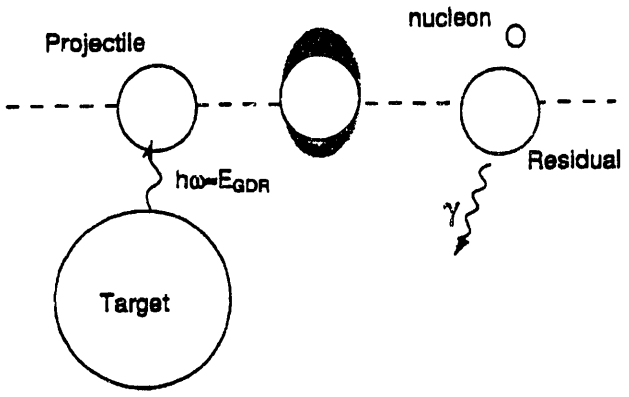

Figure 1.2: Electromagnetic dissociation.

Consider the example shown in Figure 1.2 of a projectile interacting with a target electromagnetic field. In the WW approximation, the target electromagnetic field can be replaced by a flux of virtual photons, and therefore this interaction is equivalent to the absorption of photons by the projectile. For simplicity, the absorption of a single photon is considered. One should notice that the target and the projectile can be interchanged through a Lorentz transformation. The projectile, which contains the excess energy of the absorbed photon, will eventually decay by emitting either a γ ray or a nucleon. The EMD cross section in the WW approximation can be given by

$$\sigma_{EMD} = \int_0^\infty n(\omega)\sigma(\omega)\frac{d\omega}{\omega}$$

where ω is the virtual photon frequency, $n(\omega)$ is the virtual photon flux integrated over all the impact parameters at a given photon energy and $\sigma(\omega)$ is the photonuclear cross section which can be found in the literature [12, 13, 14]. It can be shown that in a collision with impact parameter b, the virtual photon spectrum contains photons with energies up to a maximum value given by $E_\gamma^{max} \approx \gamma(\hbar c/b_{min})$, implying that for a given impact parameter, only excitations up to a certain value can be reached. The virtual photon flux, integrated over all the impact parameters is given by [11],

$$n(\omega) = \frac{2}{\pi} Z_T^2 \alpha \left[\frac{c}{v}\right]^2 \left(\xi K_0(\xi)K_1(\xi) - \frac{v^2\xi^2}{2c^2}\left[K_1(\xi)^2 - K_0(\xi)^2\right]\right) \qquad (1.1)$$

where Z_T is the target charge, $\xi = \omega b_{min}/\gamma v$, $\alpha = e^2/\hbar c$ is the fine structure constant, $K_0(\xi)$ and $K_1(\xi)$ are the modified Bessel functions, and v and γ are the projectile velocity and the Lorentz factor respectively. The value of b_{min} for the coulomb excitation can be taken as the sum of the nuclear radii $R_T + R_P$.

At higher energies where $\gamma >> 1$, it is useful to rewrite the virtual photon spectrum as [11],

$$n(\omega) = \frac{2Z_T^2\alpha}{\pi} \ln\left[\frac{\delta\gamma v}{\omega b_{min}}\right]$$

where $\delta = 0.681$. This simple formula can be used for most practical purposes. It can be seen that the virtual photon spectrum has a simple scaling of $\ln(\gamma)$ and $\ln(1/b_{min})$, both of which modify the naive expectation of Z_T^2 dependance.

Figure 1.3 shows the experimentally measured photo-absorption cross section of the ^{28}Si nucleus as a function of the photon energy [6]. The spectrum shows the response of the nucleus to the photons for energies between 10 MeV and 500 MeV. The peak at 20 MeV corresponds to the excitation of the Giant Dipole Resonance in ^{28}Si. The Giant Dipole resonance arises from an oscillation of the protons with respect to the neutrons in the nucleus. The predicted energy for such oscillations corresponds to $E_{GDR} = 76/A^{1/3}$ MeV for a nucleus with mass A and has been observed experimentally for various light and heavy nuclei. This resonance can be stimulated by photons with wavelengths comparable to the dimensions of the nucleus. The second peak at 300 MeV corresponds to the excitation of the Δ resonance in the nucleus. The region in between the resonances is the quasi-deuteron region. In this region, a dipole consisting of a proton and a neutron, responds to the photon wavelength, which exceeds the dimensions of a single nucleon [6]. For comparison, the virtual photon spectrum generated for three beam momenta is also shown in the same figure for the case in which a ^{28}Si projectile interacts with the electromagnetic field of a ^{208}Pb target. It can be seen from this plot that the AGS energy of 14.6 GeV/nucleon is well suited for the study of the GDR in ^{28}Si. At CERN, the energy of 200 GeV/nucleon creates a photon spectrum which populates other resonance states which can compete with the GDR, while the Bevalac energy of 2.1 GeV/nucleon produces a spectrum which falls quite rapidly over the resonance region.

The early comparisons between the theoretical calculations of the electromagnetic dissociation cross sections obtained from the WW approximation and the experimentally measured cross sections obtained at the Bevalac indicated several discrepancies. This was explained as a difficulty in subtracting the nuclear component from the electromagnetic cross sections [15]. The measurements of the exclusive cross section of ^{28}Si decaying into specific channels containing up to several nucleons were published for the first time by the E814 collaboration [31]. The experimental technique used in the E814 collaboration was quite immune to the nuclear background and the values obtained agreed well with theoretical cross sections. Table 1.1 shows the results obtained by Norbury [16] for semi-inclusive cross sections, compared with the E814

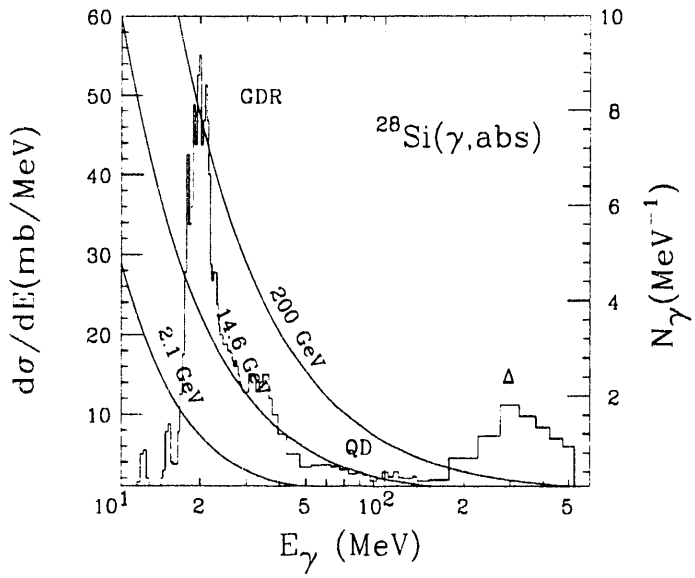

Figure 1.3: Photo-absorption cross section of the ^{28}Si nucleus. The virtual photon spectrum generated by the WW approximation for three different beam energies are also shown for comparison. Ref [6]

measurements. The uncertainties in the theoretical calculations arise from the measured uncertainties in the photo-nuclear data used in the calculation. The agreement between the theoretical calculations and the experimental measurements is not good for the Al target. This could be due to the effect of the nuclear component which can make a substantial contribution to the measured cross sections for low Z targets. The other significant feature in these data is that the neutron cross sections are higher and the proton cross sections are lower than the theoretical calculations (except for the Al target).

Table 1.1: Comparison of the measured (σ_{EXP}) and calculated (σ_{WW}) semi-inclusive cross sections at 14.6 GeV/nucleon beam energy.

Projectile	Target	Final State	$\sigma_{EXP}(mb)$	σ_{WW} (mb)
Si	Al	1p	37 ± 5	24 ± 2
Si	Al	1n	15 ± 4	9 ± 1
Si	Sn	1p	313 ± 4	317 ± 32
Si	Sn	1n	136 ± 6	118 ± 12
Si	Pb	1p	746 ± 27	806 ± 81
Si	Pb	1n	347 ± 18	301 ± 30

The charge dependence of EMD cross sections in heavy ion reactions has been

investigated by Lissauer and Takai [18]. It has been shown that the Z_T^N dependence observed at the Bevalac with N=1.4 could be explained as a consequence of an "apparent" charge distribution. The apparent charge distribution in this context defines the special region where the projectile and the target interact only through EM forces. Figure 1.4 shows the measured Z dependence of EM cross sections for beam energies ranging from roughly 1 GeV/nucleon to about 200 GeV/nucleon. The dashed lines in the figure correspond to their calculations for the expected N dependence for three different minimum impact parameter values. It is clear from this plot that most of the observed deviations are consistent within the WW approximation.

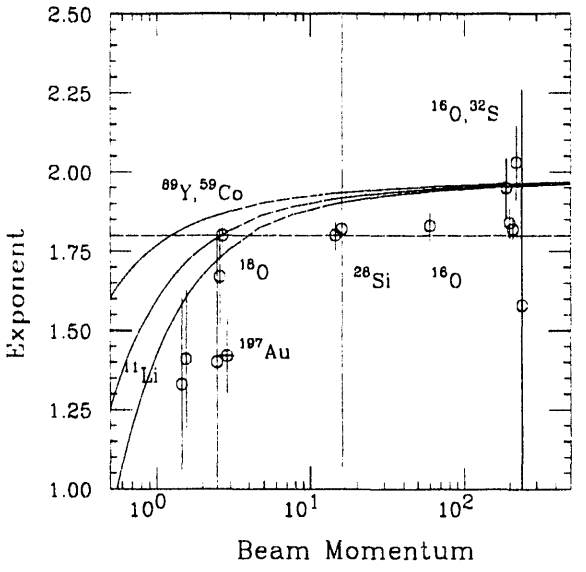

Figure 1.4: The charge dependence of the EMD cross section for different beam energies. The curves represent the theoretical calculations under the WW approximation. Ref [6]

2 Multipole Theory

The WW approximation is a very useful approximation used to understand electromagnetic processes. However, it breaks down in the regime of 100 MeV/nucleon energy due to the assumptions made in the derivation. The availability of new experimental measurements suggests the need for a theoretical model which can be used for a wide range of energies and all nuclei.

The virtual photon spectra consists of photons of different multipolarities. These multipolarities can be quite important at different beam momenta for the excitation of the GDR. An accurate theoretical analysis which involves the decomposition of the virtual photon spectra into its components was carried out by Bertulani and Baur [11]. These studies show that the analytical form of the WW essentially corresponds to

photons of electric dipole (E1) multipolarity. Other important multipolarities include the electric quadruple (E2) and the Magnetic dipole (M1). However, it can be shown that at higher momenta, only one component, namely E1, is dominant.

The most important contributions to the cross section come from E1 and E2. We can write the EMD cross section for the one photon exchange as,

$$\sigma_{EMD} = \int [n_{E1}(\omega)\sigma_{E1}(\omega) + n_{E2}(\omega)\sigma_{E2}(\omega)] \frac{d\omega}{\omega}$$

where $\sigma_{E1}(\omega)$ and $\sigma_{E2}(\omega)$ are the photo-nuclear reaction cross sections for the electric dipole and electric quadruple resonances respectively. The quadrupole resonance consists of two modes, namely, the isoscalar and the isovector. The isoscalar resonance has not been observed with most of the light nuclei [6]. The E1 photon spectra is equal to the analytical form of the WW spectrum $n(\omega)$ given earlier in equation 1.1. The analytical form of the E2 spectra is given by [11]

$$n_{E2}(\omega) = \frac{2Z_T^2\alpha}{\pi\beta^4}\left[2(1-\beta^2)K_1^2 + \xi(2-\beta^2)^2 K_0 K_1 - \frac{\xi^2\beta^4}{2}(K_1^2 - K_0^2)\right] \qquad (1.2)$$

For a crude estimate of the response of the nucleus to the different multi-polarities, we can factor the $n_{Ei}(\omega)$ out of the integral and evaluate them at a single energy and use the sum rules [11] to evaluate $\int(\sigma_{Ei}(\omega)/\omega)d\omega$. This allows us to rewrite the equation as a function of the projectile mass and charge,

$$\sigma_{EMD} = 60\frac{n_{E1}(\omega_1)}{\omega_1}\frac{NZ}{A} + 0.22\times 10^{-3} n_{E2}(\omega_2)\omega_2 Z A^{2/3} \qquad (mb)$$

where ω_1 and ω_2 are the energies for the Dipole and the Quadrupole resonances respectively.

Figure 1.5 shows the contributions of E1 and E2 to the total EMD cross section as a function of the beam momentum. We can neglect the contributions from E2 at higher beam energies. But at low energies, the contribution can be as high as 50%. The reason for the failure of the WW at low energies where E2 is important can be shown by very simple arguments [11]. The E1 photons originate from the contraction of the target electric field. The higher the beam momentum, the higher the photon intensity due to the Lorentz contraction. The E2 photons originate from the non-uniformity of the field lines caused by the finite dimension of the projectile. Although this increases with the beam momentum, once the electric field lines are contracted and are in the plane perpendicular to the beam direction, the intensity remains almost constant.

A more accurate calculation of E1 and E2 has been performed by Norbury [16, 17] by using the experimental photonuclear cross sections for $\sigma_{E1}(\omega)$ and theoretical predictions for $\sigma_{E2}(\omega)$, and numerically evaluating the integral without removing the energy dependence of the photon spectra. The results, which are summarized

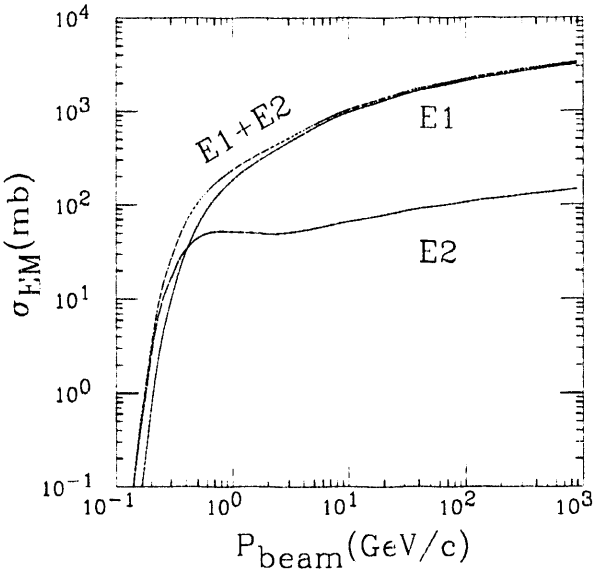

Figure 1.5: Effect of photon multipolarities at different beam energies. Ref [6]

in Table 1.2, indicate that above 10 GeV/nucleon, the WW approximation can be used successfully. The difference between the two ratios given in the table, arises essentially from the difference in the photonuclear cross section contributions used in the evaluation of σ_{WW} and σ_{E1}. These results clearly indicate the importance of the E2 contribution at beam energies below 2 GeV/nucleon.

3 Multi-photon Excitations

So far, due to its simplicity, the discussion has been limited to the absorption of a single photon. However, we can discuss the possibility of the absorption of more than one photon by the projectile (interaction with the same target nucleus) within the WW picture. This is formulated by Bertulani and Baur [11] and many others in the harmonic oscillator approximation where multiple photon excitation is treated as the multiple excitation of a pure harmonic oscillator. In the harmonic oscillator approximation, the differential cross section for the absorption of one photon of energy E^* is given by [19, 20],

$$\frac{d\sigma_1}{dE^*} = \int 2\pi b\, db\, \epsilon^{-m_\gamma(b)} \phi(E^*, b)$$

with

$$m_\gamma(b) = \int dE_\gamma N(E_\gamma, b)\sigma_\gamma(E_\gamma) = \int dE_\gamma \phi(E_\gamma, b)$$

Table 1.2: Calculated cross sections for a single neutron emission from ^{197}Au projectiles on ^{197}Au targets for different beam energies. Here σ_T represents the sum of the cross sections σ_{E1} and σ_{E2}.

Beam Energy	σ_{WW} (b)	σ_{E1} (b)	σ_{E2} (b)	σ_{WW}/σ_T	σ_{E1}/σ_T
100 MeV	0.56	0.53	0.83	41%	39%
300 MeV	1.7	1.6	0.8	71%	67%
500 MeV	2.3	2.2	0.7	79%	76%
2.1 GeV	4.9	4.7	0.6	92%	89%
12 GeV (AGS)	11.1	10.8	0.7	97%	94%
60 GeV (CERN)	19.3	18.7	1.0	98%	95%
200 GeV (CERN)	25.5	24.7	1.1	99%	96%
200 GeV (RHIC)	49.5	48.1	1.4	100%	97%

and

$$N(E_\gamma, b) = \frac{Z_T^2 \alpha}{\pi^2} \left(\frac{E_\gamma}{\hbar\gamma v}\right)^2 \left[\frac{c}{v}\right]^2 \left(K_1^2(\xi) + \frac{1}{\gamma^2} K_0^2(\xi)\right)$$

where $\sigma_\gamma(E_\gamma)$ is the total photo-absorption cross section, $\phi(E_\gamma, b) = N(E_\gamma, b)\sigma_\gamma(E_\gamma)$, and the probability of the absorption of a single photon of any energy with a given impact parameter b is $P_N(b) = (1/N!)m_\gamma^N(b)\epsilon^{-m_\gamma(b)}$. Similarly, the differential cross section for the absorption of two photons is,

$$\frac{d\sigma_2}{dE^*} = \frac{1}{2!} \int 2\pi b\, db\, \epsilon^{-m_\gamma(b)} \int dE_1 \phi(E_1, b)\phi(E^* - E_1, b)$$

The total cross section for the EMD upto two photon excitation is given by,

$$\sigma = \int dE^* \left[\frac{d\sigma_1}{dE^*} + \frac{d\sigma_2}{dE^*}\right]$$

These calculations can be extended to calculate the cross sections due to the absorption of any number of photons quite easily. Table 1.3 shows the results obtained by this method for multiple photon absorption up to 4 photon numbers [19, 20]. The experimental difficulty in observing a double GDR over a single GDR by measuring the total integrated cross sections is clear at this point since the double GDR cross sections are less than 1% of the single GDR cross sections. Conclusive experimental evidence of the existence of DGDR in electromagnetic dissociation has not been found yet. However, recent measurements with heavy projectiles (such as ^{136}Xe) indicate the possibility of observing DGDR in electromagnetic dissociation [21].

Table 1.3: Calculated cross sections for multiple photon absorptions.

Photon Number	^{16}O on ^{238}U at 100 GeV/nucleon	^{32}S on ^{238}U at 100 GeV/nucleon
1	2.5 b	4.3 b
2	20.6 mb	46.3 mb
3	328 μb	1.1 mb
4	4.8 μb	26.6 μb

C Scope of the Thesis

The original E814 proposal was submitted to the Brookhaven National Laboratory AGS committee in 1985 [25]. The main objectives of the peripheral collision program included the measurement of exclusive cross sections of electromagnetic dissociation channels up to several nucleons and the reconstruction of the excitation energy absorbed by the projectile when interacting with the target electromagnetic field. These measurements are necessary to test the theories behind the electromagnetic interactions. The scope of this thesis can be summarized as one step in achieving these goals.

During the intervening years, several experiments have reported valuable experimental measurements of the electromagnetic dissociation [1-5]. The first cross section measurements of the E814 results were published in 1990 [31], and there the dependence on Z_T and A_T was discussed. These cross sections show good agreement with the convolution of the WW spectrum with the experimental photonuclear cross sections. Other experiments also reported a similar dependence. However, satisfactory experimental observations of excitation energy measurements, which can provide invaluable information about the shape of the virtual photon spectrum, were not available until recently. Even today, only two measurements are available. The first report made by Olsen et al. [22] for the $^{16}O \rightarrow 1p + {}^{15}N$ system is shown in Figure 1.6 at 2.1 GeV/nucleon energy. The peak at 9 MeV is due to the transitions to the ground state of the residual ^{15}N. The second peak which is about 5 MeV below the first peak is due to the transitions to the first excited state of ^{15}N which is in coincidence with 4 MeV γ rays corresponding to the de-excitation of the ^{15}N nucleus. The second measurement [32], reported for $^{28}Si \rightarrow 1p + {}^{27}Al$ .. 14.6 GeV/nucleon was a result of part of the work described in this thesis and will be explained here in detail.

The GDR in various nuclei has been studied through photonuclear reactions with a higher precision than that which can be achieved through high energy heavy ion reactions. However, at relativistic energies the properties of excited projectiles can be measured with a resolution that is good enough to probe their structure. In addition, heavy ion collisions can be useful in measuring the two photon excitation cross sections which are relatively small compared to single photon excitation cross

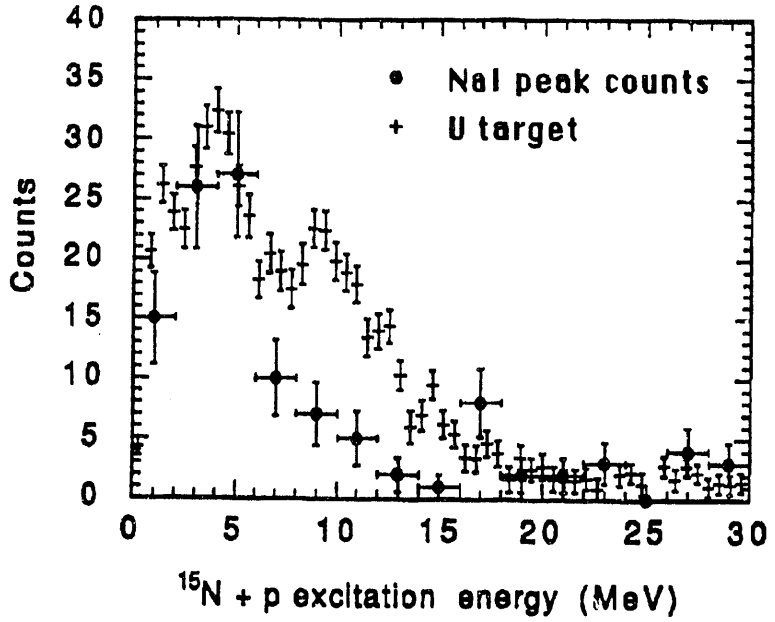

Figure 1.6: Measured excitation energy of the ^{16}O — 1p + ^{15}N reaction. Ref [22]

sections. This DGDR excitation mechanism can lead to new physics and even the production of new exotic nuclei [6].

The signatures of DGDR can be searched either through exclusive cross section measurements or by full excitation energy reconstruction, the latter being more promising. Bearing this in mind, the goals of the thesis were extended in both directions. As a result, new exclusive cross sections up to 5 nucleons in the final state including α and d particles were measured. In addition to the studies carried out with the 1p+^{27}Al channel, the excitation energy reconstruction of 1n+^{27}Si and 2p+^{26}Mg channels were carried out successfully. Although the two channels 1p+1n+^{26}Al and 2n+^{26}Si can be reconstructed using the methods discussed here, limited statistics discouraged us from carrying it out. However, the three reconstructed channels account for almost 70% of the total EMD cross section and hence permit useful comparisons with the $^{28}Si(\gamma, abs)$ data [23].

CHAPTER 2

The Experiment

Experiment E814 is a fixed target Relativistic Heavy-ion experiment operating in the Alternating Gradient Synchrotron (AGS) at Brookhaven National Laboratory. The collaboration of the experiment consists of about 50 physicists from ten different institutions. After the test runs in May 1987 and June 1988, data were taken in December 1988, June 1989, June 1990 and March 1991 with 14.6 GeV/nucleon ^{28}Si beams. The Peripheral Collisions program operated from 1988 to 1990 and results from the 1988 data were published [31]. Data from 1989 were used to study detector performances and other systematic effects. Data analyzed in this thesis were taken in 1990 with approximately 7 days of beam.

A Overview of the Experiment

1 Physics Programs

The original physics programs in E814 extend from the investigation of the properties of exotic nuclear systems produced by large impact parameter collisions to a study of energy flow and transparency by transition from large impact parameter collisions to small impact parameter collisions [25]. The program was later extended to study the properties of beam rapidity protons and neutrons (forward baryons) and to a search of strange matter which can form under high baryon densities and temperatures [26]. A description of the major programs operated during the last few years to study a broad range of topics in physics is given below.

1.1 Central Collisions

At AGS energies of 14.6 GeV/nucleon, small impact parameter collisions can produce higher hadronic densities which lead to new physical phenomena. Understanding of the reaction mechanisms possibly lead to the formation and evolution of new phases such as Quark Gluon Plasma [24]. However, even if a new state of matter is not found, systematic studies of stopping power and transparency will improve our understanding of nuclear-nuclear collisions. We measured the energy flow and the charged particle multiplicity, and their correlation with the forward baryons, with the data taken

during the 1988 and 1990 runs [28, 29, 30]. Analysis of the 1991 data is still in progress.

1.2 Peripheral Collisions

The fragmentation of the projectile in large impact parameter collisions can be initiated by either the nuclear or the coulomb field of the target nucleus. These two processes can be distinguished by their dependence on the target mass and charge. The interaction of the projectile with the electromagnetic field of the target can be explained by the absorption of virtual photons [10, 11]. At AGS energies, the virtual photon flux is strong enough to produce multi photon excitations or even bound or quasi-bound multi-neutron states. With the E814 apparatus, exclusive cross section measurements as well as excitation energy measurements [31, 32, 33] can be done on channels which are very difficult to measure in low energy photo-absorption studies.

1.3 Strangelet Search

The high baryon rich matter can produce meta-stable or even stable exotic objects like strangelets which consist of up, down and strange quarks. Compared to normal matter, strangelets are heavier (mass number > 10 and Z/A range between 0.1 to 0.3) and have lifetimes in the order of 100 nsecs which are detectable in our spectrometer. The existence of strangelets could be important in verifying the existence of Quark Gluon Plasma since the Quark Gluon Plasma can be cooled down to form strangelets [34]. With the 1988 and 1989 data, we were able to set upper limits to light and heavy strangelet productions [35], and we expect to improve the limits with the analysis of data from the 1991 run. This program was later extended to measure particles that are composed of produced quarks such as $\bar{p}$ and $\bar{d}$ [36].

2 Detectors

The experimental setup used in June 1990 is shown in Figure 2.1. The coordinate system used in the experiment is defined by a right handed system with z along the incident beam direction and y vertical (upward). The detectors in the experiment consist of a beam telescope, a set of detectors in the target area to measure the energy and charged multiplicity and a set of detectors in the forward spectrometer to measure the position, energy and momentum of the final state particles. The two dipole magnets M1 and M2 which provide the deflection for the spectrometer, separate the detectors into two groups, namely the upstream detector group and the downstream detector group. A brief description of the detectors in these two groups are given below.

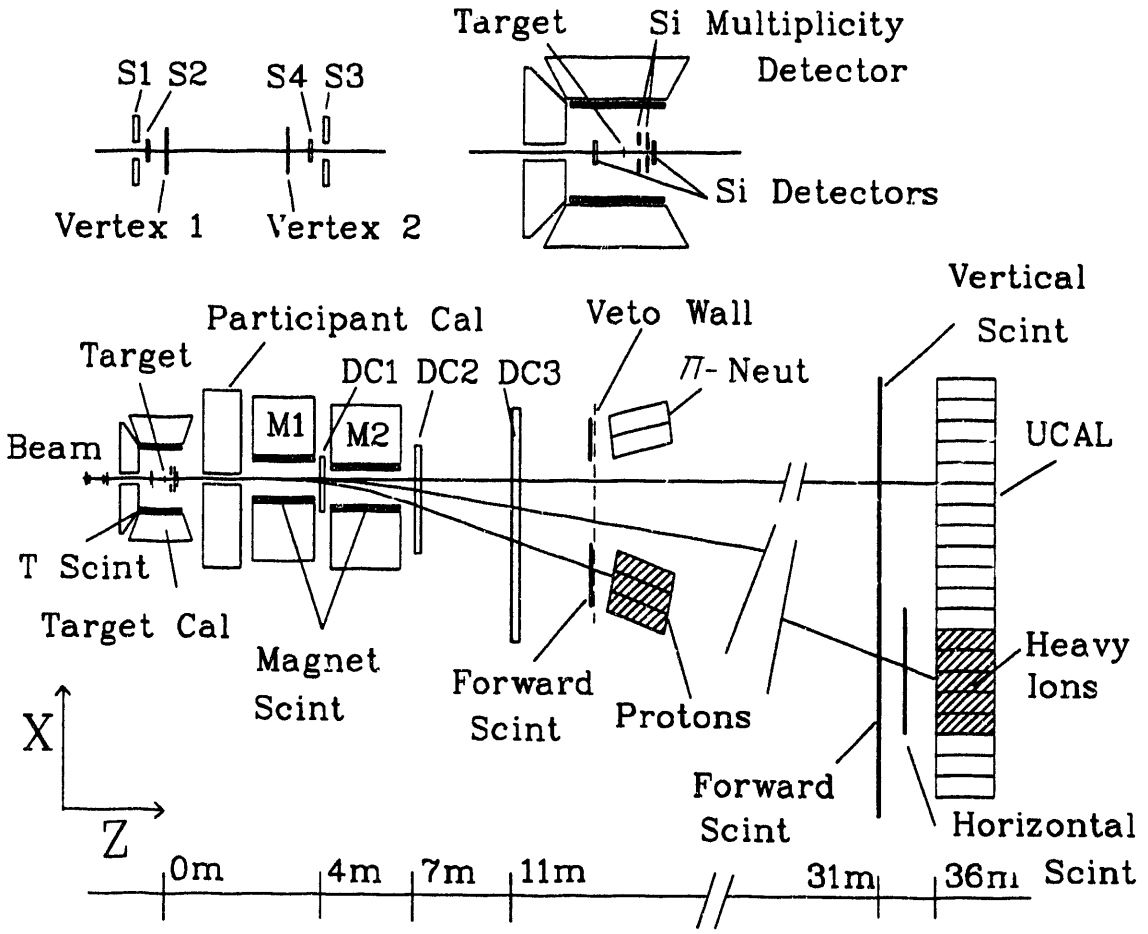

Figure 2.1: Diagram of the E814 apparatus. The beam enters through an aperture in the back of the target calorimeter. Forward going particles pass through the participant calorimeter opening and the two magnets M1 and M2. Track positions are measured in the tracking chambers DC1. DC2 and DC3. Charge is measured in the forward scintillators and energy is measured in the Target calorimeter. the Participant calorimeter and the U/Cu calorimeters. The top two figures show a blowup of the target region detectors.

2.1 Upstream Detector Group

- *Beam Telescope* (BSCI) – The beam telescope defines an acceptable beam particle for the experiment. It consists of two small scintillation counters (S2 and S4) and two veto counters with holes (S1 and S3). The timing signal T0 used as a start signal for the time of flight measurements was obtained from the S4 signals. The beam logic $S_2.S_4.\bar{S}_1.\bar{S}_3$ defines an approximately 3.0 mm beam spot on the target.

- *Beam Vertex Detector* (BVER) – The beam vertex detector consists of two silicon strip detectors of thickness 300 μm. placed in the incident beam line. They define the horizontal angle and position of the incident beam. The vertical strips have a pitch of 50 μm. and the two planes are separated by 3.0 m, giving an angular resolution of better than 20 μr.

- *Multiplicity Detector* (MULT) – The multiplicity detector consists of two concentric silicon discs, each 300 μm thick, and divided into 512 elements. The first disc is placed 3.4 cm downstream of the target and the second disc 8.2 cm downstream of the target. They cover an angular coverage of 2°-40°. These two detectors provide the charge multiplicity for any event.

- *Upstream and Downstream Si Detectors* – The upstream and downstream Si detectors consist of two surface barrier silicon detectors 1.0 cm in diameter and 100 μm thick. These are placed immediately upstream and downstream of the target to identify the charge of the incoming and outgoing particles.

- *Target Calorimeter* (TCAL) – The target calorimeter is composed of 992 NaI crystals, each of area 4x4 cm^2 and 6 radiation lengths thick, mounted in 5 separate boxes facing the target. Four of these boxes are placed with their faces parallel to the beam line (side walls) and the remaining box which contains a hole for the beam to pass, is positioned upstream of the target with its face normal to the beam line (back wall). This detector detects interaction products emitted at angles greater than 45° up to almost 180°.

- *Target Scintillators* (TPAD) – The target scintillators consist of 52 scintillators lining the inside face of the target calorimeter. This detector covers the same angular coverage as the target calorimeter side walls. This provides a measurement of charge multiplicity for any interaction. This measurement is complicated by the back scattered particles (albedos) from the TCAL.

- *Participant Calorimeter* (PCAL) – The participant calorimeter is a lead-scintillator calorimeter read out through wave-length shifting fibers into 512 photomultiplier tubes. It is divided into 16 azimuthal, 8 radial and 4 depth segments and has the same angular coverage as the multiplicity detector. This detector is

used to measure E_T in central collisions. However, it also serves as an excellent veto against nuclear interactions in peripheral collision studies.

2.2 Downstream Detector Group

- *Magnet Scintillators* (MSCI) – The magnet scintillators consist of 16 scintillators which line the lateral walls of the spectrometer magnets. The two side walls of each magnet are covered almost completely by them (8 in each magnet, 4 on each side of each magnet). Scintillators in the magnets D8 and D9 are 3.7x120x1 cm^3 and 3.7x230x1 cm^3 respectively. These are used in the peripheral program to veto events originating from nuclear interactions.

- *Veto Wall* – The veto wall consists of a set of scintillation counters, placed above and below the beam line in a vertical plane at z=12 m. These counters are mounted sufficiently far from the horizontal plane to be in the shadow of the forward collimation system and are used to veto background events caused by interactions downstream of the magnet.

- *Tracking Chambers* (DRCH) – The tracking chambers consist of an interpolating cathode pad drift chamber DC1 located between the two magnets, with one single plane of two dimensional cathode pad readout, and two drift chambers DC2 and DC3, located downstream of the magnet. These two chambers are of identical design except for size and number of wires. They consist of a drift section as well as a pad section. All three chambers are designed and constructed to detect tracks originating from minimum ionizing particles as well as beam-like fragments.

- *Forward Scintillators* (FSCI) – The forward scintillation counters measure the charge, time of flight and vertical coordinate of forward going particles. They are grouped together and form two hodoscopes which are located downstream of the magnet at z=12 m and z=31 m respectively. The upstream hodoscope consists of 10 vertical scintillator plates of dimensions 9.5x1x60 cm^3 (6 of these are placed in the region of Z/A=1, and the remaining 4 are placed in the region of Z/A<0) and the downstream hodoscope consists of 39 vertical scintillator plates of dimension 10x1x120 cm^3.

- *Horizontal Counters* (HSCI) – The horizontal counters consist of a scintillation counter array consisting of 5 horizontal counters of dimensions 10x1x120 cm^3 placed at z=34 m. They are placed directly in the path of the deflected beam particles. These counters provide additional information on the charge measurement of the heavy ion fragments.

- *U/Cu Calorimeters* (UCAL) – Stacks of 25 U/Cu calorimeter modules were installed downstream of the magnet at two locations, z=13 m and z=36 m, to

measure the energy and the position of reaction fragments at the downstream end of the spectrometer. Each module is approximately 20x100x120 cm^3 and they cover the same area as the forward scintillator hodescopes.

3 Trigger

3.1 Goals of the Trigger

The trigger system is a chain of electronics, which select the events to be recorded on magnetic tapes [37]. Due to the unknown nature of the characteristics of interesting events, the trigger was designed to permit as much flexibility as possible through software controlled logic systems. Every event is analyzed using a limited number of signals extracted from the detectors to allow the data acquisition system to select good events for recording on magnetic tapes for further analysis. It has the capability to enhance the rare event types by downscaling (i.e accepting only a fraction) the higher cross section events, as well as to record a variety of event types.

The main goals of the E814 trigger system for the three principal physics programs are:

- Identify central collisions through the requirement of high E_T using weighted analog sums of the signals from detectors in the target region, especially the participant calorimeter and the target calorimeter.
- Identify peripheral collisions through a requirement of low E_T in the target region, and appropriate energy and charge in the U/Cu calorimeters and forward scintillators.
- Identify candidates for strangelets through a measurement of time of flight in the forward scintillators by selecting low velocity particles in the final state.

To achieve these goals, summed signals from most of the detectors were made available at the trigger electronics, for decision making. This included signals from target region detectors as well as downstream detectors. Drift chambers were not included in the trigger, since track recognition was not required at the trigger level.

3.2 Trigger setup

First, signals from different detectors were grouped [1] together and brought to the counting house where the trigger electronics are set up Necessary time delays were added to the signals, depending on the location of the detectors as well as the stage at which the signals were processed in the trigger. All these signals were calibrated and gain equalized prior to the run. However, the gains of the photomultiplier tubes

[1] The formed groups of signals for important detectors are described in section B

show long term as well as short term variations. Hence, the detectors were calibrated throughout the run as often as was necessary for the proper operation of the trigger.

The trigger makes its decisions at three separate levels as shown in Figure 2.2. At the preliminary stage of the trigger (beam trigger), a decision is made as to whether a good beam particle has passed through the Beam Scintillator system. Then, the coincidence of the beam trigger and a prompt signal from one of the major detectors (multiplicity detector, U/Cu calorimeters, target calorimeter or participant calorimeter) was used to form the pre-trigger. The pre-trigger issues the START signals to all the ADC's and TDC's to start their digitization and activate the higher level triggers which process in parallel with the digitization. At the next level, the trigger (1st level) checks for the presence of another beam particle close to the one generated at the pre-trigger and rejects the event if such a particle exists (after protection). If not, the last stage (2nd level) will be activated and the decision is made as to which physics events are to be recorded, and the control is passed over to the data acquisition system.

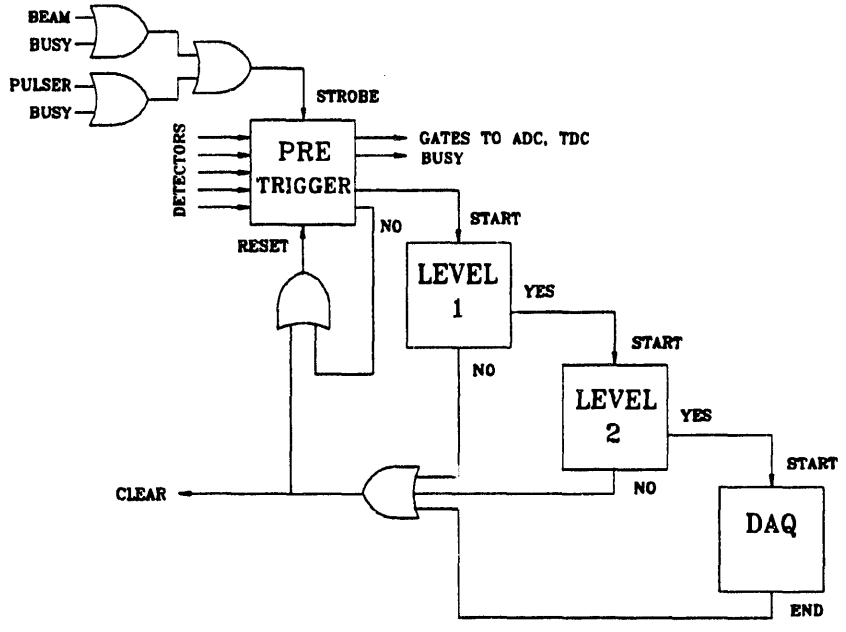

Figure 2.2: A block diagram of the E814 trigger system.

4 Data Acquisition System

4.1 Front End

The data acquisition system consists of 6 fastbus crates, each controlled by a SLAC Scanner-Processor (SSP) as shown in Figure 2.3. Five of these read out their own crates, and pass the data to the Master SSP, which reads out its own crate and assembles all the data into an event. The Master fastbus crate has a 4 MB fastbus

memory module, a CFI card which connects to a Microvax and a Struck FBD to read the CAMAC branch which contains trigger electronics and a portion of data from several detectors.

After receiving a START signal from the trigger the Master SSP takes the following actions.

- A logic output signal (SSP BUSY) is generated which suppresses any triggers, until it is cleared.
- The lower level SSPs are signaled to begin reading out the modules in their crates. Each crate works in parallel.
- Devices in the master crate are then read out.

When the Master SSP is finished with its own crate, it begins polling the lower level crates for their data, and builds the data record for one event. This event record is then written into the memory card and SSP BUSY is cleared.

During a spill, the event records are stored in the Fastbus memory, and when the spill is over, the microvax is given the signal to read before the next spill occurs. If the microvax does not finish reading in time, the next spill or spills are skipped until it is done. On average 30 events per spill will be recorded and the SSP readout time is approximately 10 msec per event.

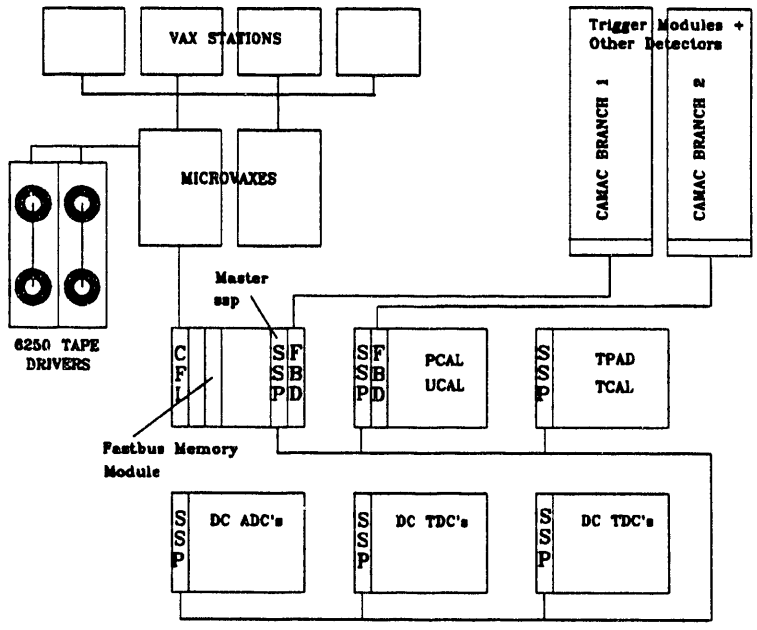

Figure 2.3: A block diagram of the E814 data acquisition system.

4.2 Microvax

The heart of the data acquisition system is a Microvax which is linked to the Master SSP via the CFI controller. This machine is connected to two. high speed. 9 track tape drives. on which data is written. It is also connected via DECnet (Ethernet lines) to another Microvax and 4 Vaxstations.

Data collection is done by three processes:

- The Link server. which waits for a signal from the Master SSP, reads out the fastbus memory card. and stores events into a buffer.
- The Buffer logger, which writes events to a tape, if the user desires.
- The Buffer processor, which takes events and puts them into the event pool, which is a large. shared memory area that user-written programs may pull events from. Typically, this receives about 10% of the events.

In addition. there are processes (Daq servers) which get events from the pool. and transmit them. via DECnet. to Vaxstations which perform online monitoring of data. On each workstation. another process (the Daq client) collects events from the Daq server. and puts them into an event pool local to the workstation. Typically. the experimenter runs programs (consumers). which extract events from this pool and analyze them.

B Detectors used in EMD studies

Although we used all the detectors in the experiment for EMD studies, in this section an extended description of three of the most vital detectors is given. These detectors are used to measure the charge. energy and momentum of the fragments in the downstream end of the spectrometer.

1 Forward Scintillators

1.1 Construction

The principal objectives of Forward Scintillation counters are to measure the charge (Z). the time of flight (T) and the vertical position of the reaction fragments at the downstream end of the spectrometer. They must have the capability to measure Z=1 as well as Z=14 particles requiring a dynamic range of 1:200. In addition, the online Z measurement should be good enough to be used in the second level trigger.

The resolution in the measurement of Z in a scintillator depends primarily on the statistical fluctuations in the deposited energy arising from the production of energetic δ rays. and the non-uniformity in thickness over the exposed area of the scintillator material. The general theory for the loss of energy of charged particles in matter is known to be a Landau distribution [38]. The limited energy deposited

by the ionization of heavy particles in thin absorbers due to finite thickness was first discussed by Vavilov [39] and was later improved by Badhwar et al [40, 41] correcting for the energy loss due to escaping electrons. This effect makes the distribution more Gaussian in shape because the statistical fluctuations have less effect on the mean energy deposition. If we approximate the distribution of the deposited energy analyzed by Badhwar for heavily ionizing particles by a Gaussian distribution, it can be shown that,

$$\left(\frac{\sigma}{I}\right)^2 = \frac{\gamma S}{(2SZ^k)^2}$$

where S is the scintillator thickness, k is a property of the scintillator and I is the mean light yield. γ is given by

$$\gamma = \xi\epsilon_D\left[2 - \frac{\epsilon_D}{\epsilon_{MAX}}\left(\frac{\beta^2}{2} + 1 + \beta^2\ln(\frac{\epsilon_{MAX}}{\epsilon_D})\right)\right]$$

where $\xi = 0.3(z/A)(mc^2/\beta^2)SZ^2$.

In these expressions ϵ_D is the mean energy deposited by a δ ray that leaves the scintillator and ϵ_{MAX} is the maximum δ ray energy. The quantities z and A are the atomic number and the atomic weight of the absorber respectively, m is the electron mass, and βc is the particle velocity. For a 1 cm thick scintillator, we find that $(\sigma/I) = 0.18/Z^{(k-1)}$ which yields a resolution of 2.8% at Z=14, assuming k=1.7.

In addition to the effects discussed above, the measured Z resolution of a light output of a scintillator suffers due to the scintillator saturation as well as the gain drifts in photomultiplier tubes. These questions are addressed in more detail in chapter 3.

The NE104 scintillators with 120 cm attenuation length were selected to construct the downstream forward scintillators because of their faster decay time properties. The upstream scintillators were constructed with Bicron 420 scintillators. Each scintillator slat was connected to two photomultiplier tubes as shown in Figure 2.4. Light generated in the scintillator material was guided into the phototubes through light guides connected between the cathode of the phototube and the scintillator material itself. We used EMI-9954 photomultiplier tubes with 12 stage bases in most of the forward scintillators.

From the downstream scintillators, two signals were taken from each phototube, one from the anode and the other from the last dynode. The last dynode signals were added together and inverted and this signal was brought into the FERA ADC's (LeCroy 4300B, Fast Encoding Readout ADC) of 10-bit accuracy, and was used in the trigger. The anode signals were split passively between a fastbus ADC (LeCroy 1885F dual range ADC) and a dual discriminator (Phillips Model 7106). One output of the discriminator was fed to a TDC (LeCroy Model 4291B) of 300 ps/channel resolution and the other was connected to a FERET (LeCroy 4303, Fast Encoding

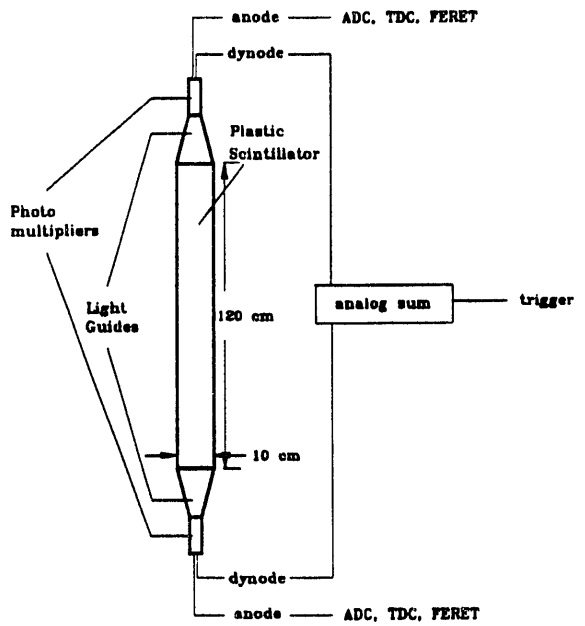

Figure 2.4: A forward scintillator slat.

Readout TDC) with 50 ps/channel resolution which was used in the trigger. The dual range ADC's lower range has a 50 fC/channel sensitivity whereas the upper range has 400 fC/channel, giving a full digitizing range of $\approx$ 1600 pC/channel. These ADC's are extremely useful in maintaining the required sensitivity along the full dynamic range.

The anode signals of the upstream scintillators follow the same path as those of the downstream scintillators, but the dynode signals are discriminated immediately after extraction from the phototube to prevent the degrading of the timing resolution due to the change in the pulse shape when the signals pass through long delay cables. The output signals of the discriminators were brought into the counting house and discriminated again and connected to a 50 ps/channel TDC (LeCroy Model 2280A) system for a timing measurement of higher precision.

1.2 Calibration

The gain equalization of each phototube was done by using a ^{106}Ru, 1 mC radio-active source. First, the Ru source was mounted on a holder and placed at right angles to the scintillator slat, roughly, in the middle. Another small scintillator counter with one phototube attached, was placed behind the counter to be calibrated. This counter serves as a trigger for the signals from the Ru source to reduce the background due to cosmic rays (as well as x-rays and γ rays emitted by the Ru source). Signals from dynodes were connected to an ADC with the gates generated by the trigger counter and read by a small data acquisition system controlled by a PC. One phototube at a time was calibrated to bring minimum ionizing particles roughly at 300 ADC counts

(in a dual range ADC this is equivalent to 15 pC) for downstream scintillators (except for the beam region) and 1000 ADC counts for upstream scintillators (since upstream only get minimum ionizing particles).

Due to the large amount of light generated in the scintillators in the deflected beam region by heavy fragments, each beam region, used by three different physics programs (roughly 7 counters) were calibrated at a lower voltage setting, so that there would be no overflow in the FERA ADCs. As a result, we were unable to use the full range of dual range ADCs which can digitize upto ~32K ADC counts (or 1600 pC). A typical Z=14 particle produced 10-15K ADC counts with the selected gain settings in these ADCs.

The gain calibration of the phototubes was done once prior to the data taking run and the calibrated voltages were loaded into the HV power supply for the phototubes before each physics program operated.

2 U/Cu Calorimeters

2.1 Construction

The main purpose of the U/Cu calorimeters are to provide information about the energy (E) of the beam rapidity nucleons going through the 0.8° hole in the participant calorimeter. They should measure positions (X and Y) of the particles with reasonable accuracy and should be able to resolve multineutron or multiproton events where several neutrons or protons hit the calorimeter wall simultaneously. A good online energy resolution is essential to trigger on various peripheral channels.

To achieve these goals, U/Cu/Scint calorimeters built for ISR experiment R807 and subsequently used by HELIOS collaboration (CERN experiment NA34) were redesigned [42, 44] by replacing the electromagnetic section with one continuous hadronic section. In addition, the scintillator plates were optically decoupled to improve the ability to separate two showers in the same neighborhood. Although such a change would reduce the measured energy resolution of $0.35/\sqrt{E}$ in these calorimeters, the collaboration decided to sacrifice energy resolution for required spatial measurement capability.

Figure 2.5 shows a schematic drawing of the redesigned calorimeters. Longitudinally, each module consists of 40 identical sections, each with a 5 mm Cu plate and two 30 mm depleted uranium plates as an absorber, alternating with 2.5 mm scintillator sheets. The total depth of a stack is 4.2 absorber lengths. Light created in the scintillator is intercepted by wavelength shifter (WLS) bars parallel to the beam direction, 2.5 mm thick, 10 cm wide and 120 cm long. Each module has 24 WLS bars, 12 on each side of the stack and they are coupled to phototubes located in the back of the module. The phototubes used were EMI 9905B and phillips XP2081 except for the three calorimeters in the deflected beam region. In these regions we used Hamamatsu photo tubes.

Depending on the light decoupled sections of the scintillator plates we can separate

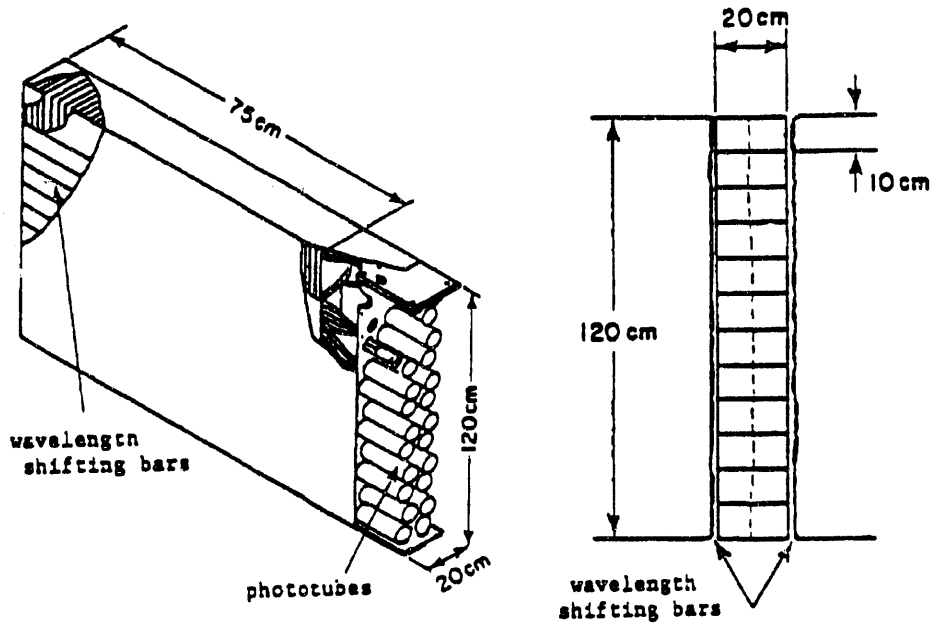

Figure 2.5: A U/Cu calorimeter module. Ref [44]

the 25 modules into three types. The first type consists of 3 modules which are used to detect protons. Each of these are divided into 24 sections of 10x10 cm^2 cells. The second type with no divisions consists of one module (beam calorimeter) placed directly in the Z/A=0.5 beam line. The rest of the modules consisting of 20x10 cm^2 size cells are used to detect neutrons, proton rich or neutron rich nuclei as well and π-neuts.

From each calorimeter module, anode signals of the photomultiplier tubes (each module has 24 photo tubes) were extracted and split into two. One of these signals was connected to a summing box which performs the analog sum of 24 signals over each calorimeter module. The other signal was connected to a Fastbus ADC (LeCroy model 1882) of 400 fC/channel. The output signals from the summing boxes were split into two and one signal was connected to the FERA ADC's (LeCroy model 4290) which were used in the trigger and the other signal was discriminated and connected to a TDC (LeCroy Model 4291B) system to extract timing from calorimeter modules.

2.2 Calibration

The gain equalization of each phototube in individual stacks was done using the radioactivity of the uranium plates in the calorimeter itself. Uranium plates create uniform low level light (uranium noise) in the scintillator plates. The gains of the phototubes can be adjusted so that the response of each tube to the uranium noise produces the same average DC current.

For the measurement of the average uranium current, a CAMAC module (current monitor) was designed and built. The current monitor contains a current-voltage

conversion (CVC) followed by a voltage-frequency (VFC) conversion. The output of the VFC is connected to a scaler in each channel. Due to the possible signal ground problems which alter the measurement of the gain in each photo tube, one single phototube in each individual stack was completely covered (blackened phototube) to use as a reference and the calibration procedure was carried out as described below.

- Without turning the high voltages on the phototubes, the background noise signal was recorded for each tube.
- Phototube voltages were turned on and the new signals from each phototube were recorded. The shift in the signals from the blackened phototube was computed and each phototube signal was corrected by this amount in each module. This shift indicates the possible ground shifts due to the addition of voltage supplies assuming all phototubes produce roughly the same amount of dark currents.
- For three different voltage settings, current monitor readings were recorded and the gains in each tube due to the uranium light was calculated. With an extrapolation, a new voltage setting was calculated for each tube to bring the gain to the reference value.

This was done on an average, every 24 hours during the normal data taking runs. The reference reading was calculated by the response of these calorimeters to 12 GeV pion and muon beams.

Although there are a few corrections involved in the procedure, it was found that the method brings the phototube gains to the standard energy scale. The studies of gain drifts in phototubes is discussed in more detail in chapter 3.

3 Tracking Chambers

E814 operating conditions provided an important challenge for tracking detectors. They were required to operate in an environment with high track densities and high beam rates which can extend upto 1 MHz. In addition, they require a large dynamic range which begins with minimum ionizing particles and extends upto heavy fragments with Z=14. A detailed description of E814 tracking chambers is given elsewhere [45, 46] and only the relevant information to understand the performance of the drift chamber studies described in this thesis is given here.

3.1 Pad Chamber (DC1)

This detector, placed in between the two dipole magnets plays an essential role in this analysis. As shown in Figure 2.6 (a), it consists of a single cathode plane divided into a large number of rectangular pads. Anode wires are placed above the pads and field wires with slightly negative potential are placed in between the anode wires. All

pads beneath one anode wire are interconnected by a resistive strip. An avalanche created by a charge particle traversing the detector induces a localized charge on several pads. Measurement of the induced charge on the pads, combined with an interpolation, provides an unambiguous measurement of the track position.

Depending on the track densities, the readout spacings vary over the plane of the chamber. Approximately, every 10th pad is readout by charge sensitive preamplifiers which are mounted on the chamber itself. Each preamplifier output passes through a pair of transformers into a shaping amplifier which produces a bipolar pulse of 200 nsec risetime and this is digitized by a 15-bit LeCroy model 1885F dual range ADC system.

The active area of the chamber is 26x16 cm^2. The anode wire spacing is 4 mm and the separation between readout nodes range from 15 mm (edges) to 6 mm (center) giving a total of 1016 channels. Detector thickness is about 6% radiation length. With collimated x-ray beams, a position resolution of $\approx$ 70 μm was observed.

3.2 Drift Chambers (DC2 and DC3)

The drift chambers DC2 and DC3 consist of 6 drift planes followed by a single layer of chevron shaped pad plane as shown in Figure 2.6 (b). The corresponding wires in adjacent drift planes are shifted by half of the separation between wires in a single plane to eliminate the effects of left-right ambiguity in track reconstruction. An aluminized milar layer is inserted in each drift section to absorb the low energy δ rays.

Signals from each anode wire are connected to low noise preamplifiers. The output of the preamplifier is connected to a unipolar shaping amplifier which has a gain of $2x10^3$ and a risetime of 12 nsec. The output of the shaping amplifier enters a dual discriminator in which the lower level sensitive to the leading edge of the signal generated by the drift cloud and the upper level which is blind to minimum ionizing tracks, measure the centroid of the charge distribution of heavily ionizing tracks (zero-crossing discriminator). The upper level shapes the 12 nsec unipolar pulse into a 60 nsec risetime bipolar pulse before the signal enters the zero-crossing discriminator with a gain of $\sim$ 1 at the shaping stage. The output of the dual discriminator is connected to a 10-bit, pipeline, LeCroy 1879 TDC with 1 nsec resolution. Signals from the cathode plane follow the same path as DC1 signals.

The active size of these chambers are 10x50 cm^2 and 20x100 cm^2 respectively, and they are identical in design. DC2 has 128 wires in each driftplane with a separation of 6.35 mm. Its pad plane has a total of 464 chevron pads with variable density ranging from 3 mm to 9 mm. DC3 has 160 wires in each driftplane with a 12.70 mm separation and a total of 760 pads whose sizes range from 5 mm to 15 mm. The thickness of DC2 and DC3 is about 10% and 20% radiation lengths respectively. Both chambers were expected to provide a 200 μm single cell resolution in the X direction and the chevron pads were expected to provide a resolution of approximately 1-3% of the spacing between readout nodes in the Y direction.

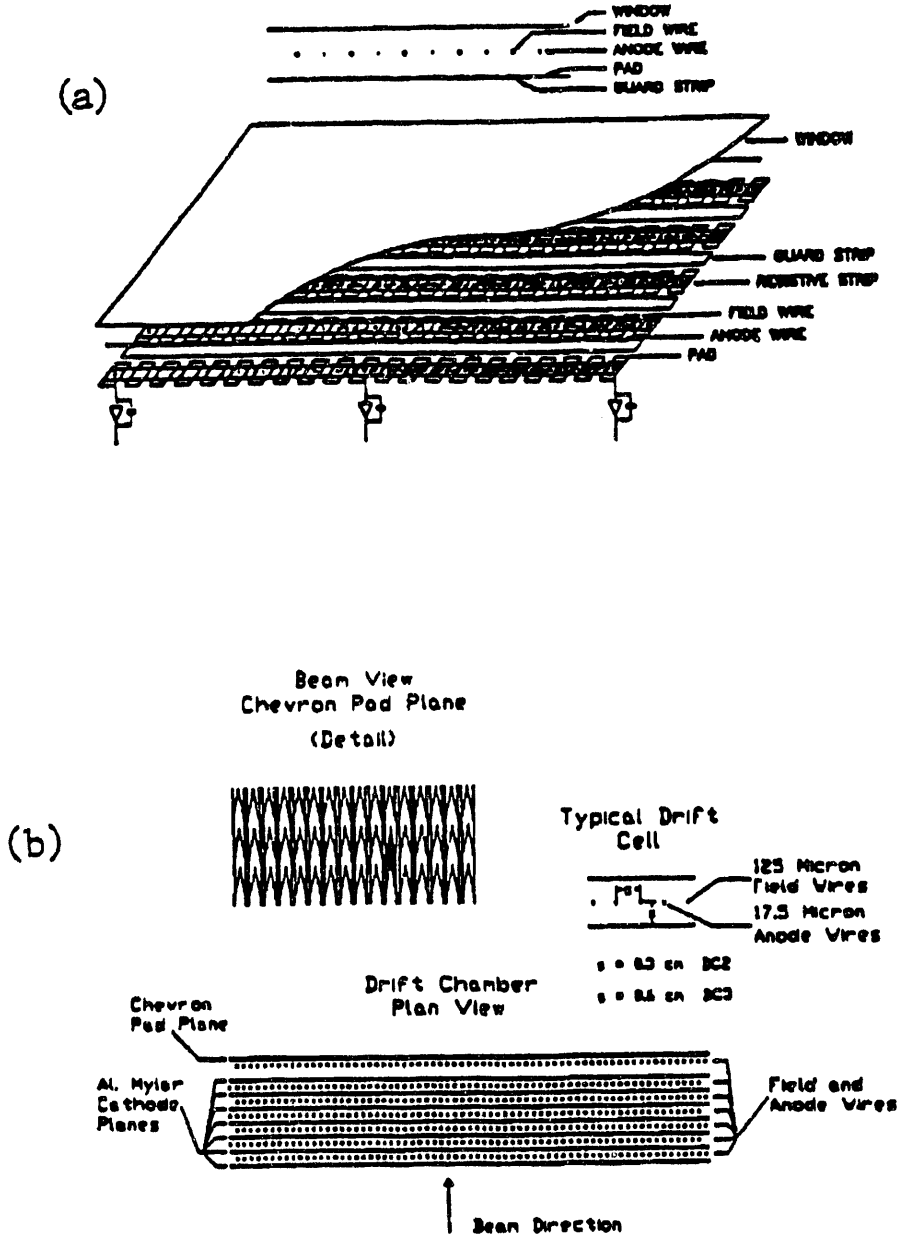

Figure 2.6: The E814 tracking chambers. (a) A view of the pad chamber DC1 showing the locations of the anode wires and field wires. (b) A view of the drift chamber DC2 (and DC3) showing the chevron pad plane and the drift region. Ref [46]

3.3 Calibration

The drift cells operate by measuring the time between the passage of an ionizing particle and the subsequent avalanche around the anode wire. Thus, at the calibration phase, the relative (channel-to-channel) time delays of each channel are measured and recorded. In the offline analysis, adjustments are made to the calibration constants to correct for variations in time at the reduced gain region.

The pad chambers operate by measuring the image charge on a segmented cathode plane facing a standard drift wire. The centroid of the image charge distribution is inferred by measuring the relative charge accumulated on neighboring pads. Thus, the important parameters in the pad chamber calibration are the gain and pedestal of each channel. Since the charge signals are measured by 1885F dual-range ADC's, each channel must be calibrated independently for the two ranges.

A free-running pulser was used as a trigger for the data acquisition system and for a calibration pulser. The trigger pulses were delayed considerably before entering the data acquisition system. An adjustable delay between the trigger pulser and the calibration pulser was used to time the chamber's signals with the gates generated by the DAQ. The pulse height of the calibration pulser is controlled via a DAC resident in CAMAC. A system of CAMAC-controlled switches are used to ship the calibrated timed pulses to small regions of each chamber. The system is controlled by the same micro-VAX as is used for the data acquisition, but is run independently of the normal data acquisition since the normal DAQ does not provide the facility to program the calibration pulser during data taking.

During drift cell time calibration, the settings of the discriminator thresholds for each channel are also recorded with the measured time for the timed pulses. This was accomplished by recording the response to different pulser amplitudes. Tests have shown that the time value at threshold and the time value well above the threshold create the same relative time calibration for all channels due to the coarse (2 nsec/channel) digitization of the time.

The pad chamber calibrations are achieved by recording the response of channels to different pulse amplitudes. The low range and the high range of the ADC's are calibrated separately. The pedestal values are obtained from a set of "empty events" taken without pulsing the chambers. This method is required by the fact that there is a slight DC offset between the DAC (located in the counting house) and the calibration pulser (located near the chambers).

The calibration procedure is fully automated (with the exception of occasional gate timing and panel switch attenuator) and requires approximately 1 hour. This is executed before the data taking run.

CHAPTER 3

Detector Studies

In experimental physics, the quality of the results depends on the resolution of the detectors used. Due to various factors, the resolution of the detectors, achieved through bench tests is degraded in the experimental environment. For this reason, understanding the performance of the detectors, and, the corrections for factors contributing to degrade the resolution, plays a very important role. Studies to achieve the optimum resolution for Forward Scintillators, U/Cu Calorimeters and Tracking Chambers are described in detail in this chapter.

A Forward Scintillators

The Forward Scintillation counters are expected to provide a resolution which separates all charges from Z=1 to Z=14. This requires the offline analysis to obtain an optimum resolution from these counters. The counters located at the deflected beam region suffer more than the counters in other regions from rate dependence problems. Therefore corrections which are applied to obtain the best possible resolution for these counters are described.

1 Noise Corrections

1.1 60Hz corrections

The gain setting in the PM tubes in the deflected beam region counters provides a signal of about 5 pC for minimum ionizing particles. In order to obtain a good resolution for these particles, a pedestal (integrated noise when there is no signal) width of less than 1 pC is required. However, during the test runs, signals from these counters showed a pick up noise from power cables corresponding to a 60Hz ripple which is approximately 2-3 pC. This ripple scaled with the gain setting in each region can seriously compromise the signal resolution.

Because of our sensitivity to the 60Hz ripple, we used a special CAMAC unit to measure the position of the 60Hz waveform for every event. The measured position together with the event records were written in the data tapes. The CAMAC unit is a four channel, 24-bit scaler, whose contents are stored in a register upon receiving a signal (in this the case the pre-trigger), with 4 μsec accuracy. The scaler contents

are cleared with a signal, derived from a zerocrossing discriminator which views the 60Hz waveform.

Figure 3.1 (a) shows a scatter plot of the signal (pulse height) obtained from one end of the forward scintillators in the beam region, against the measured position of the 60Hz ripple, when no beam particle is present in the apparatus (MT event). In this scale, minimum ionizing particles produce a signal of around 100 counts.

The shift in the pulse height for any location of the 60Hz ripple, for each signal, was evaluated by fitting orthogonal (Tschebyschev) polynomials for waveforms similar to the one shown, generated from each signal and corrected on an event by event basis. This removed the major noise contribution in the forward scintillator signals. However, even after correcting for the 60Hz ripple, a small component of the noise was present in each signal. This noise was correlated to the noise in signals of the neighboring counters which share common grounds in the electronics in the counting house. An additional correction was applied by computing the average noise in a physical group of signal cables. Only the signals which did not show a "hit" was used to calculate the noise average. A pedestal width of σ ~2 ADC counts (0.1 pC) was achieved after the correction.

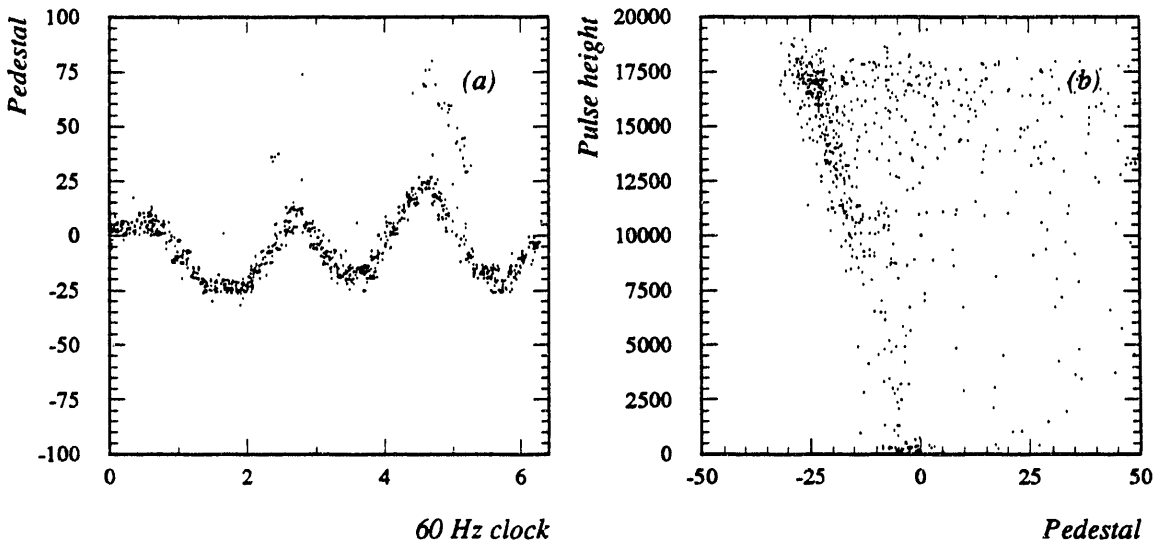

Figure 3.1: Noise in forward scintillators. (a) Effect due to the 60Hz ripple. (b) Cross-talk between nearest neighbors.

1.2 Cross-talk corrections

When real beam particles traversed the scintillators, an additional broadening was observed in the beam region counters. This effect caused a negative shift in the pedestals which was most prominent in the counter adjoining the counter in which the beam passed. A close inspection showed that this effect arises due to the cross-

talk in the current monitors. [1] Whenever a beam particle or a high Z particle passes through a scintillator, the signal going through the current monitor induces an inverse polarity signal in its neighbors, causing this effect.

Figure 3.1 (b) shows the signal at one end of the scintillation counter through which the beam passes (DB counter) against its closest neighbor. A typical beam particle produces a negative shift of about 20-40 ADC counts in the closest neighbor. This effect was corrected by searching the counter which has the largest signal, and estimating the negative shift with a linear extrapolation to the signal height. The induced noise decreased with the distance from the beam counter and was present in about 8 counters surrounding the DB counter (4 to each side). After correction, a pedestal width of $\sigma \approx$ 3-5 ADC counts (0.15-0.25 pC) was achieved for beam region counters.

2 Charge Measurement

When a fast moving charge particle passes through a scintillation counter, it deposits an energy that is proportional to the square of its charge in the scintillation material. This energy is transformed into a pulse of light which travels along the scintillation counter. This can be detected and amplified by photomultiplier tubes placed at each end of the counter. We need to investigate how we can relate these signals and thereby extract the charge of the particle.

Consider a simple model of a scintillation counter with photo tubes attached at each end. Let x be the distance along the scintillator from the center to the point through which the charge particle traversed. The pulse height measured at the two ends can be written as,

$$Q_1 = LG_1 \exp\left[-\frac{(s+x)}{D}\right]$$

$$Q_2 = LG_2 \exp\left[-\frac{(s-x)}{D}\right]$$

assuming a pure exponential light attenuation in the light guide and the scintillator. Here, L is the light produced in the scintillator by the charged particle, G_1 and G_2 are the gains of the phototubes, s is the half length of the scintillator and D is the attenuation length of the scintillator. By taking the geometrical mean of pulse heights we get,

$$\sqrt{Q_1 Q_2} = L\sqrt{G_1 G_2} \exp\left[-\frac{s}{D}\right]$$

which is independent of the hit location of the particle and depends purely on the gains, and the amount of light (which is proportional to Z^2) that is produced in the scintillator.

[1] see chapter 2, section 2.2

Figure 3.2 shows the measured charge distributions for low Z particles in the forward scintillators obtained by evaluating the geometrical mean. In this scale, the gains were normalized to place minimum ionizing particles at 100 counts. The distribution shows a characteristic Landau shape.

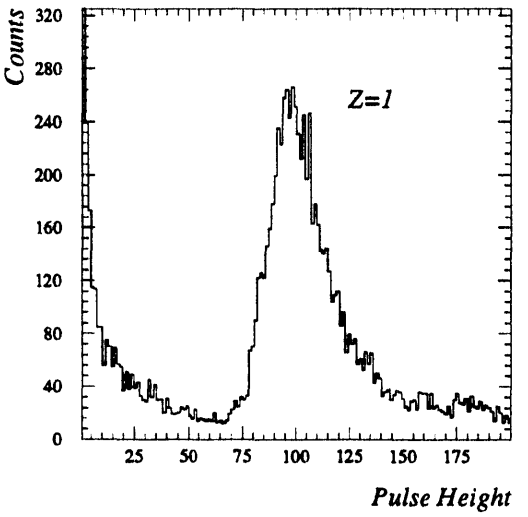

Figure 3.2: Measured pulse height in upstream forward scintillators for minimum ionizing particles.

3 Saturation Effects

For high Z fragments, the scintillators show a deviation from the expected Z^2 behavior. Although the specific mechanisms are not known, this effect has been discussed by many authors [47, 48]. The simplest model divides the ionization energy loss into two regions, the "core" and the "halo". The core is a region of high ionization density around the charge particle path, causing "saturation" or decrease in scintillation efficiency due to an enhancement in non radiative decay channels. The halo is a much larger region of low energy density surrounding the core that is energized by δ rays that are created in close collisions with the charge particle and suffers no saturation.

We used the simple parametrization suggested by Birks [49] for heavily ionizing particles at low velocities given by,

$$\frac{dL}{dX} = \frac{A(dE/dX)}{1 + B(dE/dX)}$$

where (dL/dX) is proportional to the amount of light produced for a particle of given ionization dE/dX, and A and B are two parameters which depend on the scintillator material. For 16 counters in the beam region (11 vertical and 5 horizontal) the

parameters A and B were evaluated and corrected for this effect, by inverting the above formula. Table 3.1 shows the extracted parameters A and B, for 3 counters in the horizontal scintillator hodoscope and 5 counters in the vertical scintillator hodoscope in the deflected beam region. Although the constants A and B should be the same for a given scintillator material, a variation was observed among NE104 scintillators. This could be induced by the gain variations in the photomultipliers.

Table 3.1: The extracted parameters A and B using Birk's parametrization for a set of scintillator materials

Counter	Scintillator	A	B x1E-3
8	NE104	19.69	0.79
9	Bicron 400	19.77	1.60
10	NE104	19.67	0.59
24	NE104	19.69	0.76
25	NE104	19.66	0.49
26	NE104	19.67	0.56
27	NE104	19.67	0.64
28	NE104	19.67	0.64

Figure 3.3 (a) shows a measured charge distribution from the downstream silicon detector, against a measured charge from one of the forward scintillators in the beam region. The events that lie along the 45 degree line correspond to good candidates and the horizontal band of events corresponds to the downstream interaction products. Since the Si detector response is proportional to Z^2, the deviation from the 45 degree line indicates the scintillator saturation. Figure 3.3 (b) shows the same counter after correcting for the saturation effect. Resolution of ~4.0% was observed for Z=14 particles in individual counters. The non uniformity in thickness along the counter length, and the phototube gain variations during the spill have not been taken into account in this analysis.

4 Time of flight

4.1 Slewing Corrections

If we consider the same model described in section 2, and assume a constant velocity v of light in the scintillator, the measured timing at the two ends can be written as

$$T_1 = \bar{T} + \frac{(s+x)}{v}$$

$$T_2 = \bar{T} + \frac{(s-x)}{v}$$

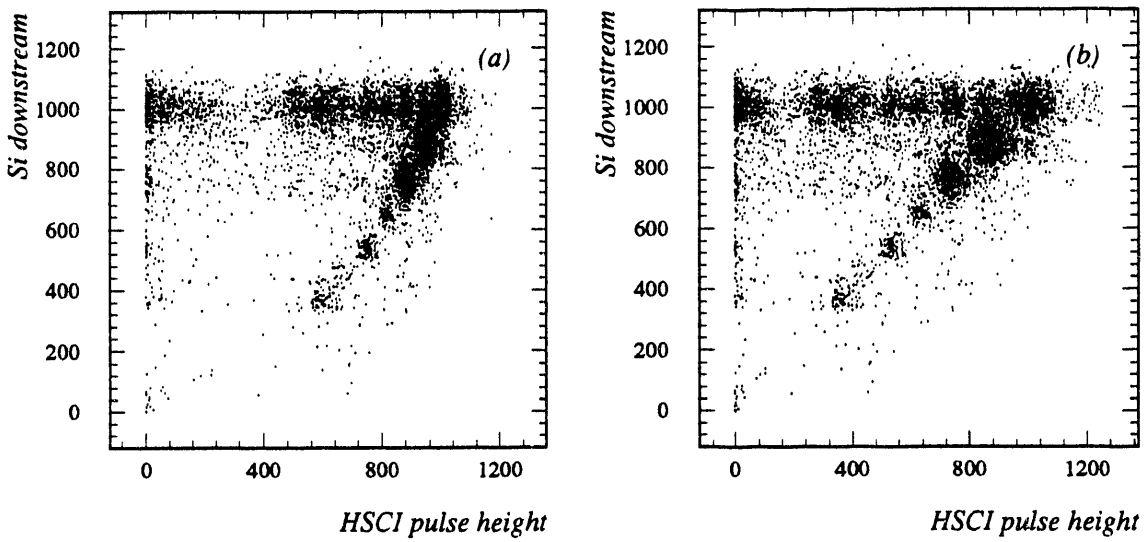

Figure 3.3: Effect of scintillator saturation. (a) Pulse height in Si downstream vs. measured pulse height in a scintillator. (b) Same after correcting for the scintillator saturation.

where $\bar{T}$ is the time of arrival of the particle at the counter. For simplicity, constant time offsets, such as phototube transit times, cable lengths and delays in the electronics are omitted from this discussion. By taking the average we get,

$$\frac{T_1 + T_2}{2} = \bar{T} + \frac{s}{v}$$

which is independent of the hit position and, since s/v is a constant, provides a measurement of the time of arrival of the particle.

This simple formula does not take into account the dependence of measured time on pulse height when leading-edge discriminators are used (slewing). Figure 3.4 (a) shows the measured pulse height against the measured time for one end of a counter. Leading-edge discriminators fire whenever the leading edge of the signal rises above a given threshold. When the signal becomes larger, the time to cross a given threshold becomes smaller, producing this effect. The corrections for the slewing effects have been discussed by many authors [50, 51], and following their arguments the corrected time was defined as,

$$T_c = T_1 + (A + \frac{B}{\sqrt{Q_1}})$$

where A and B are constants. The constant A (which accounts for the time offsets omitted in the previous discussion) is added to shift the time distribution to be centered at zero in order to simplify the cuts used in this analysis. Figure 3.4 (b) shows $1/\sqrt{Q_1}$ against the measured time for the same end of the counter. A linear

relationship was observed justifying the above equation. For each phototube, the parameters A and B were computed and corrected for the slewing.

The time of flight distributions, computed by taking the average of T_1 and T_2 after correcting for the slewing effects for the counters in the beam region and the counters in the upstream proton region, yield a resolution of 350 ps and 215 ps respectively.

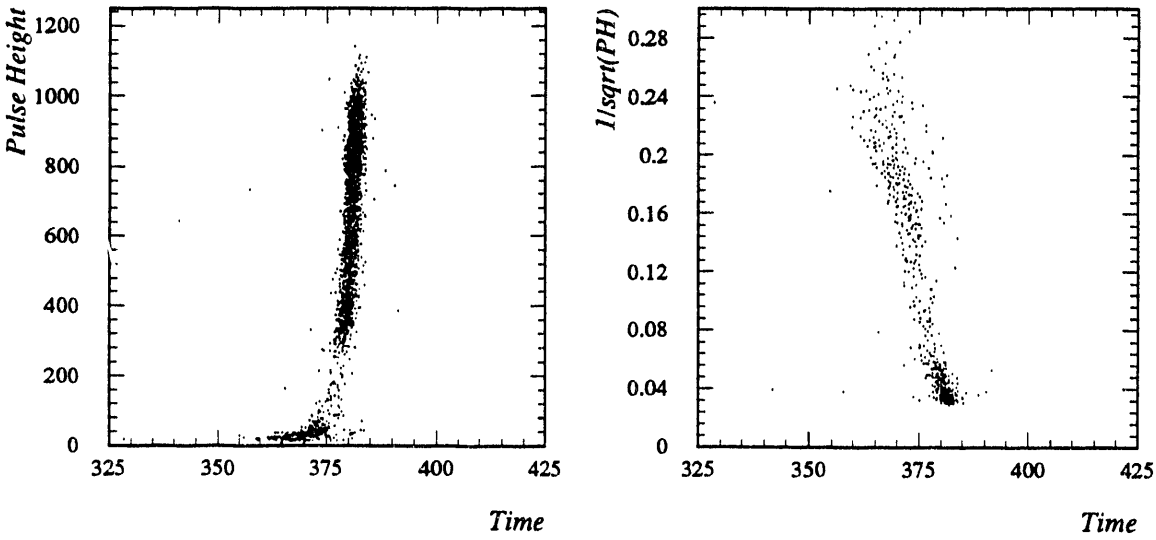

Figure 3.4: Effect due to slewing for time measurement. (a) Pulse height vs. time. (b) 1/sqrt(PH) vs. time demonstrating a linear relationship.

4.2 T-zero corrections

An additional contribution to the width of the timing signal comes from the time jitter associated with the start timing (T-zero) of the experiment obtained through one of the S4 signals. This effect can be corrected by taking the average of S4 timing signals. This correction was applied only to the upstream scintillator hodoscope where the highest resolution was required to identify prompt signals from albedo signals (background noise from particles scattering backwards) coming from the upstream calorimeter modules which are located roughly about 1.0 m from the upstream forward scintillators. A resolution of $\approx$ 200 ps was observed for upstream counters after all corrections were made.

5 Position Measurement

5.1 Position by pulse height

If we take the ratio of the expressions given in section 2 for the pulse height measured at the two ends of a counter, we get,

$$x = \frac{D}{2}\left[\ln(Q_2/Q_1) + \ln(G_1/G_2)\right]$$

which is a direct measure of the position along the scintillator. For every counter, $\ln(G_1/G_2)$ was estimated by centering the position distributions at x=0. The attenuation lengths D for NE104 and Bicron 400 scintillators are 120 cm and 200 cm respectively. By this method, a position resolution of 2 cm was obtained.

5.2 Position by timing

If we consider the expressions given in section 4 for timing measurements, we can write,

$$x = \frac{v}{2}(T_1 - T_2)$$

which gives an independent measurement of a position along the scintillator. The light velocity v inside the scintillator was found to be 18.75 cm/ns for NE104 and 15.0 cm/ns for Bicron 400. This measurement gave a position resolution of 2.5 cm.

Although these two measurements provide us with position measurements of very similar resolutions, the position obtained using time difference was more immune to gain drifts and worked better even in an environment with δ rays (given that the δ rays go through the counter in the vicinity of the particle position which we are measuring). Position by pulse heights are useful in the deflected region counters where TDC thresholds are marginal for minimum ionizing particles due to low gain setting in the PM tubes.

The position resolution in the direction perpendicular to the long dimension of the scintillators was taken as half width of the scintillation plates used.

B U/Cu Calorimeters

The performance of U/Cu calorimeters with test beam data has been described elsewhere [44]. In this section, the offline corrections which are applied to obtain optimum resolution with peripheral 1p and 1n events are described. In addition, studies on gain drifts and response to ^{28}Si beams are given.

1 PM gain drifts

The photomultiplier gain stability is a major factor contributing to the energy resolution in U/Cu calorimeters. During the normal data taking period, the accelerator, which delivers the beam to the experiment, fails to provide an uninterrupted beam throughout the run. The sudden changes in the working conditions affect the photo tube gains, degrading the resolution. In addition, it affects the trigger condition significantly since, to make decisions, the trigger relies on the energy measurement. This imposes a severe limitation on the choice of photomultipliers available in the market.

We have developed a photomultiplier test setup which simulates the AGS operating conditions. Figure 3.5 shows a schematic of the test setup. The background

uranium noise for the phototubes was simulated with a slow pulse (red LED) of frequency $\sim$1 sec and the light generated by a true beam particle was simulated with a fast pulse (green LED) of frequency $\sim$1 μsec. both of which could be controlled externally through a PC driven data acquisition system. Phototubes were mounted inside a light-tight box. and the anode signals were connected to a 2280 ADC system via current monitors. Using this test setup. up to 55 individual photo tubes could be tested simultaneously. These tests consist of exposing the phototubes to 4 different conditions given by fast and slow pulses. The stability of the fast pulse was monitored by a reference photomultiplier which is exposed solely to the fast pulse. The temperature inside the box was monitored constantly by a temperature sensor mounted next to the slow pulse.

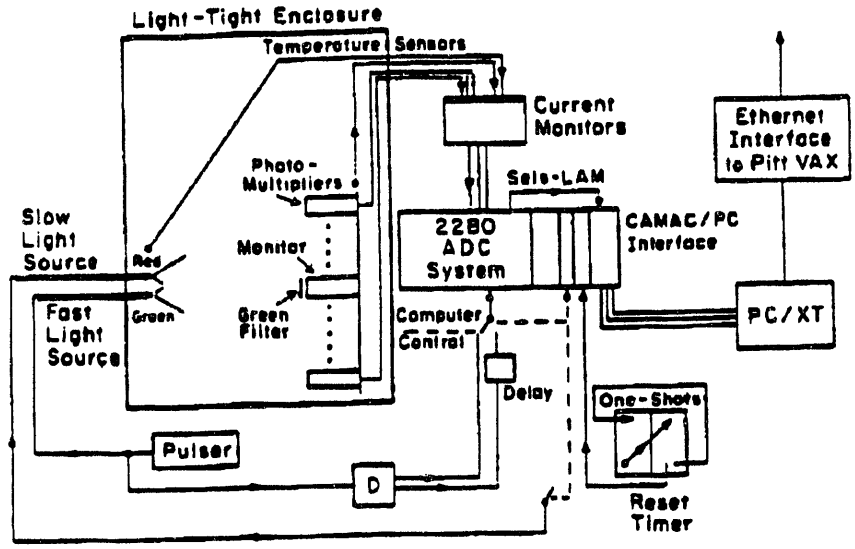

Figure 3.5: Pitt photomultiplier test facility with data acquisition setup.

We carried out tests for 100 R580-16 Hamamatsu photomultipliers. Our tests confirmed that. even for currents as high as 200 μA the short term gain variations are less than 1%. Figures 3.6 (a) and (b) show a long term variation of two of the Hamamatsu tubes. Although the short term variations of the two phototubes are similar to each other. the long term variations in one phototube is twice as large as in the other. The tubes which show minimum variation were selected by this test facility and used in places where heavy average currents and abrupt changes in running conditions are expected (Primarily in the deflected beam region).

2 Noise corrections

Although the calorimeters are calibrated every 24 hours. due to signal ground shifts. the energy measurements varied between calibrations. Any variation in the High Voltage power usage between calibrations can introduce shifts which are not present at

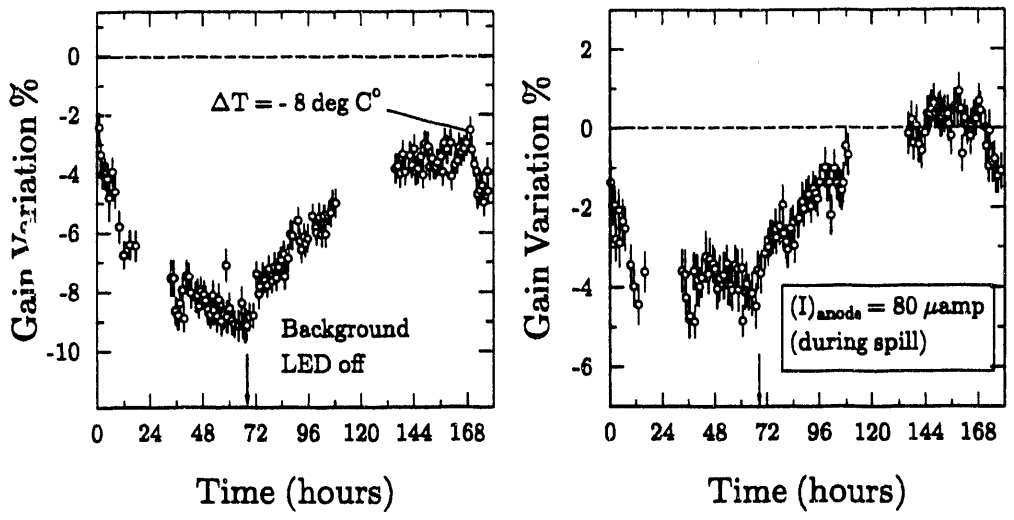

Figure 3.6: Gain drifts in two hamamatsu photomultiplier tubes.

the time at which the calibration takes place. In addition, any faults in the calibration procedure due to noise problems could change the absolute energy calibration.

The blackened photo tube, which does not see any light generated either by real particle showers or uranium noise, gives us an excellent system to monitor the effects of signal ground shifts over a large period of time. This effect was corrected event by event between calibration runs, assuming the blackened phototube pedestal shift as the true pedestal shift in all photo tubes in the offline analysis.

3 Cluster Finding

Cluster finding in the UCALs play a very important role in determining the energy of the incoming particle. Hadronic showers in our calorimeter modules usually extend over several towers of 10x10 cm^2 area and a cluster finding algorithm should recognize the towers which contain the real energy deposit. Energy sharing between showers due to multiple hits in the same vicinity or energy leakage due to the cracks between the calorimeter modules, complicate this analysis.

In the proton and the neutron calorimeters, the cluster search was performed in a very similar fashion. Initially, the number of clusters was identified by selecting the number of cells having an energy above a given threshold. Here, a cell refers to a light decoupled section. For proton and neutron calorimeters, the threshold energy was defined as 5.0 GeV. The total raw energy was computed by adding all signals together and this was compared with the expected energy which was calculated using the hit multiplicity, assuming each particle will deposit an energy of 13.8 GeV in the calorimeter. If the raw energy exceeded the expected energy by more than 2σ, where σ was taken to be $0.35/\sqrt{E}$, more clusters were searched until the expected energy was within 2σ of the raw energy. This procedure was introduced so that clusters

which deposit a low energy in the hit cell, due to shower fluctuations or to particles going through the cracks between calorimeter modules, would not be overlooked.

The cluster energy was computed by taking the energy summed over a 3x3 cell area. Cells which share the energy between clusters were marked and this energy was divided among the clusters, but the main cell (cell in the middle) energy was not allowed to be shared between clusters. Finally, an additional check was made on each cluster to identify the events in which two particles passed through the same cell but were identified as one. Clusters in which this occurred were split and marked as two clusters. Figures 3.7 (a) and (b) show the measured raw energy distributions for protons and neutrons where the cluster analysis was performed. An energy resolution of $\sigma_E/E = 0.8/\sqrt{E}$ (where E is measured in GeV) was observed after the cluster analysis.

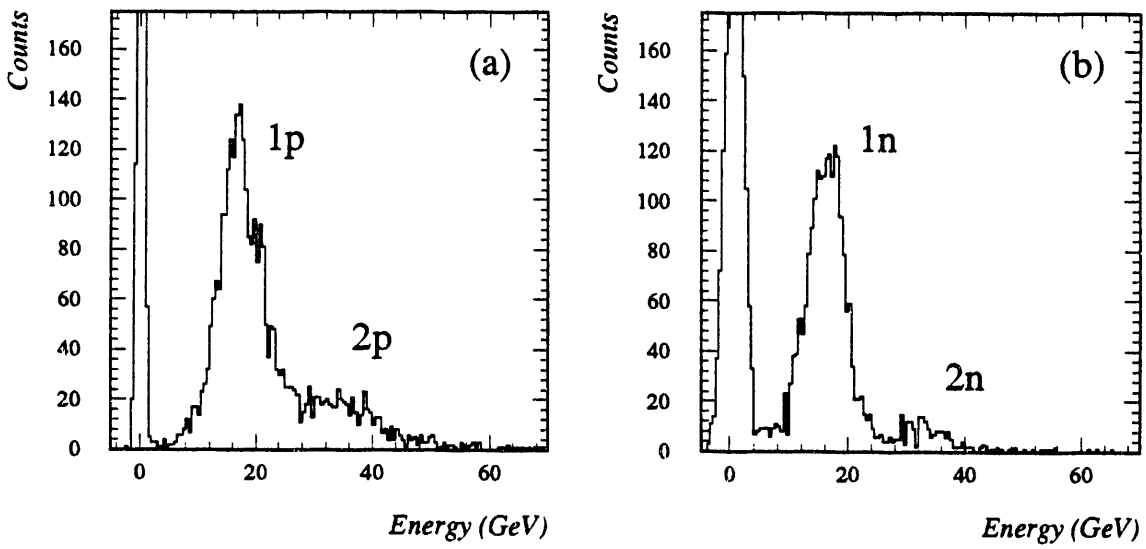

Figure 3.7: The measured raw energy distributions. (a) Protons. (b) Neutrons.

The energy deposited in the deflected beam region by pure beam particles or heavy ion fragments extended roughly over 5 calorimeter modules and hence no cluster analysis was performed. In this region, the energy was computed by taking the raw sum over 5 calorimeter modules surrounding the module with the maximum energy (hit module).

4 Position Measurement

The information about the hit position of the particles in these calorimeters can be extracted by using the energy deposited in the cells surrounding the hit cell. Out of various possible combinations, we have selected the form,

$$POS = A \times \ln\left(\frac{E_1}{E_2}\right)$$

To evaluate the X position in neutron calorimeters, two phototubes viewing the hit tower were selected as E_1 and E_2. For proton calorimeters, two cells to the left and the right of the hit cell were selected and for the beam region, two towers in the neighboring calorimeters were selected. The constant A was found to be 9.5, 1.5 and 2.8 for the neutron, the proton and the beam region calorimeters respectively. The formula to extract the X position given in reference [44] works equally well for these calorimeter modules.

For the Y position estimate, the towers above and below the hit tower were selected for E_1 and E_2 in the neutron and the beam region calorimeters. In the proton region calorimeters, the top and bottom cells were selected. The extracted values for the constant A are 1.8, 1.5 and 2.2 for the neutron, the proton and the beam region calorimeters respectively. For the beam calorimeter, which is a totally unsegmented module, an additional factor of 2.3 was used, bringing the constant to be roughly 5.1. A position resolution of 2.0 cm and 2.5 cm for X and Y respectively, was obtained for the neutron calorimeters. Similar position resolutions were observed for the proton region and beam region calorimeters.

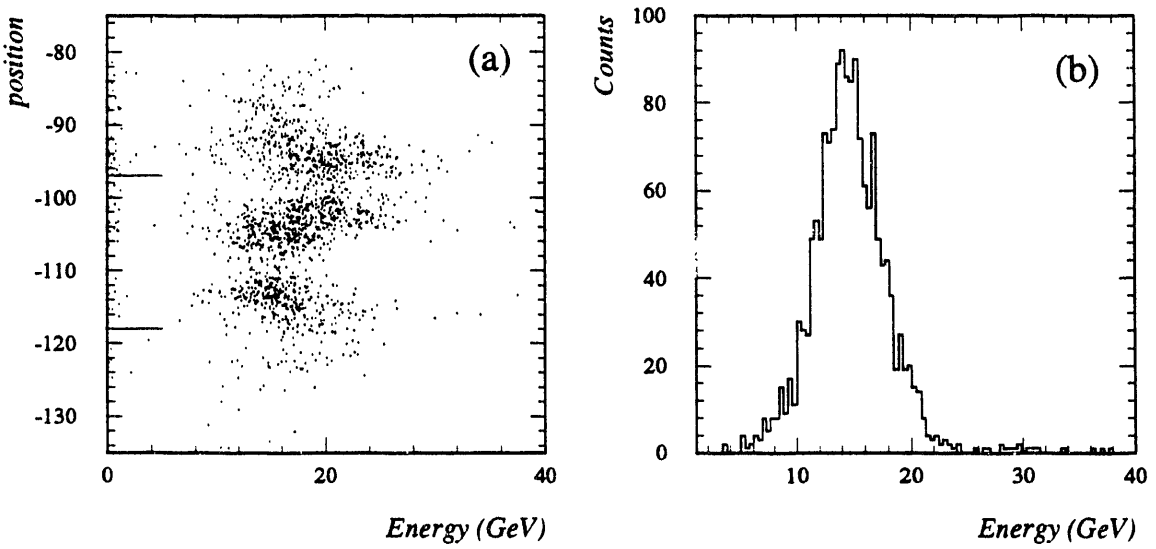

Figure 3.8: Position dependence on measured energy. (a) Position vs. energy. (b) Corrected energy distribution.

5 Energy Resolution

In order to achieve the maximum resolution from the calorimeters, it was necessary to correct for position dependent response. Figure 3.8 (a) shows the measured X position against the measured cluster energy for peripheral protons. The two pointers indicate the location of the cracks between the calorimeter modules. This plot shows that the calorimeter response is low for showers which originate at the center and that it increases steadily when it moves towards the edge of each calorimeter module.

By assuming the relationship between the position and the measured energy to be linear for a given energy, the following correction was applied on the measured energy.

$$E_c = E\left(1 - x\frac{A}{E}\right)$$

Figure 3.8 (b) shows the corrected energy distribution after all the corrections were made. This correction improves the resolution to $\sigma_E/E = 0.6/\sqrt{E}$. This is still higher than the value of $0.35/\sqrt{E}$ seen for the calorimeters when they were segmented longitudinally into an EM and hadronic sections [44]. No dependence of the response on the Y position was observed.

6 Shower Fluctuations

Among the factors that contribute in degrading a calorimeter resolution, the response of a calorimeter to a pure electromagnetic and to pure hadronic showers (e/π ratio) plays a very important role. [52, 53]. Particles deposit their energy as electromagnetic and as hadronic showers. Electromagnetic showers are well concentrated in the direction of the path of the particle compared to the hadronic showers which spread more in the lateral direction. In addition, electromagnetic showers produce a better energy resolution than hadronic showers due to smaller shower fluctuations. Depending on the fraction of the electromagnetic to the hadronic energy in the created shower, the response of the calorimeter can fluctuate (unless e/π=1).

Figure 3.9 (a) shows a scatter plot of maximum cell energy against the cluster energy computed for peripheral neutrons. This plot indicates that the concentrated showers produce more energy than the showers which are spread out among several cells. A recipe for correcting this effect can be found in the literature [54] and with a slight modification to fit our data is,

$$\bar{f}_i = A f_i\left(1 - f_i\frac{B}{\sqrt{E}}\right)$$

where A=1.23 and B=0.15 are constants found by minimizing the $\chi 2$ to force the sum of the $\bar{f}_i$ to be 13.8 GeV where i refers to the individual phototubes. Here, E is the total cluster energy, f_i is the individual readings from each phototube and $\bar{f}_i$ is the reading after correction. Depending on the energy in each cell, this correction factor generates different weighting factors. The constant A was introduced as an energy normalization parameter.

Figure 3.9 (b) shows a histogram after applying this correction, which brings the resolution to $0.5/\sqrt{E}$, which is still larger than the resolution obtained before the calorimeters were modified. The modifications to the original design which were described previously, could be a major source for this degradation of the resolution.

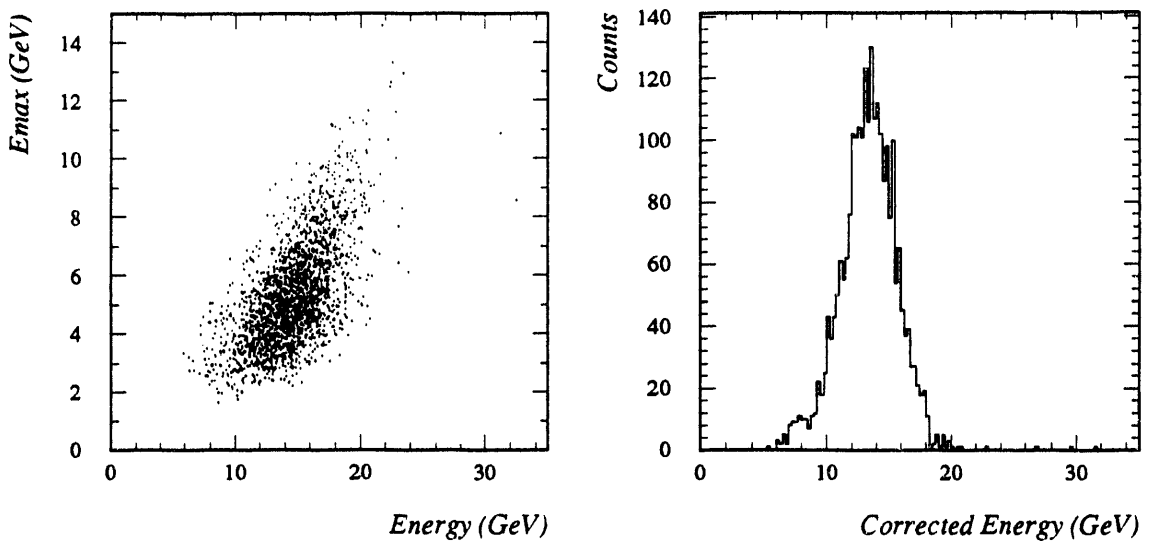

Figure 3.9: Shower fluctuations. (a) Maximum cell energy vs. the total energy. (b) Energy after correcting for the fluctuations.

C Tracking Chambers

The information from tracking chambers was processed in two steps. The first step, which is described here, deals with the preliminary pattern recognition and noise elimination, and the second step, which is described in chapter 5, deals with more rigorous analysis that pushes the chambers to their limits.

1 Pad Section

1.1 Noise corrections

In general, the noise in the pad sections of the tracking chambers does not require tedious corrections since the noise rms is only about 10-20 ADC counts in a scale where minimum ionizing particles produce a charge corresponding to about 200 ADC counts. Although there are serious noise problems in DC2 and DC3, especially in the regions where large pads are located, no attempt was made to correct these problems since they did not interfere with the regions with which this analysis is concerned. A full description of most of the noise problems in DC1 are well described in reference [55], and only the relevant problems are discussed here.

Occasionally, pads along some anode wires in DC1 reported negative signals which were large enough to wipe out the minimum ionizing signals. Figure 3.10 (a) shows an event of this type. Here, the squares represent positive signals and the circles represent negative signals. The area represents the amount of charge in each readout node. A reason for this offset could be a poor connection between the anode wire and the isolating capacitor which provides an AC ground.

This problem was corrected by taking the average of the negative signals along the

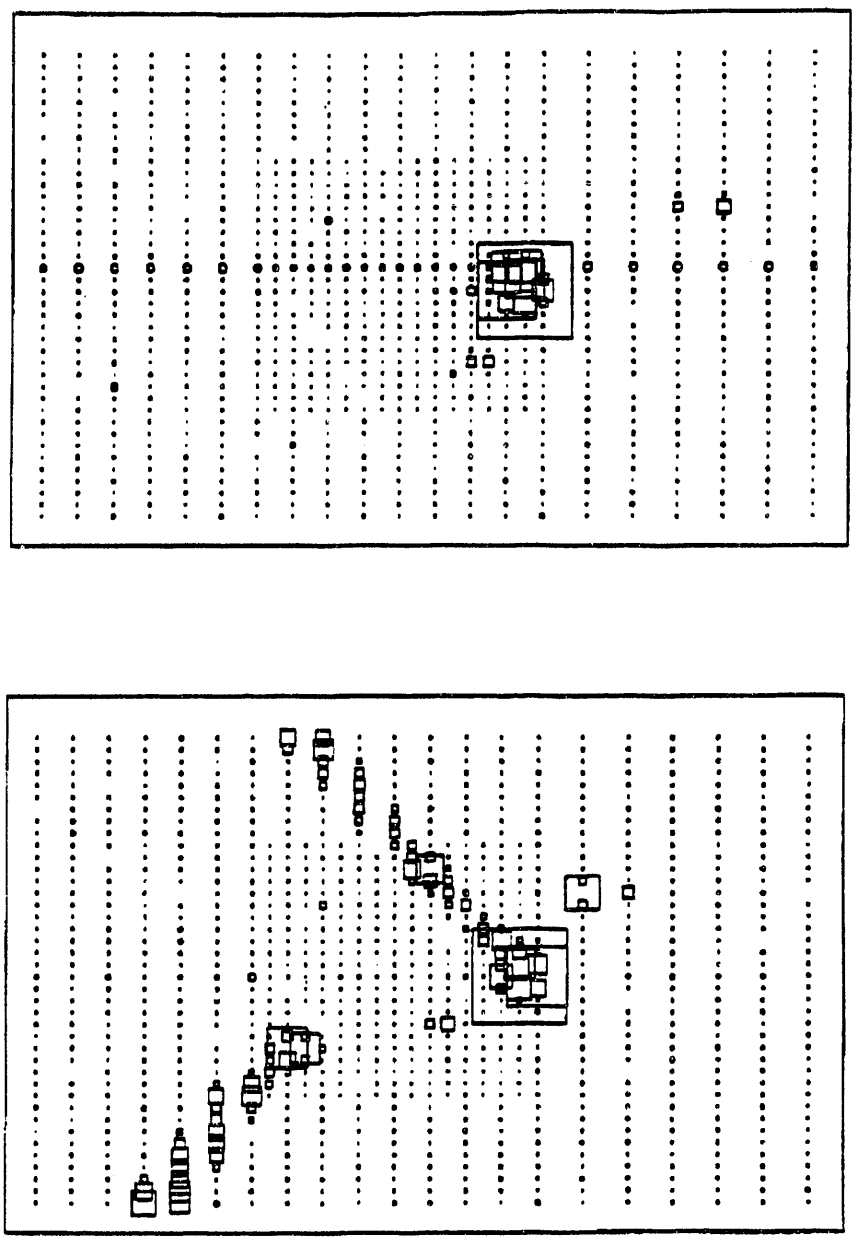

Figure 3.10: DC1 event display showing two common problems induced by the heavy ions passing through the chamber. (a) Negative signal shift along anode wire. (b) Two δ rays emerging from a heavy ion cluster. Ref [55]

anode wires in the region of the chamber where no peripheral protons were seen. For the correction, size differences in the readout nodes in different regions were taken into account. Since this problem was not observed in DC2 and DC3, no special corrections were applied to the pad sections in these chambers.

1.2 Cluster finding

The cluster finding in the pad sections were initiated by searching for single hits which deposited above 100 ADC counts. A cluster was defined as the selected hit and its two closest neighbors along the anode wire, beneath the hit pad. These two neighbors were not counted as a new cluster. A heavy ion hit produces a large amount of charge in the pad sections around the hit location. For this reason, hits inside a given window around the maximum hit for any single event, were not taken as new hits. Different size windows were used in the three chambers for this purpose. After extracting all the clusters, the total cluster charge was computed by taking the sum of the three signals. The cluster with the maximum charge was defined as the heavy ion hit.

The δ rays originating from the heavy ions make cluster finding very difficult. Figure 3.10 (b) shows an event with two δ rays originating from the heavy ion location. The amount of charge deposited by these δ rays can easily confuse the minimum ionizing signal. In addition, it can degrade the position resolution in these chambers. No corrections were applied in this analysis to correct for the effects arising from δ rays due to the poor understanding of their effect on the pad sections.

1.3 Position using the data from the Pads

An excellent description of the position estimation in pad chambers is given in reference [55]. The suggested method uses the property of charge sharing between pads which is a characteristic of this type of chamber. Figures 3.11 (a) and (b) show the charge ratio plots for heavy ions and protons passing through the chamber DC1. Here, Q_l, Q_m and Q_r define the three signals belonging to a cluster. Of these three signals the middle signal Q_m has the maximum charge. The width of the band represents the position resolution in the chamber. Any effect due to δ rays will cause the ratio to fall outside this band.

The suggested centroid finding formula for these chambers is,

$$POS = \frac{Q_{i-1}X_{i-1} + Q_iX_i + Q_{i+1}X_{i+1}}{Q_{i-1} + Q_i + Q_{i+1}}$$

assuming the charge distribution is spread over 3 readout nodes. Here, X_i and Q_i represent the position and the measured charge at readout node i.

Figure 3.12 (a) shows the position measured by the vertex detector extrapolated to the DC1 plane, against the position measured by DC1 for beam tracks taken with no target in the target holder (empty target). Figure 3.12 (b) shows the difference

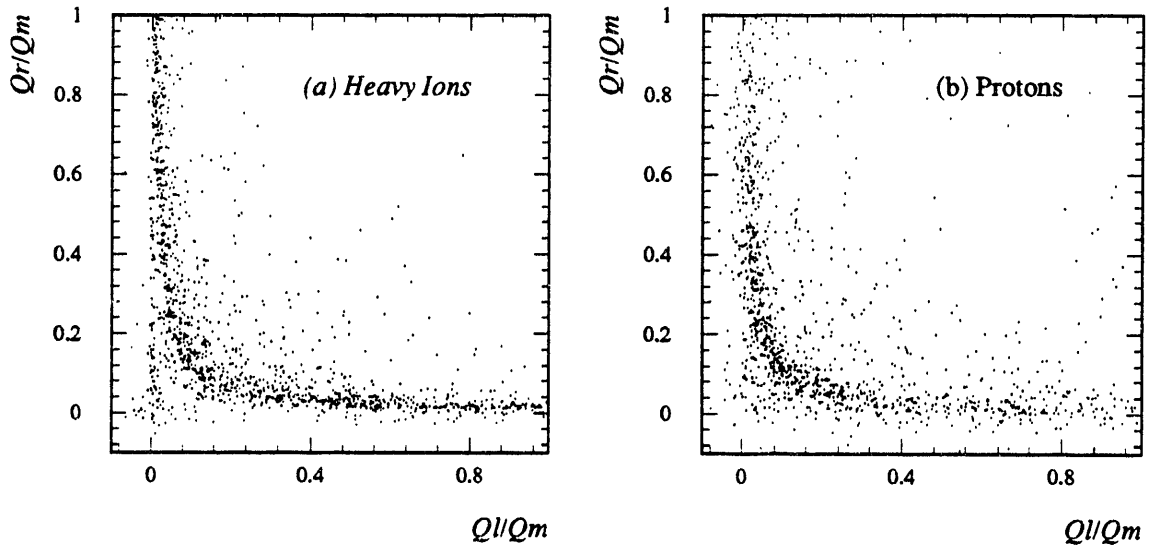

Figure 3.11: Charge ratio plot. (a) Heavy ions. (b) Protons.

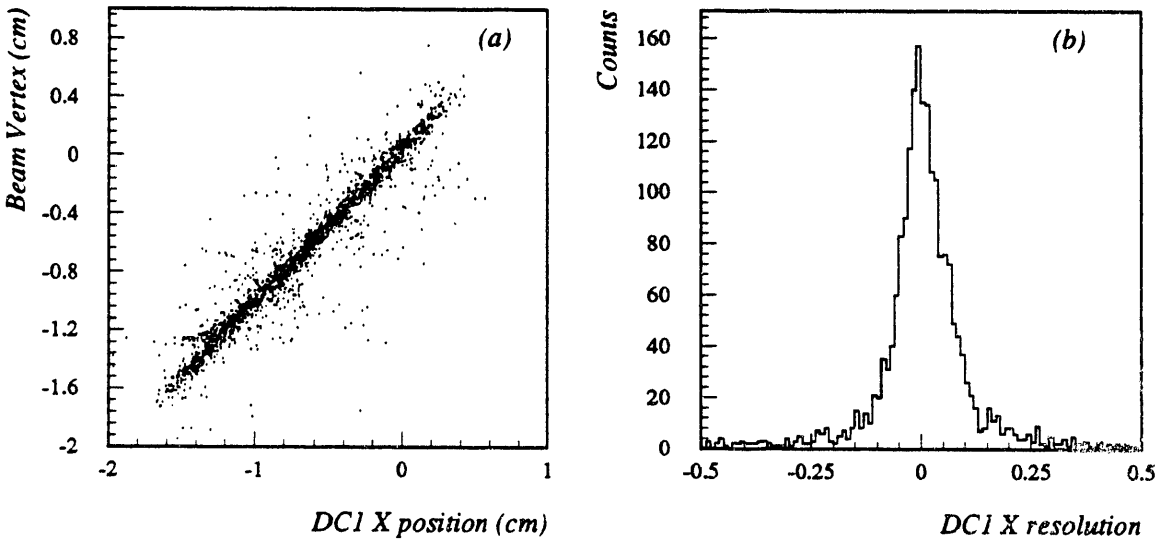

Figure 3.12: DC1 resolution in the x position measurement. (a) Beam vertex measurement extrapolated to the DC1 plane vs. the DC1 x measurement. (b) The difference between the two measurements.

between the two measurements. The width of this distribution is about 500 μm. Accounting for the contributions from multiple scattering and the vertex detector resolutions, we estimate the DC1 resolution to be about 200 μm. This value is twice the value of the expected resolution with x-ray measurements. But x-ray measurement studies show that, at higher charge levels, the position resolution is degraded due to the spreading of the avalanche along the anode wire. In addition, the δ rays adversely affect the position resolution in these chambers.

This formula is modified slightly when it is used with the chevron shaped pads in DC2 and DC3. Charge sharing between chevrons occurs mostly between two pads, and therefore only two terms were used for the position estimate. Out of the two possible pad neighbors, the pad with the higher charge was selected. Preliminary results showed that the algorithm tends to pull the position distributions towards the edge of the hit pad. In order to correct for this effect, a constant was introduced to shift the centroids and the modified formula reads.

$$POS = \frac{Q_m(X_m \pm A) + Q_s(X_s \mp A)}{Q_m + Q_s}$$

where Q_m and X_m refer to the hit pad charge and the position respectively and Q_s and X_s refer to the same quantities for its selected neighbor. The sign of the constant A was selected to pull the distributions towards the center of the hit pad and it depends on the location of the neighbor in the physical chamber with respect to the hit pad. The optimum value of A was $\sim$10% of the length of the hit pad.

Figures 3.13 (a) and (b) show the measured Y position distributions for beam tracks in DC2 and DC3 plotted against the reconstructed position distributions extrapolated to the planes of each chamber assuming the tracks pass at target Y=0. When calculating the reconstructed position, the chamber to be tested was taken out of the fit. These distributions yield us a position resolution of 2.5 mm for DC2 and 5.0 mm for DC3. These results indicate that chevrons produce a resolution which is approximately 10% of the size of the chevron.

2 Drift Section

2.1 Noise Elimination

Due to the presence of δ rays created by the heavy ion tracks, a typical peripheral event produces a large number of TDC hits in drift wires. Compared to central events, track reconstruction of peripheral events becomes rather difficult due to this reason, and this forces the offline analysis to develop fast pattern selection algorithms. These chambers were developed and constructed especially to deal with heavy ions and therefore peripheral events, with a high Z particle in the final state, can demonstrate that the chambers perform up to the expected standard.

Figure 3.14 (a) shows a histogram of observed TDC counts for wires in a single plane of DC2 for a collection of tracks produced by the presence of a single proton

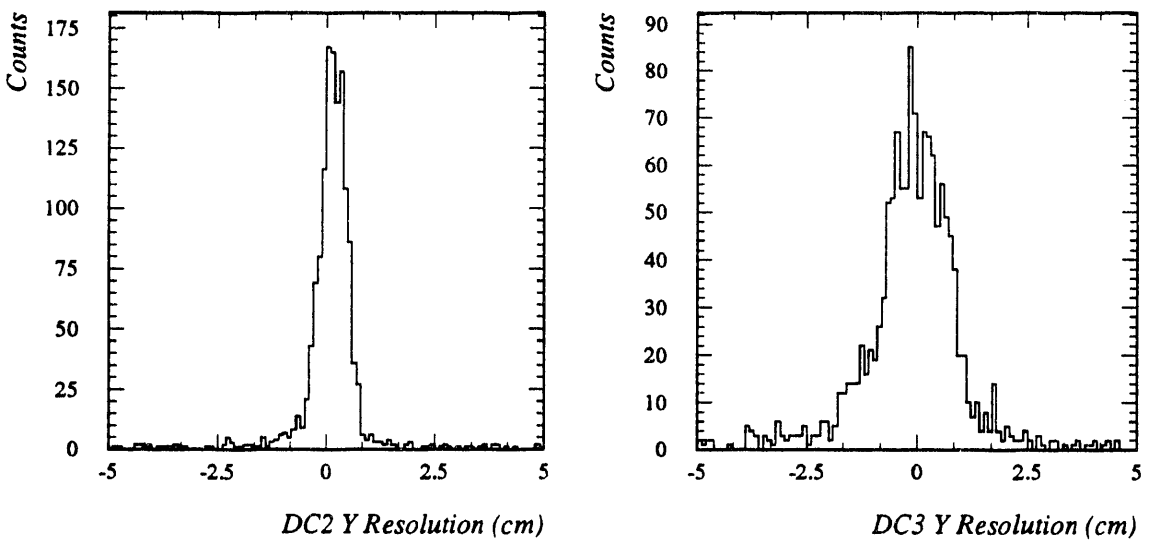

Figure 3.13: Measured y position resolution by chevron pads (a) Difference between the DC1 measurement extrapolated to the DC2 plane. and the DC2 position measurement. (b) Same for DC3.

and a heavy ion. Every wire with a "hit" makes one entry for each event. Although we can recognize the heavy ion and the proton as two distinct peaks. the background noise in the chamber makes it cumbersome to do any reliable pattern recognition without selecting genuine TDC hits that belong to the two tracks. This is specially applicable to heavy ion tracks since most of the hits that originate from δ rays appear as genuine TDC hits at first glance.

The pad plane in each drift chamber can pin-point the pad wire at which the heavy ion track traverses since it carries the information about the charge. This is a useful way to remove the uncorrelated TDC hits in the drift sections. For the heavy ion track. due to its tight rigidity. the bending angle remains close to 60 mr. This allows us to select the true TDC hits that originate from the heavy ion track. from two wires (in each drift plane) which are closest to the pad wire at which the heavy ion was seen. For other tracks. 3-4 wires were allowed. depending on the location of the track. Figure 3.14 (b) shows the same wire plane after removing the noise. The proton and heavy ion hits are clearly visible in this plot.

2.2 T_0 Corrections

For drift chambers. T_0 defines the measured time for a track passing any given drift wire at a zero distance from the wire location. Due to the time delays in the cables and the electronic modules. T_0 differs for each wire. The online calibrations described in chapter 2. are expected to provide the initial T_0 corrections to bring the drift time in different anode wires to one common scale by taking into account the differences in cable lengths, delays in electronic paths etc.

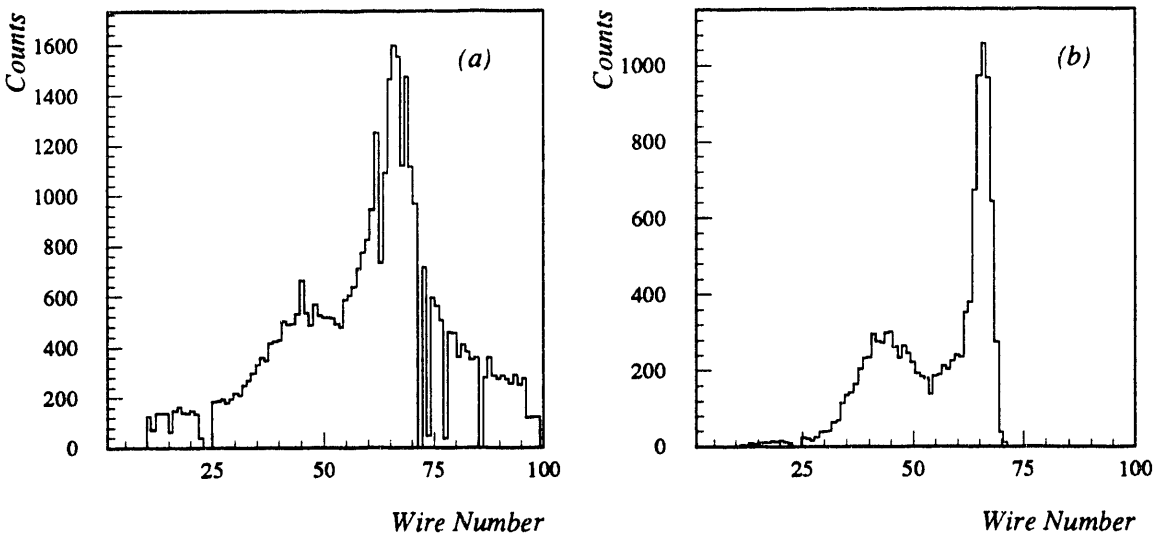

Figure 3.14: Average TDC hit distributions in drift planes in DC2. (a) Raw distribution. (b) Distribution after cleaning by a comparison with pad hits.

The T_0 constants were studied by using the peripheral protons and heavy ions. For most of the wires, the calibration constants provided very good results. For the wires for which these constants did not work, new constants were generated.

For DC2 and DC3, the T_0 values for heavy ion tracks and proton tracks differ. This could be due to the slewing effects [2] in the leading-edge discriminators since heavy ions produce much larger electron clouds than protons. To correct this effect, additional corrections of 5 nsec for DC2 and 10 nsec for DC3 were used for roughly 10 wires in each chamber where the heavy ion traversed. A variation of 3-5% was observed for T_0 constants in the two chambers.

2.3 Non-linearity in Drift Cells

To convert the timing signals to position, the following formula was used,

$$POS = V_d(T - \eta) + \Delta$$

which is a linear relation. Here, T is the measured timing, V_d is the drift velocity, and η and Δ are offset constants. Δ was introduced to correct for the shift between planes which is 0.0 for odd numbered planes in each chamber, and 0.3175 cm for DC2 and 0.6350 cm for DC3, for even numbered planes. V_d and η are 0.52 cm/nsec and 245 nsec for DC2 and 0.52 cm/nsec and 280 nsec for DC3 respectively. The observed drift times for drift cells in DC2 and DC3 were 60 nsec and 120 nsec respectively.

Although the used formula is a linear relationship between time and position, the drift time has a non-linear behavior. Figure 3.15 shows field lines and equipotential

[2] see section 4.1 in this chapter

lines for a double cell in the drift section. The tracks which pass the chamber at the boundaries take much longer to reach the anode wires. Figures 3.16 (a) and (b) demonstrate this behavior for beam tracks passing through chambers DC2 and DC3 respectively. Here, the position was estimated by assuming a uniform track density from the center of any given drift cell to its edge.

For the data analyzed here, no corrections were applied to correct for this non linearity.

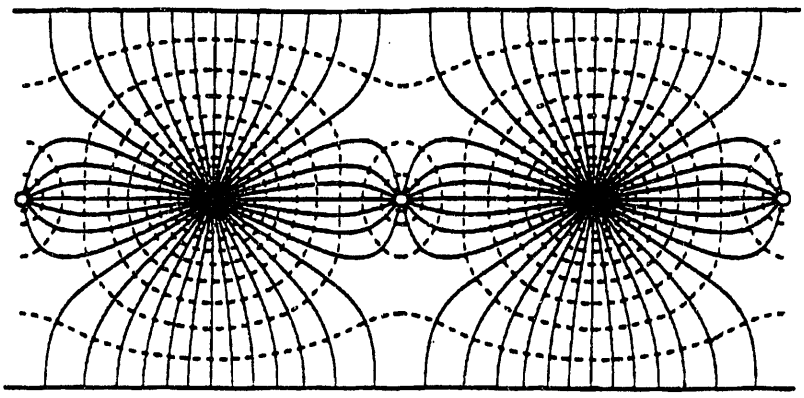

Figure 3.15: Equipotential and field lines for drift cells used in DC2 and DC3 chambers. Ref [55]

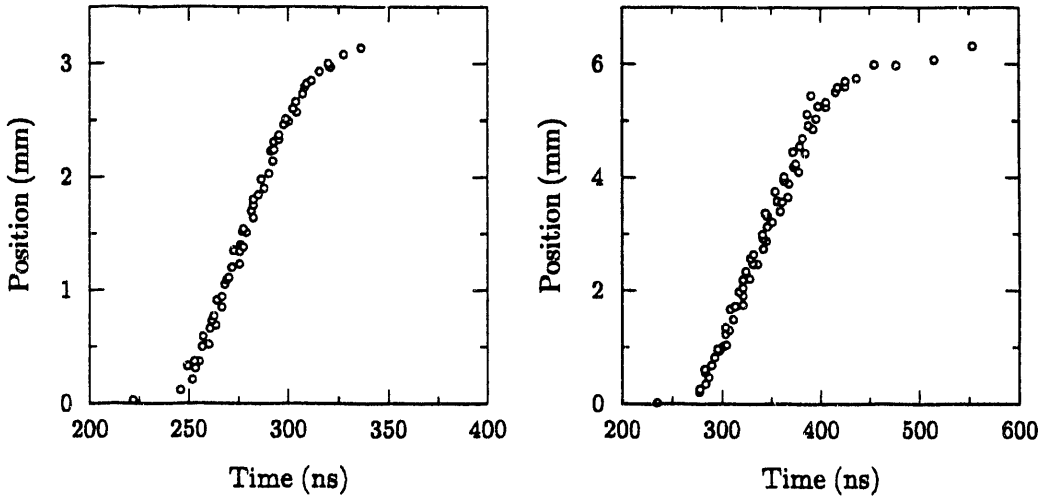

Figure 3.16: Non linearity in drift time measurement. (a) Track location vs. drift time for DC2. (b) Same for DC3.

2.4 High Level TDC information

E814 tracking chambers have a unique feature to produce two or more TDC hits from the same charge cloud. The first signal is generated by a leading-edge discriminator whereas the succeeding signals are generated by a zero-crossing discriminator. [3] The zero-crossing discriminator thresholds were set so that they do not respond to charge clouds originating from minimum ionizing tracks and hence true heavy ion hits can be selected by omitting the noise signals from δ rays.

In preliminary pattern recognition, second hits or so called high level TDC information was not used. A discussion on how these could be used to help pattern recognition is given later.

[3] see chapter 2, section 3.3

CHAPTER 4

Selection of Electromagnetic Interactions

In this chapter, a full description of the peripheral trigger setup, the data reduction methods and the cross section estimations for simple decay channels produced by electromagnetic interactions is given. This analysis was later combined with a more rigorous analysis developed to study complex decay channels.

A Online Selection

As described in chapter 2, the main purpose of the trigger is to make fast, reliable decisions about given events, whether they should be accepted or not, by studying the limited number of signals obtained from various detector systems. An efficient trigger allows the data acquisition system to store only the interesting events and it does not waste time over uninteresting events.

1 Peripheral Trigger

The selection criteria for the peripheral trigger is based on the selection of events which produce low activity in the target region detectors. In addition, to reduce the background and to enhance each event type, the trigger was set up to select events with a substantial charge in the heavy ion region ($Z/A \approx 1/2$) and energy in the proton and neutron region calorimeters. The selections varied depending on the type of trigger that was used.

The trigger takes about 20 μsec of processing time to analyze a peripheral event. Due to the beam rates used in our experiment ($\sim 10^5$ particles/sec) the beam particles are spaced by only a few μsec. Thus, it is not possible for the trigger to analyze and make decisions about every beam particle fully. Due to this reason, the trigger was implemented in several parallel processing stages [37] with different processing times that depend on the number of elements used in the trigger decision. As a result, no time was wasted over events which were identified as uninteresting events, and only the events which were good candidates for a given physical process were analyzed fully before the final decision was made. A description of each type of trigger is given below.

- *Beam triggers* – Beam triggers are the most unbiased triggers in the experiment and are very useful for measuring efficiencies of more complex triggers. They are defined by the signals extracted from the 4 beam scintillators S1-S4. Good ^{28}Si beams are identified by the pulse height corresponding to Z=14 in S2 and S4 with no hits recorded by S1 and S3.

- *Pre-triggers* – The pre-trigger is the first signal which indicates that a possible interaction has occurred. This is formed by the coincidence of the beam trigger and the energy sum in the proton or the neutron region calorimeters. The pre-trigger initiates the process of digitizing information from all detectors, including the FERA ADC's which are used in the second level trigger. The pre-trigger can be taken as a "minimum bias" trigger for most of our applications. These events are also useful in studying efficiencies, as they are richer in interesting events compared to the beam triggers.

- *First Level trigger* – The purpose of the first level trigger is to look for beam particles which are closer than 1μsec from the previous beam particle. If the pre-trigger is generated by such a particle, it will send CLEAR signals to all the detectors in the experiment to abort the digitization and to be ready for the next event (after protection).

- *Second Level trigger* – The second level trigger makes the final decision based on the FERA data about a given event. In the case of peripheral triggers, the information from the target region veto detectors (multiplicity detector, downstream veto wall, participant calorimeter, target calorimeter, and magnet scintillators) and the downstream detectors (downstream silicon detector, downstream forward scintillators, and the energy sum in calorimeter modules) was used. The triggers generated with the aid of all the detectors listed above were marked as triggers with online vetos and the triggers generated without the target region detectors but using the downstream calorimeters and forward scintillators were marked as triggers without online vetos.

- *Parallel Triggers* – The E814 data acquisition can accept only up to 30 events per spill. If individual triggers have rates higher than this, the events which are more abundant would be collected more frequently. To prevent this, the trigger system was designed to allow data taking with parallel triggers, with the ability to accept only a fraction of the triggers in any given channel (we call this process "downscaling"). In this manner we are able to enhance rare event types.

In addition to the second level trigger, several other triggers were activated to study gain variations and other systematic effects. They are the beam triggers, the pre-triggers and the MT triggers (random triggers with no beam particle present, generated through a random pulser). The frequency of these triggers were adjusted

to give a rate of about 5% of the events taken with the second level triggers. The downscaling factors are software loadable and the typical values used in the 1990 run are listed in Table 4.1.

Table 4.1: List of parallel triggers with their downscaling factors.

Trigger Type	Downscaling factor
1p	16
1n	8
2p	3
2n	1
3p	1
3n	1
Pre-triggers	2001
Beam triggers	4001
MT triggers	22

2 Scalers

There are several types of scalers used in the experiment for various measurements. They are:

- *Spill Scalers* – Spill scalers keep track of the total number of beam particles, the number of gated beam particles (as defined by the beam telescope), and the number of events that are used in each trigger. They are read out and cleared at the end of each spill. These scalers are essential for cross section measurements.

- *Latching Scalers* – Latching scalers are used to measure the time at which each event occurred with respect to the previous beam particle, the beginning of the spill, the phase of 60Hz power lines, the previous clear etc. In addition, these are used to measure the instantaneous rate of the beam. These scalers are useful to study noise problems and other electronic problems.

- *Down Scalers* – The sole purpose of down scalers are to prescale different triggers so as to equalize their rates as described earlier. A section of these scalers are used to count the total number of triggers of a given type that is read out at the end of the spill.

3 Data Sample

The data selected through the online trigger requirements were written on 6250 BPI magnetic tapes. A data taking "run" consists of data taken until a tape is filled, which

corresponds to approximately 8,000 to 9,000 complete, independent, event records. Each tape is labeled according to the order in which the data have been recorded.

The recorded peripheral data sample consists of two major parts, namely, a single nucleon emission (1p or 1n, designated as the 1p-1n sample) and two or three nucleon emissions (2p, 2n or higher, designated as 2p-2n sample). These were recorded over 6 different targets, and included the data taken with an empty target frame. In addition, a majority of the events were recorded with an online trigger requirement to enrich the data sample. To study trigger efficiencies, a small percentage of the data were taken without the online veto requirement. The recorded data sample is shown in Table 4.2.

Table 4.2: List of magnetic tapes written for each target and each trigger type.

Target	1p-1n	2p-2n or rare	Pre-trigger	Beam trigger	Pulser
Pb	8	36	6	6	6
Sn	7	36	3	3	3
Cu	3	37	3	3	3
Al	5	35	3	3	4
C	3	-	-	-	-
MT	4	33	3	3	3

The original data written in 6250 tapes were copied onto 8mm tapes which were read via exabyte tape drivers. Each 8mm tape is used to record up to 12 independent runs from 6250 tapes organized according to the target and trigger types. The peripheral data sample consists of 6 8mm tapes for 1p-1n triggers and 22 tapes for 2p-2n or rare trigger types. The total sample consists of about 2,400,000 events. These were fully analyzed in a Silicon Graphics computer (Personal Iris).

B Offline Selection

A large portion of the data written in the original 8mm tapes cannot be considered as good candidates for peripheral collisions, due to various factors such as interactions upstream and downstream of the target, problems in the detectors during the data taking run, etc. The offline analysis described in this section is mainly involved in reducing the data sample, by selecting good candidates for electromagnetic or soft nuclear fragmentation. The selected data were extracted and written into a secondary set of 8 mm tapes for further studies.

All detectors were calibrated and corrected for short term as well as long term gain variations prior to the offline selection procedure.

1 Good Beam Selection

1.1 Beam Scintillators

The trigger uses the beam scintillators to identify good beam particles. However, beam particles which interact with the materials upstream of the target, or two beam particles arriving within a very short time interval (double beams) could be recorded as good beam particles by slipping through the selections in the online trigger. Therefore additional offline selections were imposed on the measurements of the beam scintillators.

Figures 4.1 (a) and (b) show the histograms of the average pulse heights measured in counters S1 and S3. Each of these counters are read out by 4 phototubes connected through light guides placed symmetrically around the counters. Due to a noise problem in one of the signals, only 3 signals were used to perform the average for S3. The tail at low pulse height is a result of a pulse height measurement being distorted by a pileup effect in the phototubes. Figure 4.1 (c) is a two dimensional histogram which shows the time measured between the event under consideration and the previous event (time after the previous beam) versus the measured pulse height in S1. The data showing candidates at short times (t<8 μs) indicate the effect due to the pileup. These events are not produced by upstream interactions. The events with pulse heights greater than 100 in S1 and 75 in S3 were rejected.

Figure 4.1 (d) shows the average pulse height measured in the S2 and S4 counters. Each of these scintillators are connected to 2 phototubes mounted at opposite ends. In this scale the pulse height corresponding to the ^{28}Si beam is normalized to 100 counts. The measurement provides a resolution of 10% for Z=14 particles. The gain variations in the phototubes were corrected on a run by run basis. Events with counts less than 50 or greater than 150 were rejected.

1.2 Upstream Silicon Detector

The upstream silicon detector provides an additional pulse height measurement to select Z=14 beam particles. Since this detector is mounted just upstream of the target, it is able to detect the interactions in the beam scintillator system. However, this detector too suffers from serious pileup effects. Figure 4.2 (a) shows the measured time after previous beam against the measured pulse height for beam particles. We observe in Figure 2 that the pileup effect occurs when the beam particles arrive within a few μsecs of each other. This is due to the contribution of the negative going tail of the previous pulse on the present pulse, since the preamplifiers used in this detector have long shaping time. Events closer than 2.5 μsec were not used in this analysis.

Figure 4.2 (b) shows the measured pulse height in this detector after rejecting the events arriving less than 2.5 μsec from the previous beam particle. A resolution of 5% was obtained with this detector. The Z=14 particles were normalized to 1000 counts in this scale. Corrections were made for gain variations on a run by run basis. Events with counts less than 750 or greater than 1250 were rejected.

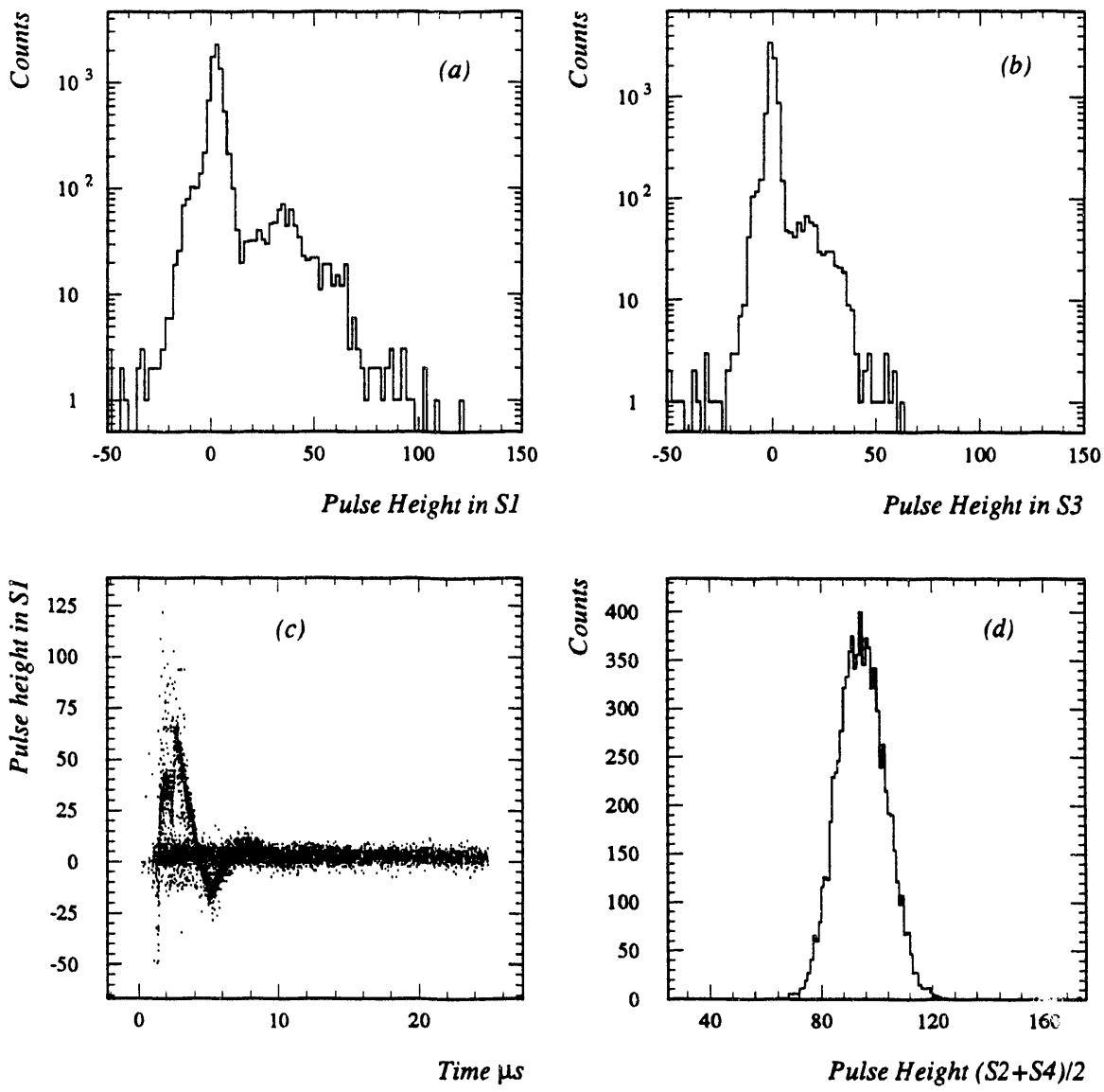

Figure 4.1: Beam scintillator system. (a) Pileup effect in veto counter S1. (b) Same for S3. (c) Pulse height in S1 vs. time after previous beam particle. (d) The average pulse height measurement by S2 and S4.

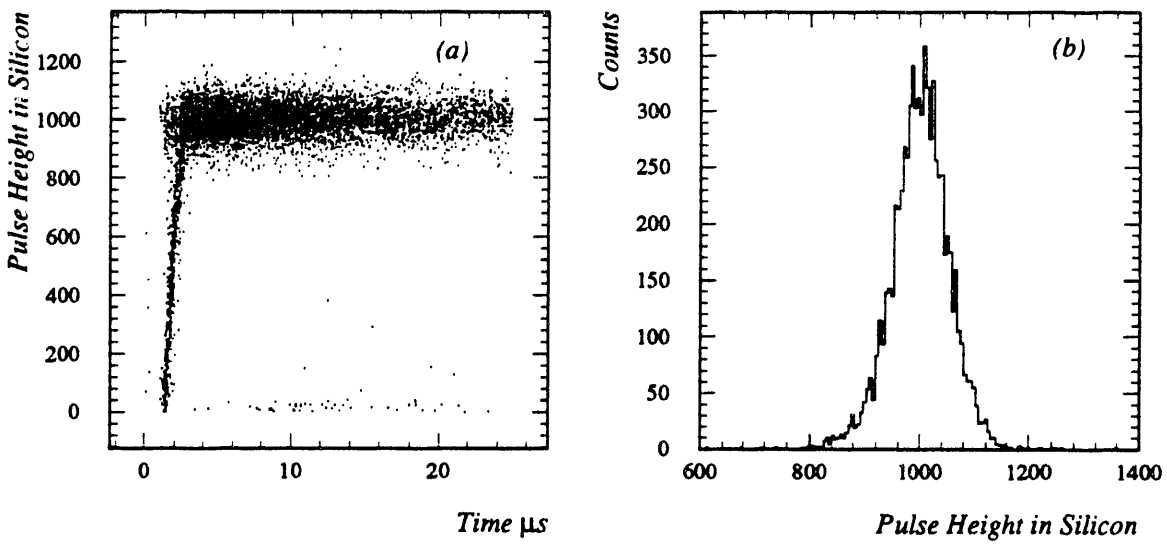

Figure 4.2: Silicon upstream detector. (a) Pulse height vs. time after previous beam particle. (b) Pulse height measurement with time after previous beam cut.

2 Data Selection

2.1 Charge Selection

After the initial interaction at the target, the heavy reaction fragments ($Z/A \approx 0.5$) travel about 30 m before detection. Although the full flight path is filled with helium gas in order to reduce the intermediate interactions, about 30% of the heavy fragments interact, producing various nuclear fragments. Due to this reason, it is very important to measure the charge of the heavy fragments at the target and at the downstream end of the spectrometer. We use the silicon detector immediately downstream of the target to measure the charge of the outgoing fragments close to the target and the two scintillator hodoscopes (vertical and horizontal) to measure the charge at the downstream end of the spectrometer. By combining all three measurements we can easily obtain a very clean charge measurement for the heavy ion fragment.

Figure 4.3 (a) shows the measured time after previous beam particle against the measured charge at the downstream silicon detector. The pileup effect (discussed in the previous section) makes it hard to select individual charge species below 2.5 μsec. Figure 4.3 (b) shows the histogram of the measured charge distribution after applying the cut on the time after previous beam. A resolution of 4% was observed in this detector for Z=14 particles. This measurement, as it is, is not good enough to make a clean charge identification.

Figure 4.4 (a) shows a scatter plot of the measured charge in the vertical scintillator hodoscope against the measured charge in the horizontal scintillator hodoscope. The scintillator signals were corrected for the saturation effects discussed in the previous chapter. The plot indicates that the combined charge measurement from these two detectors has a better charge separation than the individual measurements. Figure

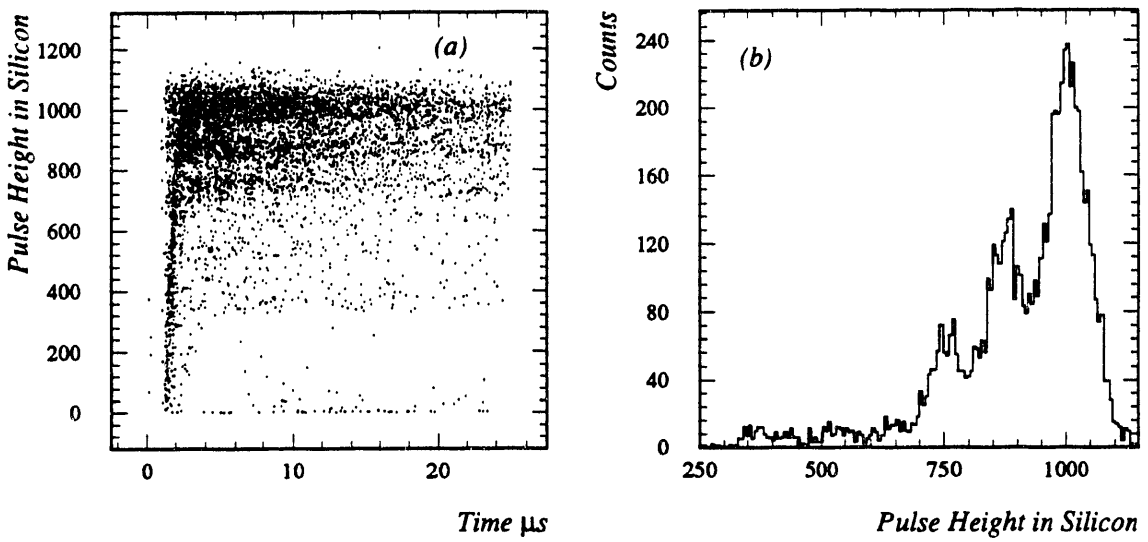

Figure 4.3: Silicon downstream detector. (a) Pulse height vs. time after previous beam particle. (b) Pulse height measurement with time after previous beam cut.

4.4 (b) shows the histogram for the combined charge measurement (double charge measurement). A resolution of 3% was obtained by this method.

Figure 4.4 (c) shows the charge measured at the silicon detector against the double charge measurement at the downstream end of the spectrometer. The horizontal band of events corresponds to the events that originated as Z=14 but interacted before reaching the downstream end of the spectrometer, producing some other charge species. In order to make a clean charge identification, hexagonal shaped gates (cuts) were made on each island that corresponded to a different charge species. The events that belong to each island correspond to three independent charge measurements. Figure 4.4 (d) shows the final triple charge measurement. Using this combination we were able to obtain a resolution of approximately 2% for Z=14 particles.

Events that fell into any of the hexagonal gates from Z=8 to Z=14 were selected as good events and the rest were discarded. Charges $Z \leq 7$ were unusable due to the trigger cut at Z=7.

2.2 Event Classification

The basic criteria for selecting EMD events is based on the assumption that the electromagnetic processes do not produce any activity at the target region. The projectile will essentially travel along its path without interacting, with the exception that it gains some additional energy by the absorption of a virtual photon. This excess energy may be enough to allow ejection of one or more nucleons from the nuclei. Nuclear collisions on the other hand are hard collisions that produce particles (eg. pions) at larger angles, and they can be detected by the target region detectors.

The background to the electromagnetic process can come from very soft nuclear

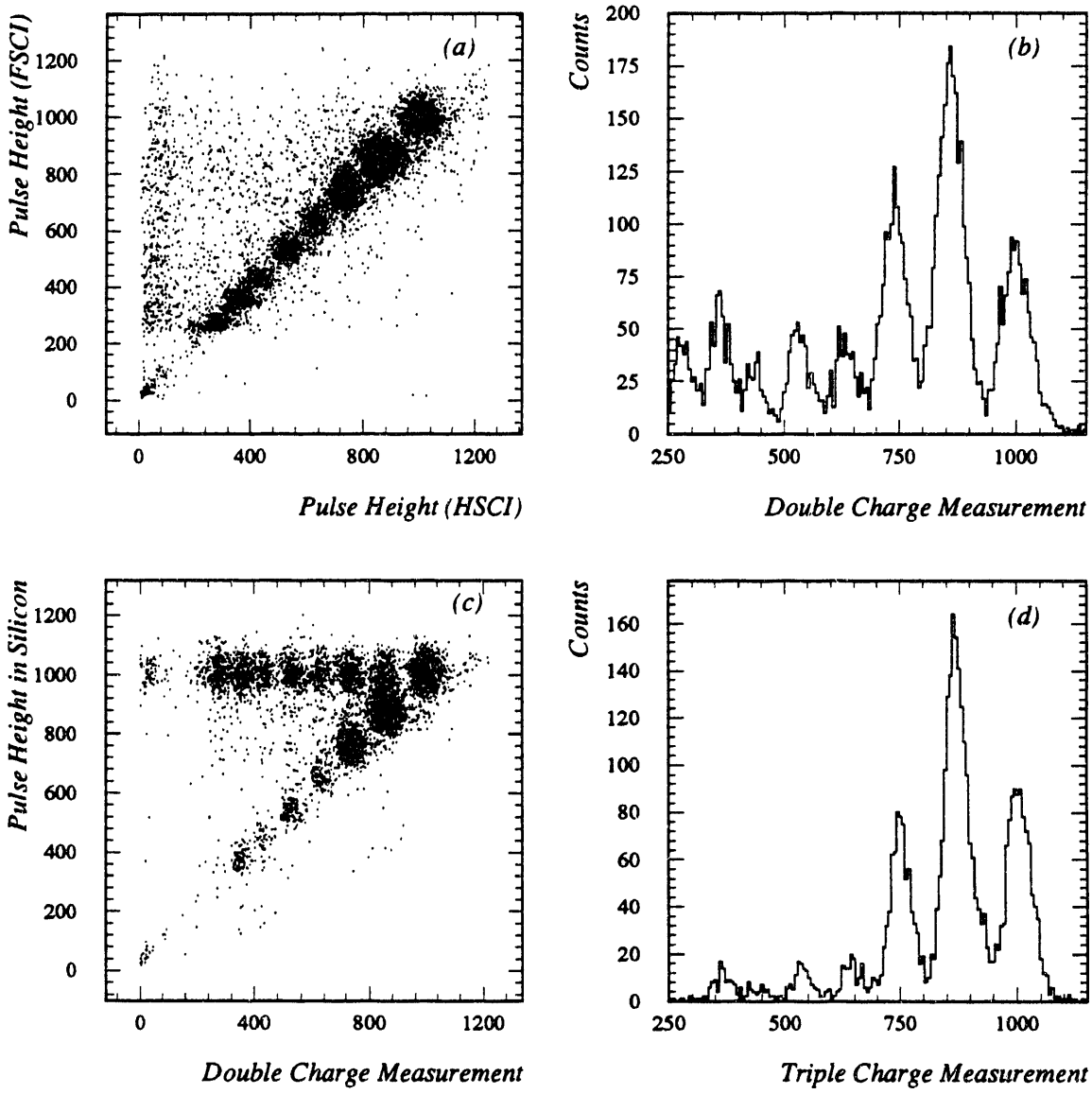

Figure 4.4: Triple charge measurement. (a) Pulse height in FSCI vs. pulse height in HSCI. (b) Double charge measurement by FSCI and HSCI. (c) Silicon downstream detector vs. double charge. (d) Triple charge measurement by combining all three measurements.

fragmentation which produce the same final state products as the electromagnetic processes and also have no activity in the target region. These processes cannot be distinguished from the EMD process on an event by event basis, but can be separated by studying the Z and A dependence of the dissociations. Selection criteria were developed to minimize the nuclear background, while keeping a high efficiency for EMD events.

The basic selection criteria was defined by studying the background as well as the target region activity produced by pure beam particles. The pure beam particles were identified by selecting the Z=14 particles that entered the experiment through the beam scintillator system and the upstream silicon detector system. Requirements were then imposed to select only the events which survive as ^{28}Si, by measuring the charge and the energy at the downstream end of the spectrometer. A pure electromagnetic interaction does not produce more activity than a pure beam particle that passes through a given target without any interaction.

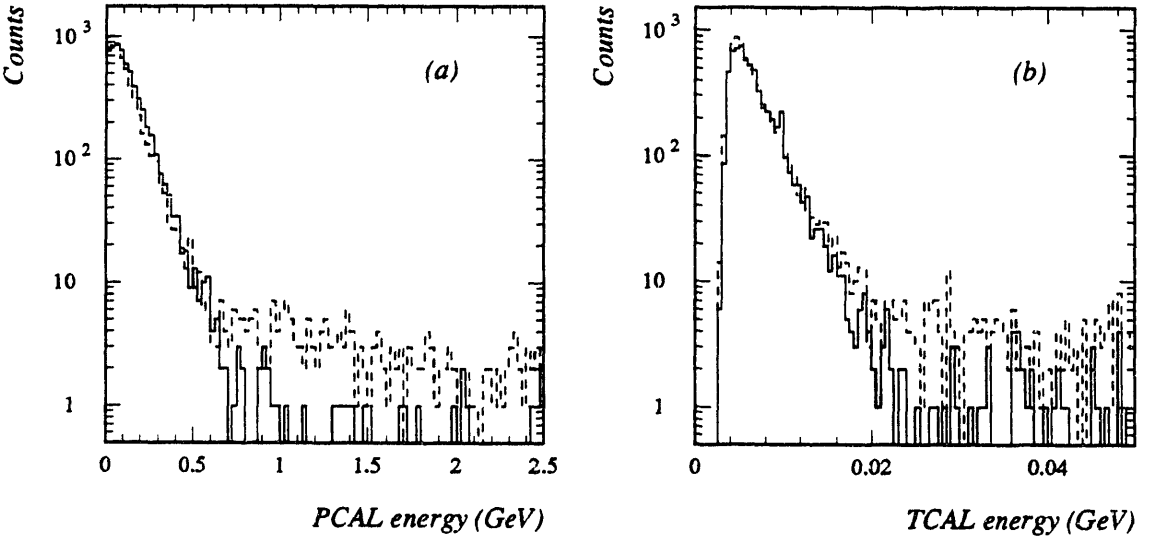

Figure 4.5: EMD event selection. (a) Energy measured in the PCAL for non-interacting beam events (solid line) and normal peripheral events (dashed line). (b) Same for TCAL.

Figure 4.5 (a) shows the total energy measured in a participant calorimeter for Si beams passing through a Pb target. The solid curve is for selected good beam tracks. The dashed curve is for normal peripheral triggers. Figure 4.5 (b) shows the maximum energy seen in any of the crystals in the side walls of the target calorimeter for the same type of events. Both of these spectra show a higher energy tail originating from non-peripheral interactions.

The response of each detector system was studied for selected good beam events and peripheral events by generating plots similar to those shown above. The cuts were imposed at each detector to reject $\leq$1% of the good beam events. The selected cuts are listed in Table 4.3.

Table 4.3: List of cuts used in EMD selection. The events which produce energy and multiplicity below the values listed here for each detector were taken as good peripheral events.

Detector System	Cut Description	Cut
Multiplicity Detector	Charge Multiplicity	25
Target Paddles	Charge Multiplicity	4
Target Calorimeter	Maximum energy in side walls	20 MeV
	Maximum energy in back wall	15 MeV
Participant Calorimeter	Maximum energy in EM section	200 MeV
	Maximum energy in HD section	200 MeV
	Total Energy	1 GeV
Magnet Scintillators	Charge Multiplicity	5
Pi-neut Calorimeters	Maximum tower energy	0.5 GeV
Neutron region scintillators	Charge Multiplicity	3

Good electromagnetic events are defined as events which do not produce an energy or a hit multiplicity above the cuts listed in Table 4.3. in any of the detectors. Events which produce any activity above these cuts in one or more of the detectors are taken as events originating from nuclear interactions. The additional information about the electromagnetic or nuclear origin was recorded in the secondary 8 mm tapes with the original data records to be used in further studies.

Table 4.4 shows the efficiency of the cuts for different targets when applied together on selected beam particles. The rejection could be due to the accidental δ rays, or the noise problems in the detector systems.

Table 4.4: Estimated efficiency in the offline selection procedure for selecting events produced by the electromagnetic interactions for various targets.

Target	Efficiency %
Pb	96.2 ± 0.5
Sn	95.7 ± 0.2
Cu	95.9 ± 0.5
Al	97.0 ± 0.4
C	-
MT	96.8 ± 0.6

No target dependence of the overall efficiency was observed and hence the same cuts were applied to all targets for the selection of electromagnetic interactions.

C Cross Sections for Simple Channels

The simplest analysis topic of the peripheral collisions is the cross section measurements. Among cross sections, a single proton (1p) or a single neutron (1n) emission cross sections are the simplest and they provide a unique way to estimate the efficiency of the selection procedure. In this section, a detailed description of the cross section estimates for these two channels are given.

1 Event Characterization

After extracting the events that originate from electromagnetic interactions, the next step is to identify simultaneously all the fragments leading to the final state in question. This was done by measuring the charge and the energy of the reaction fragments. The drift chambers were not used for the identification of 1p and 1n emission channels.

1.1 Charge Measurement

The charge of the heavy ion provides the information about the missing number of protons. For example, for 1p emissions our measurement should be the charge of ^{27}Al, which is Z=13 or for 1n emissions it should be the charge of ^{27}Si which is Z=14. Hence, a tight requirement on the charge of the heavy ion could remove most of the background for the channel in question.

The triple charge selection described in the earlier section gives us a very clean charge measurement for the heavy fragment. Figure 4.6 (a) shows the measured charge spectra at the downstream silicon detector for selected Z=14, Z=13 and Z=12 charge fragments with the triple charge selection. The plot demonstrates our ability to select portions of each charge species even in the overlapping regions. Although the downstream silicon detector measurement does not provide a clean charge separation by itself, this, combined with the vertical and horizontal scintillator hodoscope measurements gives an extremely good charge measurement.

In addition, the total charge in the upstream forward scintillators (upstream charge sum) was used to identify the protons deflecting into the Z/A=1 region. Figure 4.6 (b) shows the upstream charge sum for peripheral events. In this plot, peaks corresponding to one or two Z=1 particles are clearly visible. Only a loose cut at the lower edge was used since the charge spectrum has higher pulse heights due to the energy loss mechanisms in the scintillators (Landau shape) and the production of δ rays in the two drift chambers quite close to the upstream forward scintillators. The δ rays were mainly produced when the heavy ion tracks passed through the drift chambers. This effect was more prominent in the counters close to the beam line.

1.2 Energy Measurements

The energy in the proton and neutron calorimeters provide the additional information that is necessary to remove the background in these two channels. Figure 4.7 (a) is a

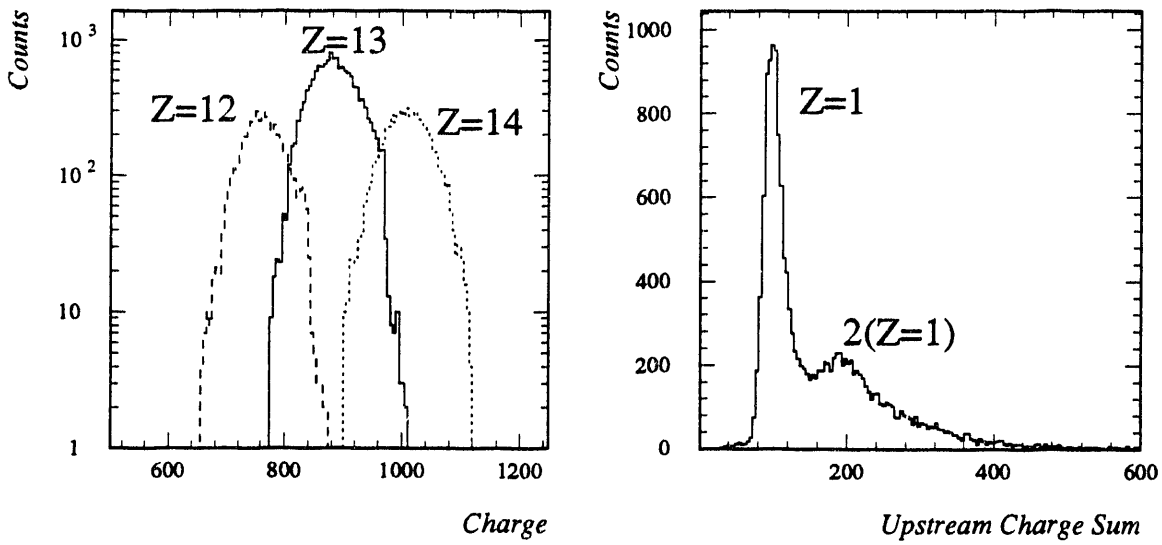

Figure 4.6: Charge selection. (a) Measured heavy ion charge for Z=14. Z=13 and Z=12 fragments. (b) The total charge measured in the upstream FSCI.

scatter plot of the raw energy in the proton calorimeters verses the raw energy in the neutron calorimeters for selected Z=13 and Z=14 particles. Three different clusters are visible in this plot. They are the protons and neutrons created by 1p+^{27}Al, 1n+^{27}Si and 1p+1n+^{26}Al reactions. It is clear from this plot that with extra cuts on the energy measurements we can select clean event samples for 1p and 1n emissions.

Figure 4.7 (b) shows the measured proton cluster energy for selected Z=13 candidates. A single cluster was selected as having energy between 4 and 22 GeV. A similar energy distribution was observed with neutrons for selected Z=14 candidates. Table 4.5 shows the cuts used to identify 1p and 1n emission channels.

Table 4.5: List of cuts used to select 1p and 1n events. These cuts were imposed on selected EMD event samples. The upstream charge sum was calibrated to place the minimum ionizing particles at 100 units.

Measurement	1p+^{27}Al	1n+^{27}Si
Heavy ion Charge	Z=13	Z=14
Proton Energy	4<E<22	E<4
Neutron Energy	E<4	4<E<22
Upstream Charge sum	Z_{sum}>25	-

1.3 P/Z from Scintillators

Although we do not need to measure P/Z of the heavy fragment to identify the 1p or 1n channels. the horizontal scintillator hodoscope provides confirmation of the purity

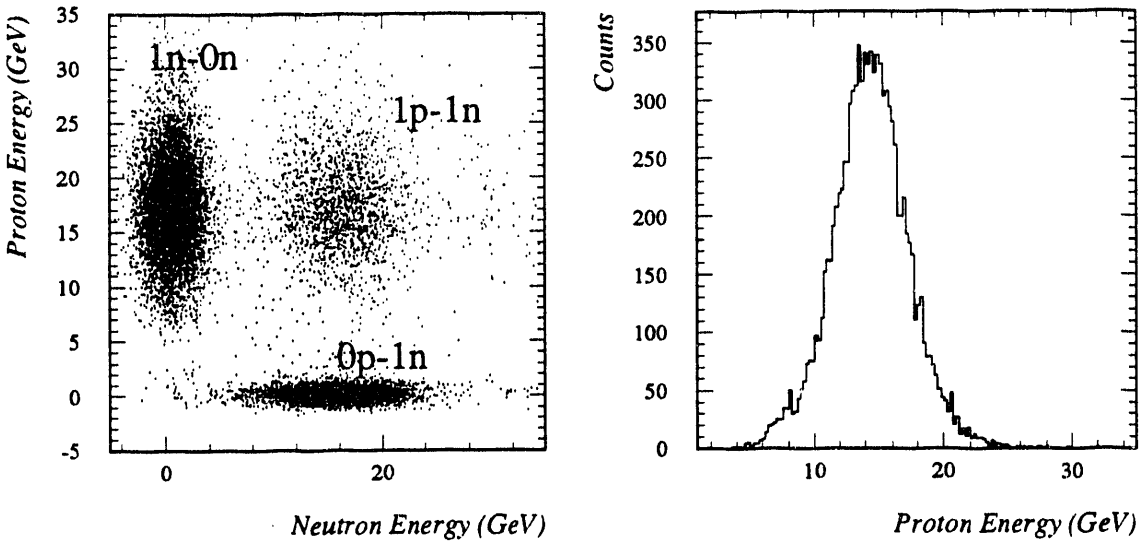

Figure 4.7: Energy selection. (a) Energy in the proton calorimeter vs. the neutron calorimeter for Z=13 and Z=14 events. (b) Proton calorimeter energy for selected 1p events with Z=13 and cut on neutron energy.

of the samples. The position of the heavy fragment in the horizontal scintillator hodoscope corresponds to the P/Z of the heavy fragment. Figure 4.8 shows the position distributions obtained for selected 1p, 1n, 1p1n and 2p channels. The position resolution of the horizontal scintillator hodoscope is about 2 cm. The distributions are corrected for the beam angle variations measured by the beam vertex detector. No cuts were applied based on this measurement due to the large variations in the position measurements arising from the gain drifts in the phototubes and the many overlaps between different channels. However, the P/Z estimations obtained through drift chamber track reconstruction turn out to be an extremely useful tool in selecting more complex channels. Such measurements are discussed later in the thesis.

2 Cross Section estimates

2.1 Efficiencies

Before estimating the absolute cross sections there are a number of corrections that need to be extracted from an unbiased data sample. These corrections arise from inefficiencies introduced by the selection procedures. The correction factors are evaluated carefully using pre-trigger and beam trigger data in such a way that the same efficiency is not counted twice.

The methods used to estimate the efficiencies are described below. A list of estimated efficiency factors obtained by this method is given in Table 4.6.

- *Upstream Interactions* – The upstream interaction efficiency was calculated by estimating the number of beam particles that were selected by the beam trigger

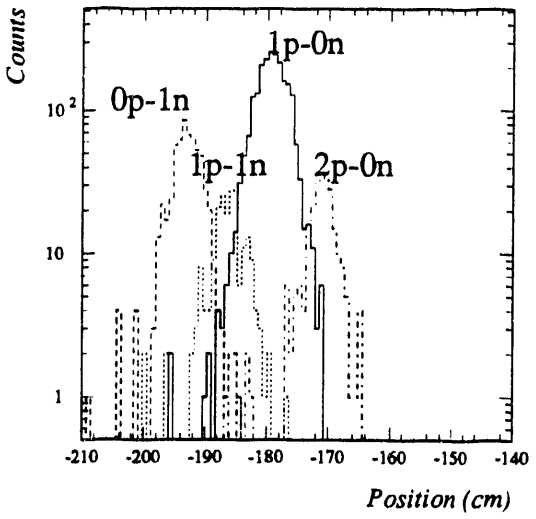

Figure 4.8: Measured position of the heavy ion fragments at the downstream horizontal counter for selected channels.

but were rejected by the cuts used in the beam scintillators and the upstream silicon detector. This represents the efficiency in the trigger of detecting good beam particles. The contribution of the time after previous beam cut at 2.5 μsec was not included in this but was calculated as a separate efficiency.

- *Downstream interactions* – The downstream interaction efficiency was calculated by selecting a sample of known Z, defined by the downstream silicon detector and the upstream proton calorimeters using low level triggers (beam triggers or pre-triggers). The probability of detecting the selected isotope inside the gates used in the triple charge measurement directly provides the downstream interaction efficiency. As a result, the cracks between individual scintillators, inefficiencies in selected gates etc are also included in the estimation. This efficiency in principle has a Z dependence.

- *Veto wall* – The veto wall efficiencies were estimated with a sample of Z which was already identified as good events with no downstream interactions, using the pre-trigger tapes. The probability of the survival of these events with and without the veto wall selection gives us the efficiency of this cut. It was assumed that this cut does not depend on the Z of the isotope or on the type of target, although there could be a small dependence due to the production of δ rays.

- *Proton and Neutron Clusters* – The clustering algorithms fail to predict the correct energy for nucleons going through the cracks or gaps in calorimeter modules. In addition, shower fluctuations could lead to some inefficiency due to a low energy deposition. The efficiency arising from clustering algorithms was estimated by selecting a known sample of 1p and 1n events in the pre-trigger

sample which produces energy outside the applied cuts in the analysis for these calorimeters.

- *Upstream Charge Sum* – The efficiency due to the upstream charge sum was calculated by selecting a good sample of 1p events without using the upstream charge sum, but using all other available detectors. The inefficiency of this cut arises due to the gaps between scintillation plates.

- *Downstream silicon detector* – The efficiency in the downstream silicon detector was calculated by selecting Z=14 particles from the upstream silicon detector and the downstream forward scintillator measurement. It was necessary to select the Z of the fragment at the downstream end of the spectrometer since a clean sample with a known Z was needed to estimate this efficiency. It was assumed that all gates defined to select different charges have the same efficiency.

- *Offline veto* – The offline veto efficiency was taken as the average of the efficiencies calculated for each target, with and without the offline vetos, using selected good beam tracks. Although cuts on each detector measurement were limited to reject only upto 1% of the good beam particles, when applied together, they produce a non negligible effect. The individual efficiencies for each target are listed in Table 4. Although a target dependence in this efficiency was anticipated, we have not observed one.

- *Time after previous beam* – The efficiency due to time after previous beam cut was evaluated by estimating the number of surviving good beam particles with and without the 2.5 μsec cut. The rejection due to this cut showed a large variation among the runs and hence was calculated separately for each run. Only the average value is shown in Table 6. It was found that the pileup effect for the latter part of the data tapes was low and therefore a somewhat lower (2.2 μsec) cut was applied for these data.

- *On-line veto detectors* – To evaluate the on-line veto efficiency, the same analysis was applied to the events taken with veto and the events taken without the veto requirements. The ratio of the yields of these two samples, with proper normalization for the trigger downscaling, provided the required efficiency. To reduce the fluctuation due to low statistics, for each run, the ratio was weighted with the average formed separately for each trigger by the trigger scaler counts. It was found that this efficiency is strongly target dependent.

Due to their run dependence,the efficiencies for the time after previous beam and on-line veto detectors were estimated on a run by run basis. Only the average is shown in Table 4.6. The large inefficiency in the neutron cluster energy selection compared to the proton cluster energy selection is probably due to the cracks in the neutron calorimeters located in the zero degree line. The pre-trigger efficiencies for 1p and

Table 4.6: List of efficiencies for the cuts used to select 1p and 1n events. These efficiency factors can be considered as independent of each other.

Selection Criteria	Efficiency %
Upstream interactions	97.8 ± 0.2
Downstream interactions	70.6 ± 1.9
Veto wall selection	87.5 ± 1.8
Proton clusters	95.8 ± 1.0
Neutron clusters	90.0 ± 2.0
Upstream charge sum	95.1 ± 0.6
Downstream silicon detector	98.0 ± 0.3
Offline veto detectors	96.3 ± 0.5
Time after previous beam	86.2 ± 2.2
On-line veto detectors	76.9 ± 1.4

1n are found to be 100%. We estimate the total efficiency [1] for 1p and 1n detection as 34%. This number is obtained by taking the product of all the relevant efficiency factors for each trigger type listed in the Table 4.6, assuming that the efficiency factors are independent from each other.

2.2 Cross Sections

The following formula was used to calculate the exclusive cross sections:

$$\sigma = \left(\frac{N}{B}\right)\left[\frac{MD}{N_A W_t}\right]\left(\frac{1}{f}\right) \tag{4.1}$$

where M is the atomic weight of the target material, D is the downscaling factor, N_A is the Avagadro number, W_t is the target thickness in g/cm^2, f is the efficiency factor, B is the total number of beam particles and N is the observed number of events for any given channel. A list of the targets used, and their properties are listed in Table 4.7.

The total number of beam particles extracted from the beam scalers were corrected for the loss of events due to after protection. This was done by estimating the number of beam particles that were rejected, by using the recorded number of pre-triggers rejected by the first level trigger. This has approximately 10% effect on the cross section estimates and cannot be neglected.

[1] Note that the total efficiency estimated for 1p events is slightly lower than the values given in Ref [31]. This is due to the fact that the efficiency of the offline veto detectors were not accounted for in the reference. Therefore, the cross sections and the other parameters extracted from the 1p data given in this thesis are slightly different to the values given in Ref [31].

Table 4.7: List of targets and their properties.

Target	Atomic weight M	Charge Z	Thickness W_t (g/cm^2)
Pb	208	82	4.359
Sn	120	50	3.253
Cu	64	29	2.239
AL	27	13	1.300
C	12	6	0.596

The observed number of counts were corrected for the interactions due to air, helium, or any other material in the path, by normalizing the counts observed for the empty target frame to the total number of beam particles used. The empty contribution for Pb and C targets are 5% and 50% respectively. In addition, part of the data obtained from 1n triggers were corrected for a trigger problem which affected 50% of the total 1n sample. This was caused by a failure of a signal cable used in the 1n trigger to detect neutrons in one U/Cu calorimeter module. The estimated correction factor for this is about 30% on the cross section values obtained by the 1n trigger.

Since the downscaling factor depends on the type of trigger used, the cross sections were calculated separately for each trigger. The evaluated cross sections for 1p and 1n channels are listed in Table 4.8. The errors include the statistical and the observed run to run variations. We estimate an additional systematic uncertainty of the total cross section values of approximately 5%. For comparison, earlier measurements of cross sections with the E814 apparatus [31] are listed. A good overall agreement is seen although the two sets of data are quite different.

Table 4.8: Measured cross sections for 1p and 1n emission by EMD. For comparison, earlier cross section measurements through our experiment are also listed.

Target	1p cross sections (mb)		1n cross sections (mb)	
	This work	Ref [31]	This work	Ref [31]
Pb	676.4±33.5	672.2±24.8	241.0±13.1	268.5±12.0
Sn	274.0±14.6	290.6±13.8	100.0± 4.5	103.2± 7.1
Cu	111.0± 2.2		40.4± 4.8	
Al	31.6± 3.6	34.2± 4.7	13.1± 1.8	11.3± 2.3
C	13.3± 0.7		6.3± 0.4	

CHAPTER 5

Reconstruction of Events

This chapter explains the methods developed to reconstruct the simple decay channels that have two or three particles in the final state. A complete event reconstruction was carried out by constructing the track segments at each detector and successively combining them with geometrical and kinematical constraint fits which exploit the physics behind the reaction under investigation. The methods discussed here are quite general in nature and can easily be extended to study other reactions.

A Track Reconstruction

The tracks in the forward spectrometer are reconstructed by performing a crude selection, followed by a detailed pattern recognition. The information from the detectors which measure the position of the particles upstream and downstream of the magnet are combined to obtain track parameters such as the position and the angle along the path of the particles as well as the magnetic rigidity P/Z.

1 Preliminary Selection

The preliminary extraction of tracking information was carried out by selecting possible hit candidates that are generated by the passing tracks at the beam vertex detector, the pad chamber DC1, the drift chambers DC2 and DC3, the forward scintillators and the U/Cu calorimeters. The detailed analysis described in chapter 3 was performed to eliminate noise and to construct the possible hit candidates at each detector plane.

For peripheral events, it is necessary to identify tracks that belong to the heavy ions and the other light fragments simultaneously. The identification of the hits which belong to the heavy ions is straightforward since, from all the possible hit candidates, these produce the highest charge or energy. This is not the case for the drift sections of DC2 and DC3 since the TDC does not carry information about the charge or the energy of the passing tracks. However, the pad sections located at the end of each chamber measure the charge of the passing tracks and these measurements can be used to initiate the selection procedure in the drift chambers.

The pattern recognition in the drift chambers was carried out by establishing "roads" in the drift and pad sections to identify the track segments within each chamber. These roads are defined to an accuracy of the width of the pads, which varies over the pad plane. The possible variation in the angle of the tracks for peripheral events crossing each chamber at different locations was also incorporated in establishing roads. No attempt was made to remove the left-right ambiguity in the x locations predicted by the TDC hits and both possibilities were kept at this stage of the analysis. The roads which contained hits in 3 or more of the 6 planes were taken as the possible hits generated by the real tracks.

The connection between the roads in DC2 and DC3, and the hit clusters in the forward scintillators generated by the same particle traversing the detectors downstream to the magnet was obtained by performing a linear least squares fit for these three measurement (both in the x and the y directions). The agreement between the calorimeter measurements and the predicted measurements (using the results of the fit and extrapolating them to the plane of the calorimeters) was used to select the best candidates to form the links between the track segments that form the tracks downstream of the magnet.

The x position in the pad chamber DC1 belonging to any track can be predicted by using the information from the beam vertex detector and the downstream crude track reconstruction combined with a simple magnet model. In this model the two magnets are replaced by two bending planes as shown in Figure 5.1. Here, x_o represents the position of the beam track at the target plane. This can be extracted from the beam vertex detector measurements. The outgoing track angle at the target plane which is represented by θ_o is very close in measurement to the incoming beam angle for the heavy ions but not for the light particles. The angle and the position of the downstream track at the plane of DC2 are represented by $\acute{\theta}$ and $\acute{x}$ respectively and the bending angles at each magnet are represented by θ_1 and θ_2 respectively.

The x position at DC1 is related to the upstream and downstream information by the formula,

$$x_{DC1} = x_1 + (x_2 - x_1) \times \left[\frac{z_{DC1} - z_1}{z_2 - z_1}\right]$$

where x_1 and x_2 are given by:

$$x_1 = x_o + z_1\theta_o$$

$$x_2 = \acute{x} - (\acute{z} - z_2)\acute{\theta}$$

The upstream angle θ_o can be calculated by:

$$\theta_o = \left[\frac{3(\acute{x} - x_o) - \acute{\theta}(2z_2 + z_1 - 3\acute{z})}{2z_2 + z_1}\right]$$

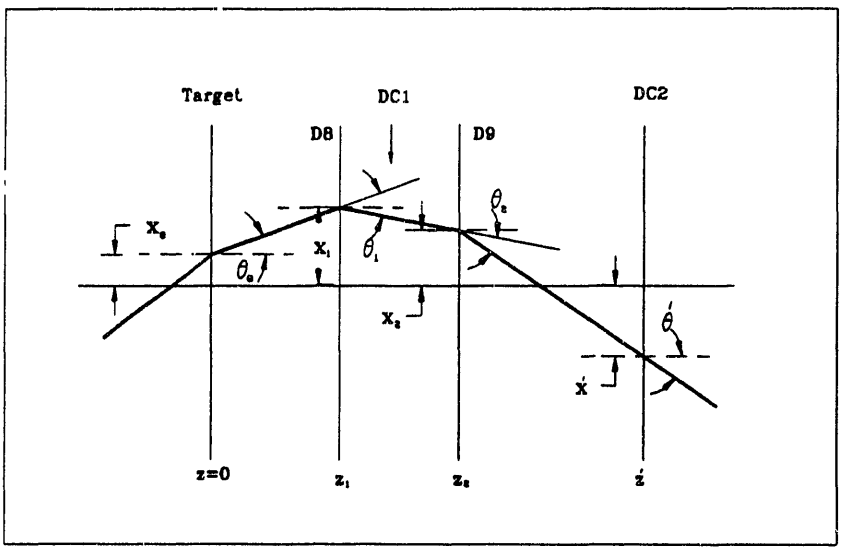

Figure 5.1: Two bend magnet model used in the preliminary analysis.

where we have taken the value of the ratio θ_1/θ_2 to be 2.0 from the magnetic field settings and effective lengths. By substituting the known values for the locations of the measuring planes along the z direction (z_1, z_2, etc) we can estimate x_{DC1}. In addition, this method allows us to calculate a crude value for the magnetic rigidity P/Z by using the simple relationship;

$$\left(\frac{P}{Z}\right) = \frac{k}{(\acute{\theta} - \theta_o)}$$

where k is a constant found to be ≈ 1.85. The value of P/Z extracted by this method was used to solve various software problems at the early stages of the peripheral analysis.

Figures 5.2 (a) and (b) show the difference between the predicted and the measured x positions at DC1 for heavy ions and protons respectively. The plots indicate our ability to select hits in DC1 without using time consuming pattern recognition algorithms. For the y agreement, a direct extrapolation was used by assuming that the tracks pass $y = 0$ at the target plane. The hits in DC1 were identified by searching for the best candidate in the neighborhood of the predicted x and y positions.

All the possible hits in DC1, DC2, DC3 (both drift and pad sections), the forward scintillators and the calorimeters, along with the hits in the beam vertex detector were passed on to our pattern recognition program (GRIST) which was developed to perform full event reconstruction in the peripheral analysis.

2 Pattern Recognition in Drift Chambers

The most tedious pattern recognition in E814 tracking chambers involves reconstructing the tracks in the drift sections. This is complicated by the ambiguity in the posi-

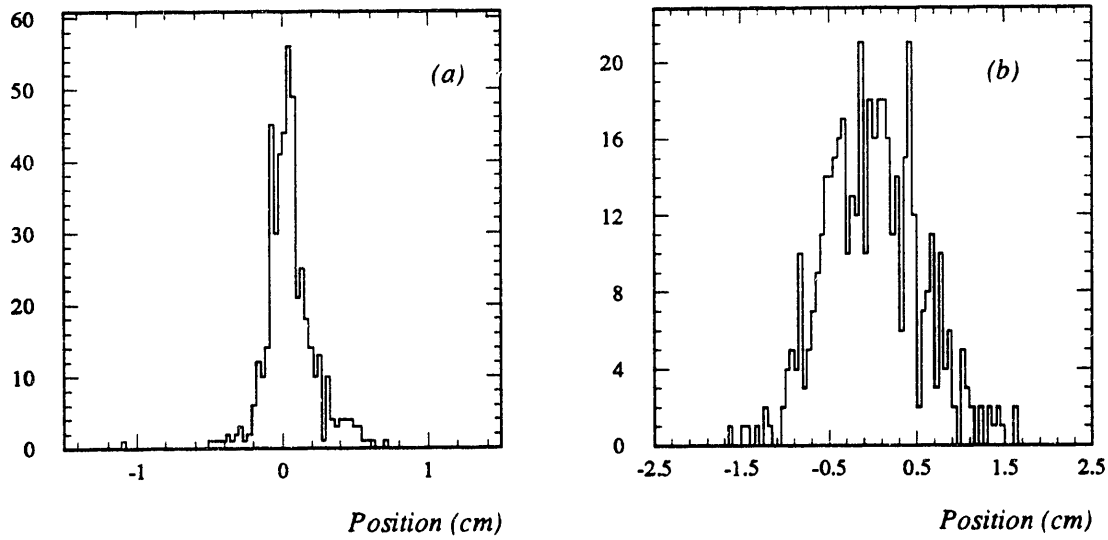

Figure 5.2: Accuracy of the DC1 hit selection. (a) Difference between the predicted and measured heavy ion positions. (b) Same for protons.

tions generated by the TDC hits which could be on either side of the anode wires, as well as the δ rays generated by the passing charge particles. For the heavy ion tracks, the rejection of the TDC hits created by the δ rays is the major problem.

It was found that the sum of the drift times of charge clusters drifting in opposite directions of neighboring anode wires provides a good selection criteria for the selection of true TDC hits originating from the passing tracks. Hits created by the δ rays do not produce the correct drift times that are produced by the good TDC hits which originate from the charge clouds. However, depending on the position of the tracks traversing between the neighboring planes which are shifted by half a cell relative to each other, the sum of the drift times varied by an amount that is proportional to the angle of the tracks. A correction was made to remove this effect in neighbor sums by estimating the angle of the tracks, using the pad locations reported in DC2 and DC3 by the preliminary selection procedures described earlier. Figures 5.3 (a) and (b) show the neighbor sums for heavy ions and protons passing through DC2 respectively. A FWHM of $\approx$ 30 and 60 ns were observed for DC2 and DC3 respectively.

By requiring that the sum of the drift times obtained from the neighboring anode wires fall within a window that corresponds to $\pm$ 1.0 mm in space, consistent hits within DC2 or DC3 were identified in the track reconstruction stage. Centroids were formed with the hits that satisfied this criteria and were observed in the odd-even planes. The location of the set of drift chamber hits which were most consistent with a straight line segment falling within the road was obtained using the Principle Component Analysis [56]. The left-right ambiguities are eliminated by the use of such centroids. After identifying the correct TDC hits, the centroids were discarded and the original TDC values were used in the track construction.

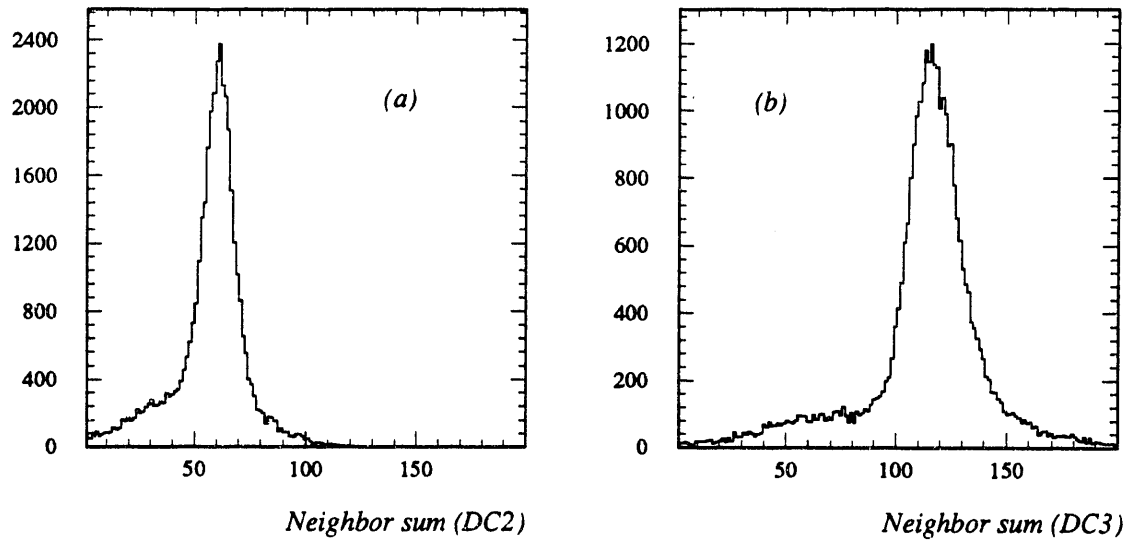

Figure 5.3: Measured sums of drift times in neighboring anode wires for protons. (a) DC2. (b) DC3.

The facility to obtain high level TDC hits [1] or so called second TDC hits, is incorporated mainly to help separate the hits generated by δ rays from the true charge clouds. Figure 5.4 (a) shows the second hit against the first hit measured for beam tracks passing through one plane of the chamber DC2. As expected, a majority of the events show a good correlation between these two measurements. But, an additional correlated band which is shifted by 40 ns or so from the main band was observed. Detailed studies showed that in some isolated cases, not one, but several of these could be observed even for individual wires. One explanation could be that the arriving charge clouds contained several peaks in the TDC distributions due to the distortion from δ rays and therefore the zero crossing discriminators were firing several times for the same charge cloud, with different time intervals. However, this did not complicate the analysis described in this thesis since the second hits were not used in the primary selection. Figure 5.4 (b) shows the same events after selecting the best events through our selection criteria. The second band is observed less frequently now, indicating that it consists mainly of hits distorted by the δ rays. To identify a set of good TDC hits, the initial pattern recognition was started with those hits which reported second hits.

For the charged particle tracks, the position information from the forward scintillators and the calorimeters was not used in the final track reconstruction stage. It was used only to guide the initial pattern recognition since the drift chambers provided a better resolution. However, to reconstruct neutral particles (neutrons), the calorimeter position and energy information were used since these were the only available information for these particles.

[1] see chapter 3, section 2.4

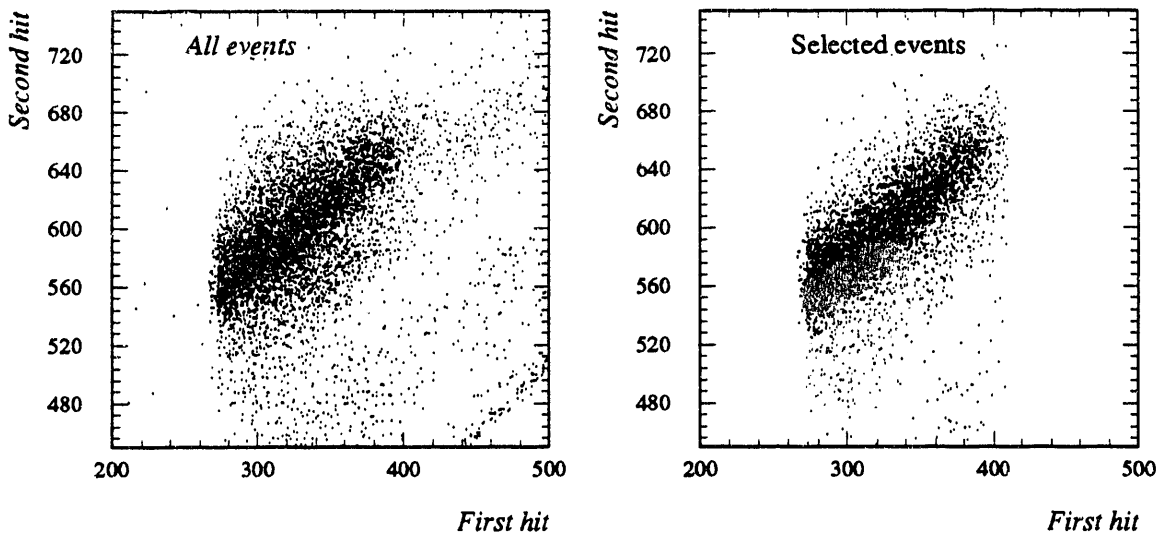

Figure 5.4: Second TDC hit vs. the first TDC hit. (a) All hits. (b) Selected hits.

3 Tracking Details

3.1 Detector Alignments

Using the hits identified in the previous step, a fit was performed on the drift time values measured in DC2 and DC3, the horizontal and vertical positions identified in DC1, and the vertical positions found in the cathode pad sections of DC2 and DC3. Because of the inaccuracy in the vertical measurements, the track is constrained to pass through y=0 at the target. The vertical distribution of the beam particles is approximately gaussian, centered at y=0 with FWHM $\approx$ 6 mm. Since the trajectory passes through the magnet, the value of the magnetic rigidity for the track is introduced as a variable in this fit, along with the horizontal and vertical slopes and the intercepts of the tracks at the position of the target.

It was found that the physical locations of the detectors measured by surveyors are not accurate enough to obtain an optimum resolution from these chambers. The following steps were carried out to align the detectors. The results obtained for the x alignments of the tracking detectors are listed in Table 5.1. A similar procedure was carried out to align the detectors in the y direction.

- By using the given survey measurements, the beam tracks (with no target in the target holder) were reconstructed and the magnetic rigidity P/Z was measured. This value was taken as the true P/Z of the beam tracks, assuming that the offsets in the survey measurements were random and therefore did not cause any systematic change in the reconstructed P/Z value.

- By using the measurements reported by the first plane of the beam vertex detector and the drift chamber DC3, the beam tracks were reconstructed with

Table 5.1: List of offset constants extracted by the alignment studies.

Detector description	z Position (cm)	x Offset (cm)	Resolution (mm)
DC1 pad plane x	398.573	-0.038	0.200
DC2 wire plane 1	687.073	-0.097	0.300
DC2 wire plane 2	687.708	-0.070	0.300
DC2 wire plane 3	688.343	-0.074	0.300
DC2 wire plane 4	688.978	-0.067	0.300
DC2 wire plane 5	689.613	-0.062	0.300
DC2 wire plane 6	690.248	-0.072	0.300
DC3 wire plane 1	1158.164	0.020	0.300
DC3 wire plane 2	1159.434	0.030	0.300
DC3 wire plane 3	1160.704	0.044	0.300
DC3 wire plane 4	1161.974	0.030	0.300
DC3 wire plane 5	1163.244	-0.005	0.300
DC3 wire plane 6	1164.514	0.045	0.300

the measured value of P/Z (extracted in the previous step) kept as a constant. The value of the shift in each detector plane (which was not used in the fit) was estimated and corrected.

- The previous step was repeated by using all the detectors other than DC3, and the offset constants were obtained for DC3. The position of the first plane of the vertex detector was assumed to be correct. This assumption did not produce any bias in the track reconstruction since all the detectors were aligned relative to the initial configuration.

3.2 Resolution in Drift Chambers

The tracking chambers were designed to detect minimum ionizing particles as well as heavy fragments. The study of peripheral interactions requires that the tracking chambers respond to both types of particles with high precision. Our pattern recognition methods indicate that the horizontal spatial resolution in each drift chamber plane for both type of tracks is ≈ 300 μm. although the heavy ion tends to produce more δ rays than the protons.

Figures 5.5 (a) and (b) show the residuals obtained for ^{27}Al tracks and proton tracks in DC2 respectively. The residuals were obtained by taking the difference between the fitted track and the measured positions. The plane to be tested was not used in the fit. In DC3 a position resolution similar to that for DC2 was achieved. Detailed studies indicate that individual wires show 100-250 μm single cell resolutions.

The reduced resolution for a single plane consisting of combining information from many wires could arise from the wire to wire offsets in these chambers.

An attempt was made to utilize the alignment method discussed above to determine individual wire offsets in the heavy ion region. Although the preliminary results were promising, the wire offset constants were not used in this analysis since this work is not yet completed and the methods involved are still under investigation.

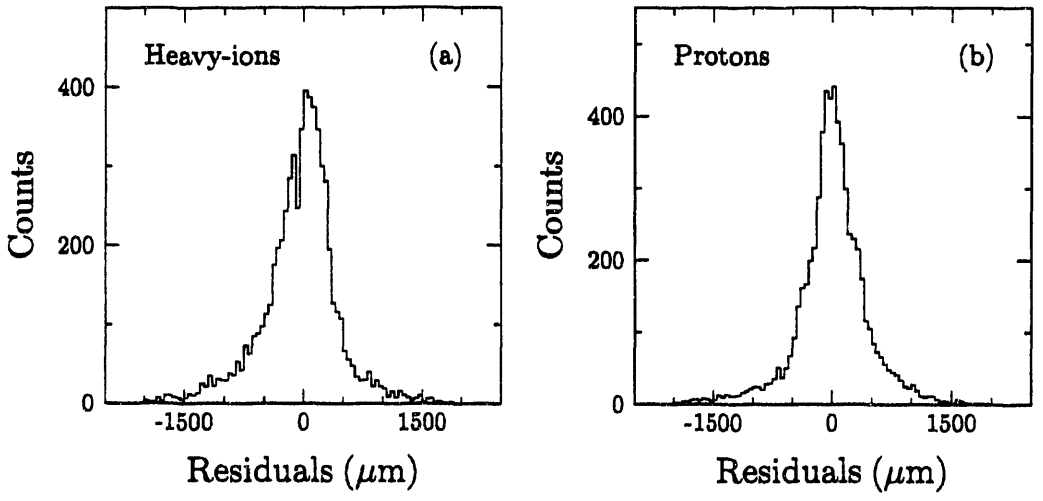

Figure 5.5: Resolution in the drift chamber DC2 (a) Heavy ions (b) Protons.

Figure 5.6 shows the measured P/Z for the beam tracks. A χ^2 cut was applied to remove the badly reconstructed tracks. A resolution of 1% was observed for the P/Z reconstruction. The major width in this distribution arises from multiple scattering in the material along the path of the track. An additional contribution of 0.25% comes from the momentum spread in extracting the ^{28}Si beam from the AGS. The value of the beam momentum extracted in this analysis was found to be 14.35±0.21 GeV/nucleon which is slightly lower than the beam momentum value of 14.6 GeV/nucleon advertised by the AGS.

B Reconstruction Studies

The improved estimates of the track variables as well as the physical quantities which we need to measure were extracted by using a reconstruction program which exploits geometrical and kinematical constraints. These constraints allow us to combine the tracking information in an optimal way to determine the parameters of interest.

1 Method of Reconstruction

The reconstruction program used in this analysis (GRIST) was originally developed at CERN during the late 1960's in an experiment which used optical spark chambers.

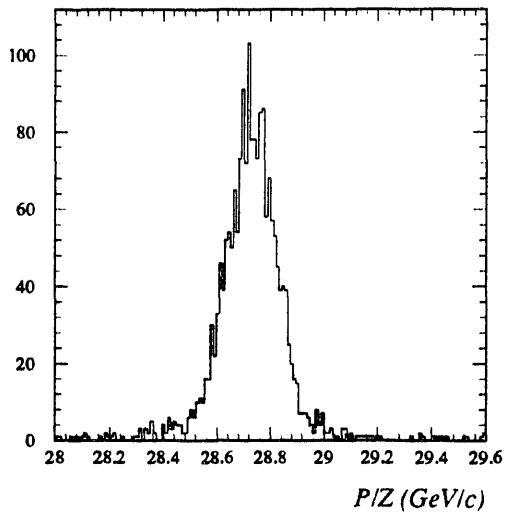

Figure 5.6: Reconstructed momentum distribution for beam particles.

This was later used in other experiments to study various reactions successfully and was modified by W.E Cleland to fit the peripheral events taken through the E814 apparatus. A brief summary of the evolution of this program is given in Table 5.2.

The method of reconstruction used in GRIST can be described as minimizing the χ^2 function with respect to a set of parameters a_j.

$$\chi^2(a_j) = \sum_i \frac{1}{\sigma_i^2} [\xi_i - U_i(a_j)]^2 \qquad (j = 1.....n)$$

where ξ_i and σ_i represent the observations (eg. Beam vertex measurements, measured TDC values of the tracks in the drift sections of DC2 and DC3, the position measurements of calorimeters ..etc) and their precisions respectively. The U_i are the calculated values of the expected observations and are a function of the set of parameters a_j. The a_j are chosen carefully so that they can describe the given hypothesis completely. In the final kinematic fit they are related to the center of mass decay angles and invariant masses of the assumed 2-body systems which describe the process. Initially, trial values for these parameters are assigned to shorten the iterative χ^2 minimization procedure.

If a_j^o are a set of trial values for the parameters a_j, by making the Taylor expansion about a_j^o, the χ^2 to be minimized by determining the corrections δa_j can be written as,

$$\chi^2(a_j) = \sum_i \frac{1}{\sigma_i^2} \left[\xi_i - U_i(a_j^o) - \sum_l \delta a_l \left(\frac{\partial U_i(a_j)}{\partial a_l} \right) \right]^2$$

Table 5.2: History of the event reconstruction code (GRIST) used in this analysis.

Years	Reaction	Ref	Features	Detectors
1965-1968	$\pi^- p \rightarrow \Lambda^o K^o \rightarrow p + \pi^-$ $p + c \rightarrow p + c$	[57]	No B field	Optical spark chambers
1968-1970	$\mu Z \rightarrow \mu\mu\mu Z$	[58]	Homogeneous B field	Optical spark chambers
1970-1973	$\Sigma + N \rightarrow \Sigma^* + N$	[59]	Inhomogeneous B field	Magnetostrictive spark chambers
1973-1976	$\Sigma^- \rightarrow \Lambda^o e\nu \rightarrow p\pi$	[60]	3 body decay (in B field)	Magnetostrictive spark chambers
1991-	$^{28}Si^* \rightarrow^{27} Al + p$ $\rightarrow^{27} Si + n$ $\rightarrow^{26} Mg + 2p$	[32]	Homogeneous B field	Drift chambers Scintillators Calorimeters etc

where $U_i(a_j^o)$ are the expected values of the observation for the set a_j^o. Thus, the χ^2 minimization can be carried out by solving.

$$\delta\vec{a} = A^{-1}\vec{\Delta}$$

in which

$$\Delta_k = \sum_i \frac{1}{\sigma_i^2}\left[\xi_i - U_i(a_j)\right]\frac{\partial U_i}{\partial a_k}$$

$$A_{lk} = \sum_i \frac{1}{\sigma_i^2}\left(\frac{\partial U_i}{\partial a_l}\frac{\partial U_i}{\partial a_k}\right)$$

where A^{-1} is the error matrix for the a_j and $\delta\vec{a}$ is the correction done to the initially selected a_j^o to obtain the minimum χ^2.

If the expected observations U_i have a linear dependence on the a_j, then the correct result can be obtained immediately. But since this is not the case for our data (and for most cases), an iterative procedure had to be used in which the convergence was dependent on the number of parameters involved and how well the initial parameters were chosen.

2 Application to Peripheral Events

2.1 Geometrical Constraint Fitting

The event reconstruction procedure was initiated by forming the individual track segments and by successively building up the vertices. This is essentially a purely

geometric fit, in which the angles of the tracks, the coordinates of the vertices, and the masses and the momentum of the particles are involved as parameters. In forming tracks in space, we need 5 parameters to specify each track (assuming that the tracks pass through magnets, since we would otherwise need only 4 parameters). They are, the x and y intercepts at the plane $z = 0$, the angles in the xz and the yz planes and the momentum of the particles associated with the given track. Geometrical constraints can be imposed according to a given hypothesis when forming the vertices for separate track segments.

Consider the example given in Figure 5.7 for the $^{28}Si^{*} \rightarrow 1p+^{27}Al$ system. The incoming beam track has only two parameters, the position and the angle at the target on the xz plane which are obtained from the beam vertex detector. The vertical information which is an unknown for our data was introduced as an additional parameter. For each outgoing track, only 3 parameters are needed since all three tracks have to form a vertex at the target. Therefore, we have a 9 parameter fit. If the three tracks were unconstrained, the pattern would be described by 2 parameters for the incoming track and 5 parameters for each of the outgoing tracks, for a total of 12 parameters. Thus, this fit has 3 geometrical constraints.

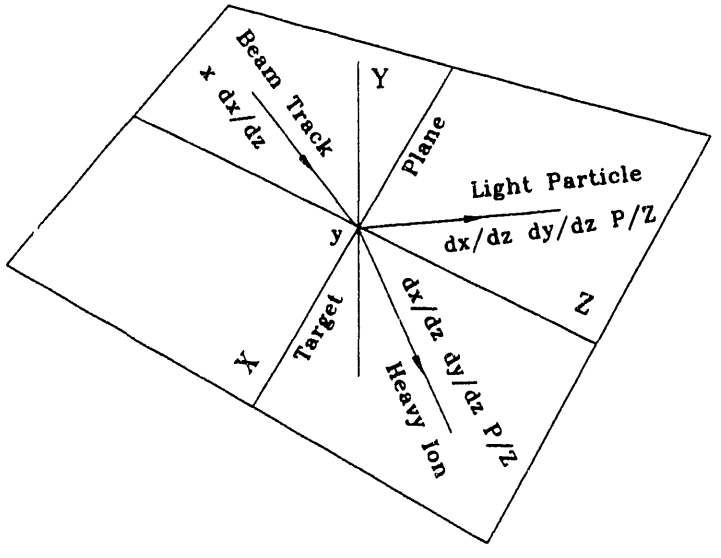

Figure 5.7: Selected geometrical parameters for the two body decay.

In the case of the $1n+^{27}Si$ system, only the measured position at the downstream calorimeters for the outgoing neutron was available to be used in the fit and hence, only a 1 geometrical constraint fit is formed.

2.2 Kinematically Constrained Fitting

The excitation energy of the projectile can be obtained by measuring the invariant mass of the system in question. Although the analysis can be carried out for systems

with several nucleons in the final state, the technique for a single proton emission channel will be described here. This can be generalized quite easily to many nucleons in the final state.

Consider the case where a ^{28}Si projectile absorbs a virtual photon from the coulomb field of the target nucleus when passing through the target. The excited ^{28}Si which has an excess energy that corresponds to the energy of the virtual photon (ω), decays into ^{27}Al and a proton. The ^{27}Al could be in its ground state or any of the excited states (ϵ_i) which will decay by emitting one or more γ rays.

The invariant mass of the final state system can be written as

$$M_{inv} = M_o + \omega - \epsilon_i = M_1 + M_2 + \epsilon^* = \left|\overline{P}_1 + \overline{P}_2\right|$$

where M_o, M_1 and M_2 are the reset masses of the ^{28}Si, ^{27}Al and 1p respectively, and $\overline{P}_1$ and $\overline{P}_2$ are the 4 momentum vectors of the ^{27}Al and the 1p respectively. Thus, the excitation energy of the final state 1p+^{27}Al system is,

$$\epsilon^* = Q + \omega - \epsilon_i$$

where $Q = M_o - (M_1 + M_2)$ is the Q value of the reaction. For this system with two particles in the final state,

$$\left|\overline{P}_1 + \overline{P}_2\right|^2 = M_1^2 + M_2^2 + 2\sqrt{P_1^2 + M_1^2}\sqrt{P_2^2 + M_2^2} - 2P_1P_2\cos(\theta)$$

where θ is the angle between the two momentum vectors. By measuring the momentum P_1 and P_2 and the opening angle θ, one can calculate the invariant mass and hence the final state energy ϵ^*.

The implementation of the kinematics in the data analysis is done by performing a kinematically constrained fit, the construction of which follows the same outline discussed earlier. In this fit, it is assumed that the decaying Si nucleus has the same velocity as the beam track, but that the invariant mass is increased by the final state energy which is introduced as a variable in the fit. Two center of mass decay angles (θ^* and ϕ^*) are also introduced as variables, along with the horizontal and vertical slopes and intercepts of the incoming track. In this analysis, θ^* is defined as the polar angle of the ^{27}Al momentum vector with respect to the beam momentum vector in the rest frame of the projectile (because of our assumption that the velocity of the projectile is unchanged in the EMD process, this is also the rest frame of the excited state), and ϕ^* is the azimuthal angle of the decay plane about the beam momentum vector, referred to the horizontal plane. The masses of the final state particles were obtained from reference [61].

The kinematic fit imposes two additional constraints beyond those required by the geometric fit for the 1p+^{27}Al system since the total number of parameters needed to described the reaction kinematics is only 7. The additional constraints can be viewed as imposing conservation for the x and z components of momentum.

This fitting technique was found to be very useful in reconstructing the $1n+^{27}Si$ system in which the measurement of the momentum of the neutron is poor, but the position is accurately determined ($\approx$ 2cm). If the energy measurement is counted as a measurement (it carries very little weight due to its large error) in the fit, we obtain the same number of additional constraints for the kinematic fit of the $1n+^{27}Si$ system, as in the $1p+^{27}Al$ system.

2.3 Optimal Track Fitting

The optimal track fitting is a method which attempts to find the closest fit for a given set of points obtained under the change in the track direction due to multiple scattering along the path length. Conventional fitting operations that involve extracting track parameters usually neglect the effects due to multiple scattering or, degrade the errors in the measuring points to account for the scattering. Both of these procedures do not exploit the information from the detectors effectively.

The technique used in this analysis is the method described by Lutz [62], in which the "observed" value of the scattering angle is zero and the error in the observation is the calculated rms value of the scattering angle projected onto a plane. Since each parameter is accompanied by an observation, this method introduces no change in the number of degrees of freedom of the fit.

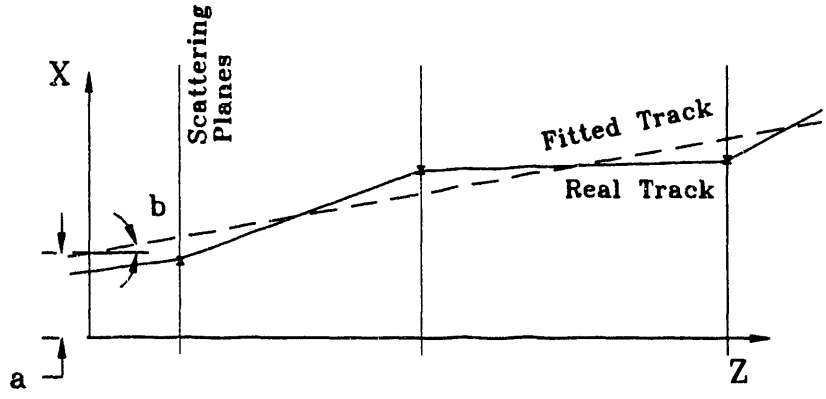

Figure 5.8: Effect of multiple scattering.

For simplicity, let us consider a region in two dimensions as shown in Figure 5.8. The multiple scattering along the trajectory can be replaced by a set of scattering planes which does not necessarily coincide with the measurement planes. The measured coordinates ξ_i can be fitted by a kinked trajectory whose position U_i in the measuring plane is parametrized by,

$$U_i = a + bz_i + \sum_J a_J(z_i - z_J)\Theta_J$$

where a and b are the position and the slope of the incoming track. α_J is the kink in the scattering plane J and the parameter Θ_J is introduced to restrict scatters ahead of the measuring planes where

$$\Theta_J = \begin{cases} 1 & \text{for } z \geq 0 \\ 0 & \text{for } z < 0 \end{cases}$$

The χ^2 to be minimized in this situation by can be written as.

$$\chi^2 = \sum_i \frac{(\xi_i - \zeta_i)^2}{\sigma_i^2} + \sum_J \frac{(\beta_J - \alpha_J)^2}{\sigma_J^2}$$

where σ_i is the rms measuring error of plane i and σ_J is the rms of the scattering angle β_J in the scattering plane J. It should be noted that knowing the value of β_J (in this case zero). compensates the additional parameters and thus keeps the number of degrees of freedom the same as that mentioned above.

In this analysis we introduce parameters to account for the multiple scattering in the horizontal plane for both the proton and the heavy ion tracks in the three regions where significant amounts of material are concentrated: namely the target. DC1 and DC2. It should be mentioned here that the energy loss resulting from the tracks passing through the target is also corrected.

3 Results

3.1 Efficiencies

Approximately 75% of the 1p events that were selected from the cross section analysis were reconstructed successfully. The major loss arises from demanding that there is exactly one hit in each counter of the beam vertex detector. Due to dead or noisy strips in the detector this criterion results in a loss of 15% of the events. By this. certain values of the beam angle and position are excluded. By failing to locate a sufficient number of hits in either DC2 or DC3 within the roads established in the pad sections of these chambers. 5% of the events are lost. (Due to the proximity of DC1 to the heavy ion track. there is a loss of the proton hit in 20% of the cases. but this does not affect the reconstruction of the event). Finally. due to either the geometric or kinematic fit failing to converge. 5% of the events are lost in the reconstruction stage. The remaining losses are quite small and it is obvious that they are not related to any particular event topology. The distributions of geometrical and kinematic quantities closely resemble those obtained in the simulation (described in the next section). Therefore it is assumed that any biases due to reconstruction inefficiencies are negligible.

3.2 Tests by Monte-Carlo Methods

The outcome of the pattern recognition methods and event reconstruction procedures depends heavily on the accuracy of the software carrying out the tasks discussed in the previous sections. The reliability of the software was tested by simulating the positions of the tracks for known kinematic conditions, in all the detection planes of the experimental apparatus, and by reconstructing them with the same code used for the real data. The actual experimental situations are represented as closely as possible by the simulation code. The measured uncertainties of the detectors and the effects that arise from multiple scattering in air and other materials (including the target and the material used in constructing various detectors) in the path of the tracks smear the track locations at each detector plane.

The excitation energy of the projectile for the $1p+^{27}Al$ and the $1n+^{27}Si$ decay channels were incorporated by convoluting the excitation energy observed in photo-absorption studies taken from the references [12, 13, 14], with the corresponding virtual photon spectrum. For other decay channels, the excitation energy distributions of Gaussian forms were used since the detailed comparison of low energy data with full event reconstructions were made for only these two channels in this thesis. In addition, to study the $1n+^{27}Si$ channel, the response of the neutron calorimeter energy distribution was built into the simulation since the energy measurements of the neutron calorimeters play an essential role for this channel.

The simulation also enables the study of the contributions from the various factors that affect the resolution of the reconstructed quantities. These arise from the position distortions caused by the detector resolution and by multiple scattering which is not accounted for by the optimum track fitting method. The real uncertainty in the recontruction was obtained by performing tests with the simulation of various reconstructed parameters. The results of these studies for $1p+^{27}Al$ and $1n+^{27}Si$ are shown in Tables 5.3 and 5.4 respectively.

Table 5.3: Reconstruction resolution for 1p events.

Source of Uncertainty $^{28}Si \rightarrow 1p+^{27}Al$	σ_M (MeV)	σ_{θ^*} (Degrees)	σ_{ϕ^*} (Degrees)
Detector resolution	0.5	1.0	2.5
Multiple scattering with no target	0.2	0.5	0.8
Total for Al target	0.6	1.3	3.2
Total for Cu target	0.7	1.6	4.0
Total for Sn target	1.0	2.1	5.0
Total for Pb target	1.1	2.6	6.0

An estimate of the systematic errors in the final state energy scale that arise from the uncertainty in the beam momentum, the field strength and the effective length

Table 5.4: Reconstruction resolution for 1n events.

Source of Uncertainty $^{28}Si \rightarrow 1n + ^{27}Si$	σ_M (MeV)	σ_{θ^*} (Degrees)	σ_{ϕ^*} (Degrees)
Detector resolution	1.5	19.5	3.9
Multiple scattering with no target	1.1	7.6	0.3
Total for Al target	2.2	21.6	3.9
Total for Cu target	2.0	27.9	1.0
Total for Sn target	1.9	27.7	4.1
Total for Pb target	1.9	28.0	4.2

of the spectrometer magnets, and the detector alignments, is also obtained from the simulation code. The estimated systematic error was less that 0.5 MeV.

CHAPTER 6

Analysis of Complex Channels

The results of the analysis of the peripheral data are described here. We have evaluated cross sections for a number of peripheral channels including those with α and d in the final state. In addition, we have measured excitation energy distributions for 1p+^{27}Al and 1n+^{27}Si through kinematic reconstruction. The possibilities of multi photon excitations and the effect on electromagnetic excitations by soft nuclear interactions are also investigated.

A Cross Section Measurements

In chapter 4, a discussion of the method used to extract cross sections for two of the simplest channels was given. The cross section analysis for exclusive channels with several nucleons in the final state is difficult if we require identification of each final state particle. Although the heavy ion charge selection through a triple charge measurement works very well for these channels, the efficiency of track reconstruction decreases with increasing multiplicity and the assignment of energy to overlapping hits in the calorimeter is very difficult. We therefore searched for a superior method to identify the channels.

1 P/Z by Drift Chambers

The P/Z of the heavy fragment will change by roughly 4% for the removal of each nucleon. The studies with drift chambers showed that the heavy fragment P/Z can be reconstructed with ~1% resolution. Since we can select a heavy ion charge with 2% resolution, this extra measurement helps to overcome the difficulties in identifying different isotopes.

Figure 6.1 (a) shows the measured magnetic rigidity (P/Z) for the heavy ion fragments with selected Z=13. The well resolved peaks in the plot correspond to different isotopes. They are 1p+^{27}Al, 1p+1n+^{26}Al and 1p+2n+^{25}Al. Figure 6.1 (b) shows the measured charge versus P/Z for heavy ion fragments. Each cluster of hits corresponds to a different peripheral channel. It should be mentioned here that we require the aid of calorimeters and other available detectors to separate the channels with a heavy ion of same P/Z but with different final states (such as 3p+2n+^{23}Na

and 1p+1α+^{23}Na). But for most of the channels we only need to apply very loose cuts in the energy measurements of the calorimeters.

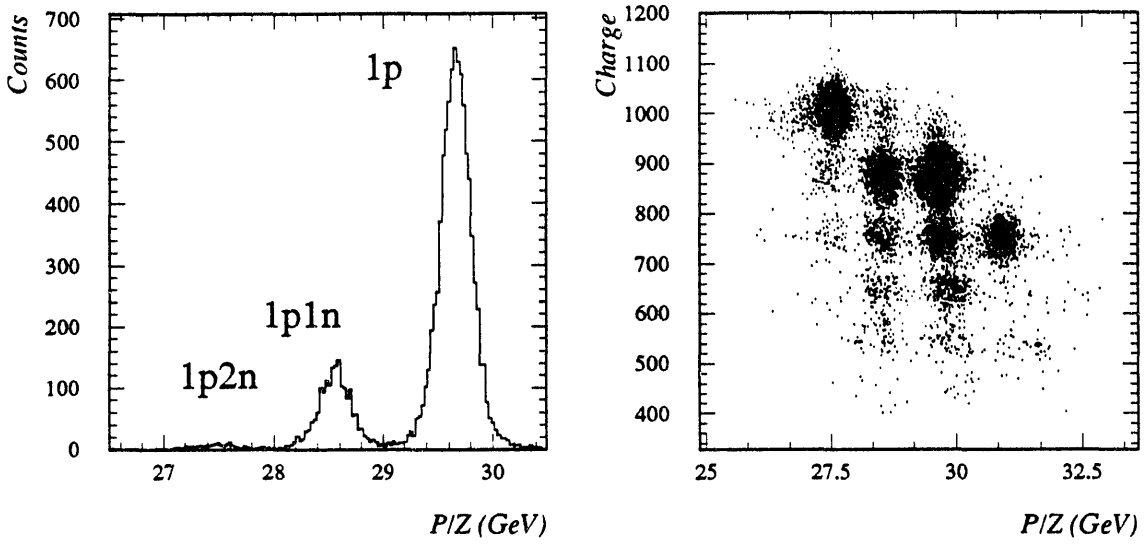

Figure 6.1: P/Z reconstruction. (a) Selected Z=13 events. (b) Charge vs. P/Z for different decay channels.

The major inefficiency for heavy ion track reconstruction arises from the beam vertex detector measurements. One plane of the beam vertex fails to report the hit location of the passing beam tracks for roughly 10-15% of the events. Therefore it is not possible to calculate the incoming beam angle for these events. However, it was found that the beam converging point was more or less concentrated in an ~1mm diameter area, the center of which varied for different runs due to beam tuning. A running average of the beam converging point was calculated on an event by event basis. This location and the location reported by the working plane were used to reconstruct the tracks for the events in which one plane of the beam vertex failed to report the beam location. A χ^2 cut was applied to all the reconstructed tracks to reject the bad reconstructions caused by problems in the drift chambers.

2 Event Classification

2.1 Selection Procedure

We consider now the identification of specific channels using the P/Z measurement described above. Let us consider the selection of the 3p channel. The Z=11 candidates were first selected by the triple charge measurement. Figure 6.2 (a) shows the neutron calorimeter energy verses the reconstructed P/Z for Z=11 candidates. The isotopes such as 3p+^{25}Na, 3p+1n+^{24}Na and 3p+2n+^{23}Na which belong to the 3p group can easily be identified. Among the other groups we can identify possible candidates for 2p+1d+^{24}Na and 1p+1α+^{23}Na, which need further classification. Figure 6.2 (b)

shows the energy in proton calorimeters for selected Z=11 candidates (solid curve). It is impossible to decide where to put the cut on this spectrum to select 3 proton events. Note that although we require Z=11 for heavy ions, the channels with α or d in the final state will have only 1 or 2 protons deflecting into the proton calorimeters. The dashed line shows the 3p+Xn+^{Y}Na (where X=0-2 and Y=25-23) candidates selected by combining the P/Z and the neutron calorimeter energy for Z=11 candidates (ie. by requiring the correct neutron energy and the heavy ion P/Z for each isotope). This shows how clean channels can be selected even without the energy measurement in the proton calorimeters.

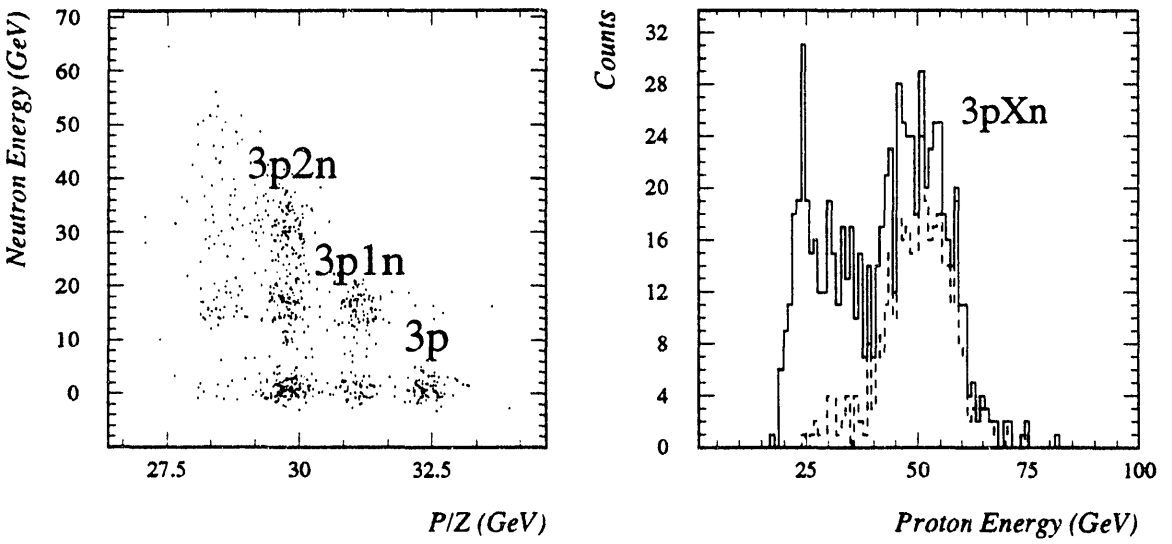

Figure 6.2: Selection of multi nucleon events. (a) Energy in neutron calorimeters vs. P/Z. (b) Energy in proton calorimeters for selected Z=11 events (solid curve) and selected Z=11 with cuts on neutron energy and the P/Z (dashed curve).

2.2 Selection of α and d Channels

The channels having α or d in the final state require an additional measurement to indicate their presence. The P/Z of these particles is very close to the P/Z of the heavy fragments accompanying them. In drift chambers, these particles traverse in the reduced gain region which is suitable for heavy ion fragments and only a very small percentage will leave recognizable tracks in the drift section as well as in the pad section. Hence, efficient track reconstruction is not possible for these particles.

A closer inspection shows that the vertical and the horizontal hodoscopes at the downstream end of the spectrometer can help us resolve this problem. The pattern recognition algorithm was developed to search for the second highest pulse height in either the vertical or the horizontal scintillation counters (after selecting the heavy ion fragment). Since the counters are perpendicular to each other, we can narrow the region in which the heavy ion and the secondary particle (α or d) overlap to an area

of about 10x10 cm^2. Figures 6.3 (a) and (b) show the measured second maximum pulse height for selected 1p+1d+^{23}Mg and 1p+1α+^{23}Na events. The second highest pulse height shows that particles with Z=1 and Z=2 (in this plot they are at 100 and 400) have traversed the scintillators, which indicates the presence of d and α. The cuts were applied on these distributions at 50 and 250 (only to reject low pulse heights), to select the d and α channels respectively.

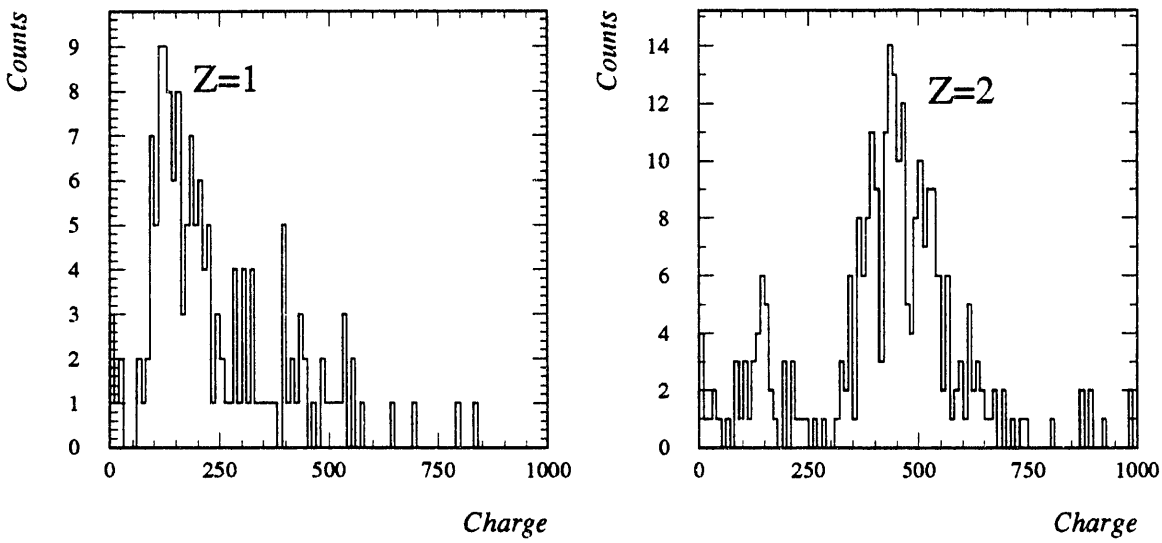

Figure 6.3: Second charge measurement at the downstream end of the spectrometer. (a) d channels. (b) α channels.

In order to confirm our identification of the complex final states, we look for collaborating evidence in the downstream calorimeters. Studies showed that for the selected events with d and α channels, the deflected beam region calorimeters on an average report an energy measurement higher than what we expect from the residual heavy ion. This indicated the presence of another particle in the same vicinity as the heavy ion fragment confirming our selection procedure. No requirements on the energy measurement was imposed due to the poor energy resolution in the deflected beam region calorimeters. However, one should bear in mind that the heavy ion usually creates δ rays which can be misidentified as the correct second highest pulse height in the forward scintillators. Hence the selection on d and α channels can be somewhat biased.

3 Results

3.1 Efficiencies

In addition to the efficiencies listed in Table 4.6, the major inefficiency for this analysis arises from the heavy ion reconstruction. This can be estimated for simple channels by selecting 1p+^{27}Al or 1n+^{27}Si with and without using the P/Z measurement since

these are very clean channels which can be analyzed without the P/Z measurement. For rare channels, $2p+^{26}Mg$ was used as the reference channel. It was found that the P/Z efficiency is almost the same for all the heavy ion fragments.

All α and d channels suffer due to the limited acceptance in the detectors. This inefficiency was estimated by using Monte-Carlo methods to simulate the decay of specific channels and by then estimating the number of events that fall outside the 10x10 cm^2 area. This estimation obviously depends on the available excitation energy for the decay since the opening angle between the heavy ion and the α or d depends on this energy. Figures 6.4 (a) and (b) show the estimated efficiency for $1p+1d+^{25}Mg$ and $1p+1\alpha+^{23}Na$ against the excitation energy used (open circles). An efficiency of 70% was used in this analysis for the acceptance corrections of all channels having α or d emissions.

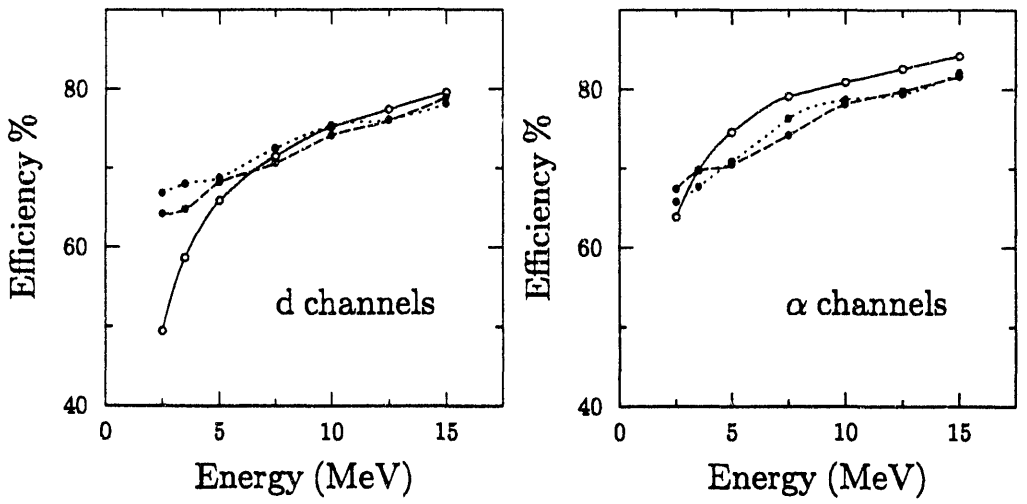

Figure 6.4: Efficiency of limited acceptance arising from the second charge measurement. Plots show the estimated efficiency variations for excitation energies up to 20 MeV. Each curve represents a specific decay channel having (a) d and (b) α particle in the final state.

The other efficiency factors arise from the performance of the calorimeters in detecting multinucleon events (which can be obtained by folding the efficiency to detect a single nucleon) and the trigger efficiencies for 2n and 3p triggers [1] due to the assigned thresholds. No acceptance corrections were needed for detecting peripheral protons or neutrons since the low P_T generated in the electromagnetic interactions does not deflect nucleons out of our detector acceptance limits. A list of estimated efficiencies is given in Table 6.1.

[1]The efficiency for the 2p trigger threshold is 100%

Table 6.1: Estimated efficiencies for selection of multi nucleon events.

Selection	Efficiency %
2n triggers	52.0 ±10.0
3p triggers	72.0 ± 5.0
P/Z reconstruction	85.2 ± 2.5

3.2 Cross Sections

The cross section calculations were carried out for each identified channel using the equation 4.1 given in chapter 4. The results for channels having neutrons and protons in the final state are given in Table 6.2 and the results for the channels with an α or a d in the final state are given in Table 6.3. These data are corrected for interactions outside of the target by subtracting the appropriately scaled rates of events observed with the empty target frame. The listed errors are only statistical.

Table 6.2: Measured exclusive EMD cross sections for channels having neutrons and protons in the final state. The listed errors are only statistical.

Channel	Pb (mb)	Sn (mb)	Cu (mb)	Al (mb)
1p	676.42±7.63	274.04±4.35	111.03±3.30	31.55±1.19
1n	241.03±4.18	100.01±2.00	40.42±1.67	13.11±0.59
1p1n	65.05±2.47	27.50±1.43	10.18±1.09	4.04±0.43
2p	74.69±0.80	34.36±0.47	13.09±0.24	4.32±0.12
2p1n	22.76±0.44	10.47±0.26	4.69±0.15	1.99±0.08
2p2n	5.95±0.23	2.95±0.14	1.54±0.08	0.66±0.04
2n	1.90±0.11	0.74±0.07	0.27±0.04	0.12±0.02
2n1p	3.45±0.15	1.64±0.09	0.76±0.05	0.34±0.03
3p	0.57±0.05	0.16±0.02	0.07±0.01	0.04±0.01
3p1n	0.82±0.06	0.39±0.03	0.15±0.02	0.10±0.01
3p2n	1.21±0.07	0.58±0.04	0.25±0.02	0.13±0.01
4p	0.011±0.006	0.002±0.002	–	–
4p1n	0.016±0.008	0.006±0.005	0.004±0.003	0.003±0.002
4p2n	0.109±0.018	0.053±0.011	0.025±0.006	0.015±0.004
4p3n	0.073±0.015	0.050±0.011	0.037±0.008	0.007±0.003

In Figure 6.5 (a), the measured EMD cross sections are displayed as functions of the Q_0 of the decay channel (open circles). The general trend of the data shows an exponential decrease with the increase in the value of Q. A difference is observed in the cross sections of the xp and yn channels. This is evident by the 2p and 2n cross sections given in the Table 6.2. The decay modes of the excited ^{28}Si nucleus in the

Table 6.3: Measured exclusive EMD cross sections for channels having d and α in the final state (in addition to the neutrons and protons). Listed errors are only statistical.

Channel	Pb (mb)	Sn (mb)	Cu (mb)	Al (mb)
1α	72±32	58±30	17±19	21±16
1p1α	24.69±1.74	10.16±1.00	5.83±0.90	2.00±0.36
1n1α	3.11±0.60	1.60±0.30	0.21±0.16	0.16±0.07
1p1n1α	7.37±1.00	1.97±0.46	1.63±0.51	0.71±0.22
2p1α	2.30±0.15	1.23±0.09	0.47±0.05	0.26±0.03
2p1n1α	2.61±0.15	1.14±0.09	0.66±0.06	0.27±0.03
2p2n1α	1.13±0.10	0.63±0.07	0.25±0.03	0.11±0.02
1p1d	20.07±1.57	8.56±0.91	4.14±0.76	1.39±0.30
1n1d	6.60±0.83	2.24±0.36	1.43±0.37	0.14±0.07
1p1n1d	5.40±0.86	3.05±0.57	2.73±0.65	0.95±0.25
2p1d	2.94±0.34	1.45±0.19	0.95±0.13	0.33±0.07
2p1n1d	3.12±0.35	1.76±0.21	0.93±0.13	0.28±0.06
2p2n1d	0.53±0.10	0.21±0.05	0.18±0.04	0.08±0.02

GDR region are discussed elsewhere [12, 13], where both statistical and non statistical decays are found. Assuming a purely statistical decay, calculations were performed to understand the general trend [19]. For these calculations, known photo-absorption cross sections were folded with virtual photon spectrums to obtain the excitation energy, and the simulation code CASCADE [21] was used to follow the subsequent decay of ^{28}Si. These results are shown in figure 6 (closed circles). The calculations show good agreement with the measured data. However, this comparison shows that in general, these calculations overpredict the proton emission cross sections and underpredict the neutron emission channels. In addition, the α emission channels which are purely statistical [12] decay channels show cross sections well below the calculated values.

The charge-changing cross sections previously measured at AGS energies [23] are shown in figure 6.5 (b) (closed circles). These cross sections define an upper limit to the cross sections we measure. Our measured cross sections which are shown in the same plot (open circles), agree well for all but ΔZ=4 which is expected since our exclusive cross sections do not contain all the decay channels. Here the α and d channels are also included in calculating semi-inclusive cross sections. No data were available in the above reference to compare with the 1n emission cross section.

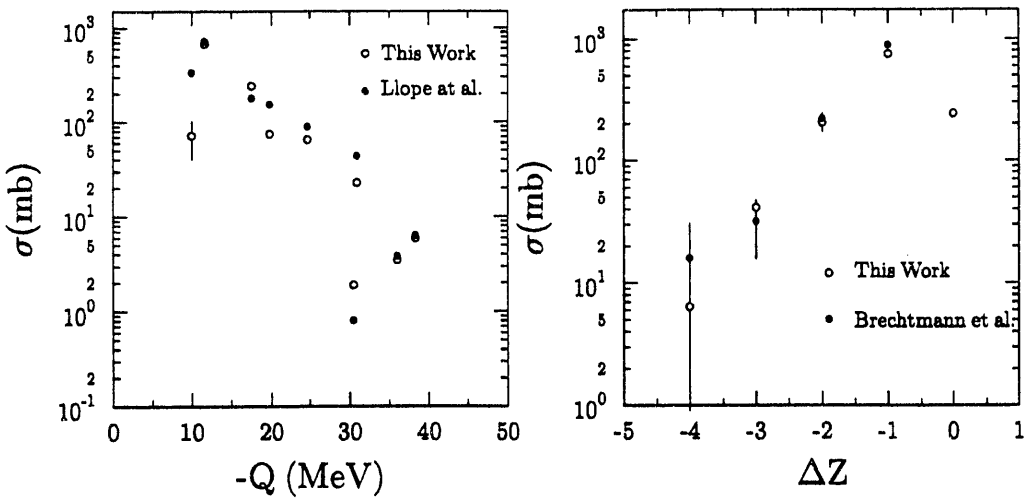

Figure 6.5: (a) Exclusive cross section vs. Q value of the reaction. (b) Total charge changing cross sections.

B Interpretation of the Data

1 Z and A Dependence

The production cross section was investigated as a function of the target, and this was used to characterize the nature of the reaction mechanism. The principal background to the EMD process is due to the soft nuclear induced fragmentation. The probability for these collisions is dependent on the target size while the probability for the EMD depends on the target charge. The measured single proton emission cross section as a function of the target charge for five different targets is shown in Figure 6.6. These cross sections show a strong charge dependence but do not show a simple Z_T scaling. A fit was performed on the data to obtain the dependence of the EMD cross sections on Z_T, assuming the following dependence of the cross section.

$$\sigma = a(A_T{}^{1/3} + A_P{}^{1/3}) + bZ_T^c \tag{6.1}$$

In the above equation, a, b and c are considered as three free parameters, and, A_T, A_P and Z_T represent the target mass, the projectile mass and the target charge respectively. The first term scales as the sum of the radii of the target and projectile mass. This is expected to describe the target dependence of the nuclear component. The second term scales as a power of the target charge and is expected to describe the target dependence of the electromagnetic component. The values of the parameters obtained from the fit are: $a = 1.39 \pm 0.20$, $b = 0.23 \pm 0.05$ and $c = 1.80 \pm 0.06$. Figure 6.6 shows the contribution of each term to the cross section. A non negligible contribution from the nuclear process for low Z targets is indicated by the results. However, due to severe biases introduced by the trigger and the analysis, the value

obtained for a by this fit cannot be taken as a measurement of the nuclear component of the cross section. The observed $Z^{1.8}$ dependence of the electromagnetic component agrees well with the values obtained in other EMD studies [18]. Although for low Z targets the nuclear component is substantial, the background to EMD for high Z targets is negligible. This opens up the possibility of meaningful detailed studies using kinematic reconstruction.

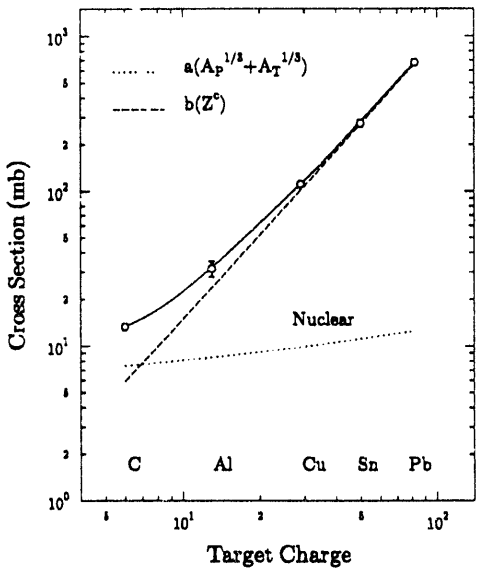

Figure 6.6: Z and A dependence of EMD cross sections for the ^{28}Si — ^{27}Al + 1p reaction. Solid curve represents the 3 parameter fit discussed in the text. Contributions of the extracted electromagnetic (dashed) and nuclear (dotted) components are also shown.

So far in this discussion, we have concentrated on the electromagnetic interactions which we claim do not produce any activity in the target region. In order to confirm our suspicion that events showing activities in the target region are indeed nuclear events, we examine whether they show the expected dependence on the target mass A_T. Two event samples were extracted from pre-selected nuclear events for the reactions 1p+1n+^{26}Al and 2p+1n+^{25}Mg by selecting P/Z and the charge Z of the heavy fragments. The events which show a correct number of protons but no neutrons (in this case a missing neutron) at the downstream end of the spectrometer were then selected. Figure 6.7 (a) shows the energy in the participant calorimeter for 1p+1n+^{26}Al events. This plot shows that the missing neutron at the downstream end has deflected into the participant calorimeter. The events with an energy of 2.5 GeV or above in the participant calorimeter were selected as a good sample for nuclear interactions. Figure 6.7 (b) shows the cross section dependence on the mass of the target for these selected nuclear events. The dashed lines are the best fit to the data with the dependence of $a(A_T{}^k + A_P{}^k)$ with a and k considered as free parameters. The value of k which is expected to be 0.33 was found to be 0.39±0.07 for the 1p1n channel and 0.46±0.08 for the 2p1n channel. Note that we cannot consider the given cross sections in Figure 6.7 as absolute nuclear cross sections since the selected samples

were triggered to select electromagnetic interactions at the trigger level. However, it is clear from this plot that nuclear events do show a strong target mass dependence.

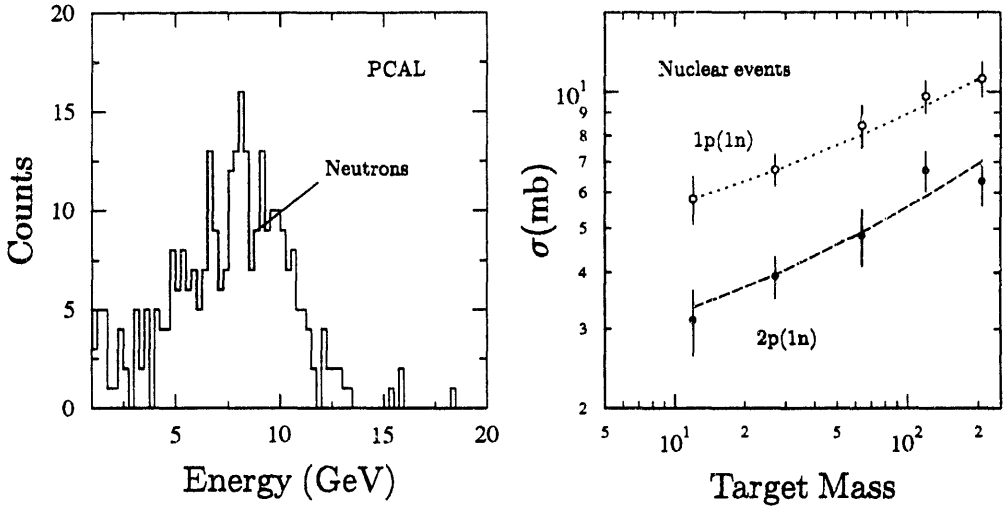

Figure 6.7: Selected nuclear events. (a) Measured energy in PCAL for missing neutrons. (b) Estimated cross sections. Dashed and dotted lines represent the expected behavior for a pure nuclear dependence.

2 Double Photon Excitations

In peripheral collision studies, one of the major goals is to see if we can identify the multi photon processes where the projectile absorbs two or more virtual photons from the same target nuclei [63, 64]. The simplest approach to this is to see if we observe any deviations from the $Z^{1.8}$ behavior. If two photons are absorbed by the projectile, the cross section should display a Z_T dependence which is close to Z_T^4. If the one photon processes are competing with the two photon processes, the Z_T dependence would not be too steep but it would still be steeper than 1.8.

The analysis to test the existence of multi photon excitations consists of extracting the Z_T dependence (exponent) of the EMD cross sections for all the available decay channels. The exponent was extracted by fitting the formula given in the previous section to cross sections for Pb, Sn, Cu and Al targets. Since the formula contains 3 free parameters and we have only 4 targets (except for simple channels), the fit does not have sufficient constraints (only 1 degrees of freedom) to do a precision measurement. Table 6.4 shows the extracted parameters for 15 decay channels.

Figure 6.8 (a) shows the graphical representation of the extracted exponents against Q_0 for all the reaction channels. Due to poor statistics, the χ^2 minimization failed to converge for some of the channels, and hence were not included in the plot. No real enhancement was observed close to 40 MeV.

Table 6.4: Extracted exponents by a 3 parameter fit.

Channel	Q_0 (MeV)	a (mb)	b (mb)	c exponent
1p	11.6	$(1.5\pm0.2)\times10^{+0}$	$(2.0\pm0.3)\times10^{-1}$	1.84 ± 0.03
1n	17.1	$(8.6\pm1.3)\times10^{-1}$	$(6.9\pm1.5)\times10^{-2}$	1.84 ± 0.05
1p1n	24.7	$(2.9\pm0.7)\times10^{-1}$	$(1.7\pm0.8)\times10^{-2}$	1.87 ± 0.12
2p	19.8	$(1.9\pm0.4)\times10^{-1}$	$(3.7\pm0.6)\times10^{-2}$	1.72 ± 0.03
2p1n	30.9	$(1.9\pm0.3)\times10^{-1}$	$(0.9\pm0.3)\times10^{-2}$	1.75 ± 0.07
2p2n	38.3	$(0.5\pm0.2)\times10^{-1}$	$(0.7\pm0.5)\times10^{-2}$	1.51 ± 0.15
2n	30.5	$(1.3\pm0.5)\times10^{-2}$	$(0.1\pm0.1)\times10^{-3}$	2.15 ± 0.25
2n1p	36.0	$(3.3\pm1.1)\times10^{-2}$	$(1.7\pm1.3)\times10^{-3}$	1.71 ± 0.17
3p	34.0	$(0.6\pm0.1)\times10^{-2}$	$(0.6\pm1.3)\times10^{-6}$	3.11 ± 0.52
3p1n	43.0	$(1.4\pm0.3)\times10^{-2}$	$(0.3\pm0.5)\times10^{-4}$	2.26 ± 0.33
3p2n	49.9	$(1.6\pm0.4)\times10^{-2}$	$(2.8\pm2.9)\times10^{-4}$	1.88 ± 0.24
4p	44.7	-	-	-
4p1n	53.6	$(0.4\pm0.3)\times10^{-3}$	$(0.3\pm1.4)\times10^{-7}$	2.91 ± 1.08
4p2n	58.8	$(2.0\pm1.0)\times10^{-3}$	$(0.2\pm0.5)\times10^{-4}$	1.98 ± 0.78
4p3n	69.1	-	-	-

A simple test enables us to measure the reliability of our fitting procedure in extracting the exponents. This is done by forcing the exponent to be 1.8 and repeating the exercise with 2 free parameters a and b. If we have enough sensitivity to extract the double photon excitation enhancement, and if our data truly support the idea, it should be reflected in the χ^2 probability distribution. It was found that both methods produce fairly flat distributions. This indicates that within our statistical accuracy, we cannot prove that the behavior of the data is other than $Z^{1.8}$.

Figure 6.8 (b) shows the ratio of the electromagnetic component to the soft nuclear component extracted by the 2 parameter fit for the decay channels. The ratio essentially gives us the contribution of the nuclear component to each peripheral channel. For higher Q values the nuclear component is large in comparison with the electromagnetic component. Unfortunately, this affects our fitting procedure since the nuclear component in the region $Q > 30$ is more than 25% of the total cross section.

3 Background to the Double Photon Excitation Process

A possible background to the double photon process could arise from the absorption of two single photons from two different target nuclei. A straightforward estimate can be made under the assumption that the cross sections for the removal of a few nucleons is roughly the same for the first and second interaction in the target material.

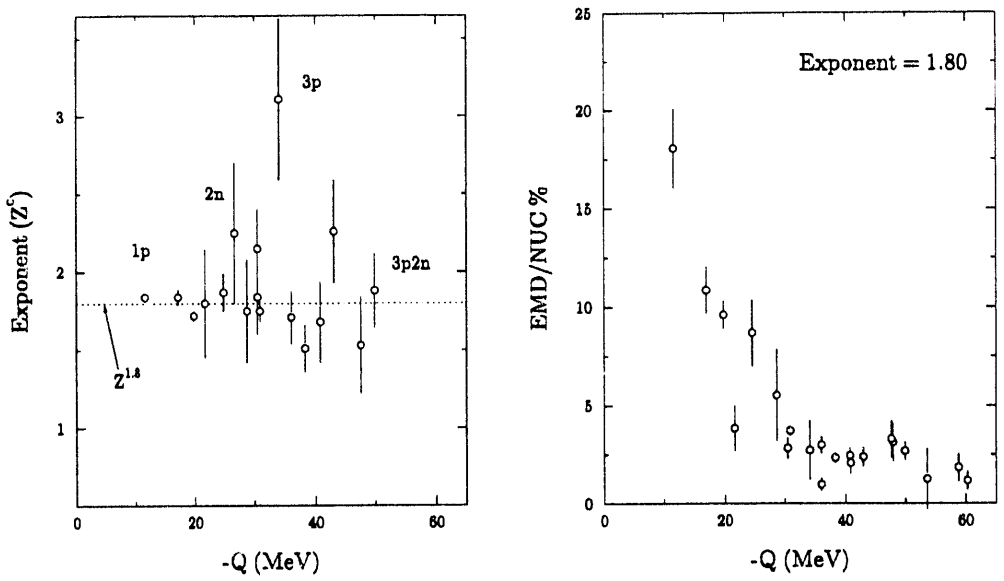

Figure 6.8: (a) Z dependence of cross sections extracted by the three parameter fit discussed in the text. (b) Ratio of nuclear and EMD components for different decay channels obtained with a fixed exponent.

For a target of thickness ℓ the flux of secondaries produced in a slice dx is given by:

$$dN = n\sigma N_0 dx$$

where, N_0 and σ are the original flux and the cross section respectively, for the first interaction. The constant n is the number density of the target nuclei.

The flux of produced particles after the second interaction in the target is given by:

$$dN' = n^2\sigma\sigma' N_0(\ell - x)dx$$

and the total yield is given by:

$$\frac{N'}{N_0} = \sigma\sigma'\frac{(n\ell)^2}{2}$$

If we generalize the above equation for multiple interactions, we would get:

$$\frac{N'}{N_0} = \left[\prod_{i=1}^{k}\sigma_i\right]\frac{(n\ell)^k}{k!}$$

where the σ_i's represent the cross sections for each interaction.

This formula allows us to evaluate the contribution of secondary interactions from two different nuclei, to the measured cross sections. Table 6.5 shows the percentage of the secondary interaction background of the measured cross sections for several

decay channels. Out of all possible combinations, the most effective decay branches were considered. It is assumed here that even after the first interaction the residual nucleus will respond to the subsequent interactions in the same manner as the original projectile. The last two columns show the extracted exponents before and after the corrections due to the double interactions. It is clear from these results that the effects of the secondary interactions do enhance the exponent. Therefore, significant contributions of this type can produce enhancements which can be misidentified as the double photon absorption since they are target dependent.

Table 6.5: Estimated double scattering contribution on the cross sections. Here, c_{old} and c_{new} represents the old and new (after correcting the cross sections for the double scattering) exponents.

Channel	-Q (MeV)	Pb%	Sn%	Cu%	Al%	c_{old}	c_{new}
1p1n	24.7	3.2	1.6	0.9	0.3	1.87	1.84
2p	19.8	3.9	1.8	1.0	0.3	1.72	1.69
2p1n	30.9	3.4	1.7	0.8	0.3	1.75	1.73
2p2n	38.3	3.3	1.6	0.7	0.3	1.51	1.48
2n	30.5	19.3	11.0	6.4	2.1	2.15	1.99
2n1p	36.0	5.7	2.7	1.1	0.5	1.71	-
3p	34.0	111.9	96.0	43.7	9.9	3.11	-
3p1n	43.0	31.2	16.0	9.2	2.3	2.26	1.69

C Excitation Energy Reconstructions

To generate excitation energy distributions and decay angular distributions in θ^* and ϕ^*, events that were used in the evaluation of the cross sections of 1p and 1n were processed as described in the previous chapter. The experiment E814 is not designed to measure the energy of the emitting photon when the residual nucleii decay to an excited state before reaching the ground state. As a result, the true excitation energy cannot be measured. The effect of such decays on the measurement are discussed here. We concentrate on the 1p emission channel primarily, and occasionally, when needed, 1n results are discussed.

1 Single Nucleon Emission

1.1 Excitation Energy Distributions

In Figures 6.9 (a) and (b), the raw excitation energy distributions of selected events produced for 1p and 1n emission channels on Pb, Sn, Cu and Al targets are shown. Corrections for interactions outside the target have been done on these data. A

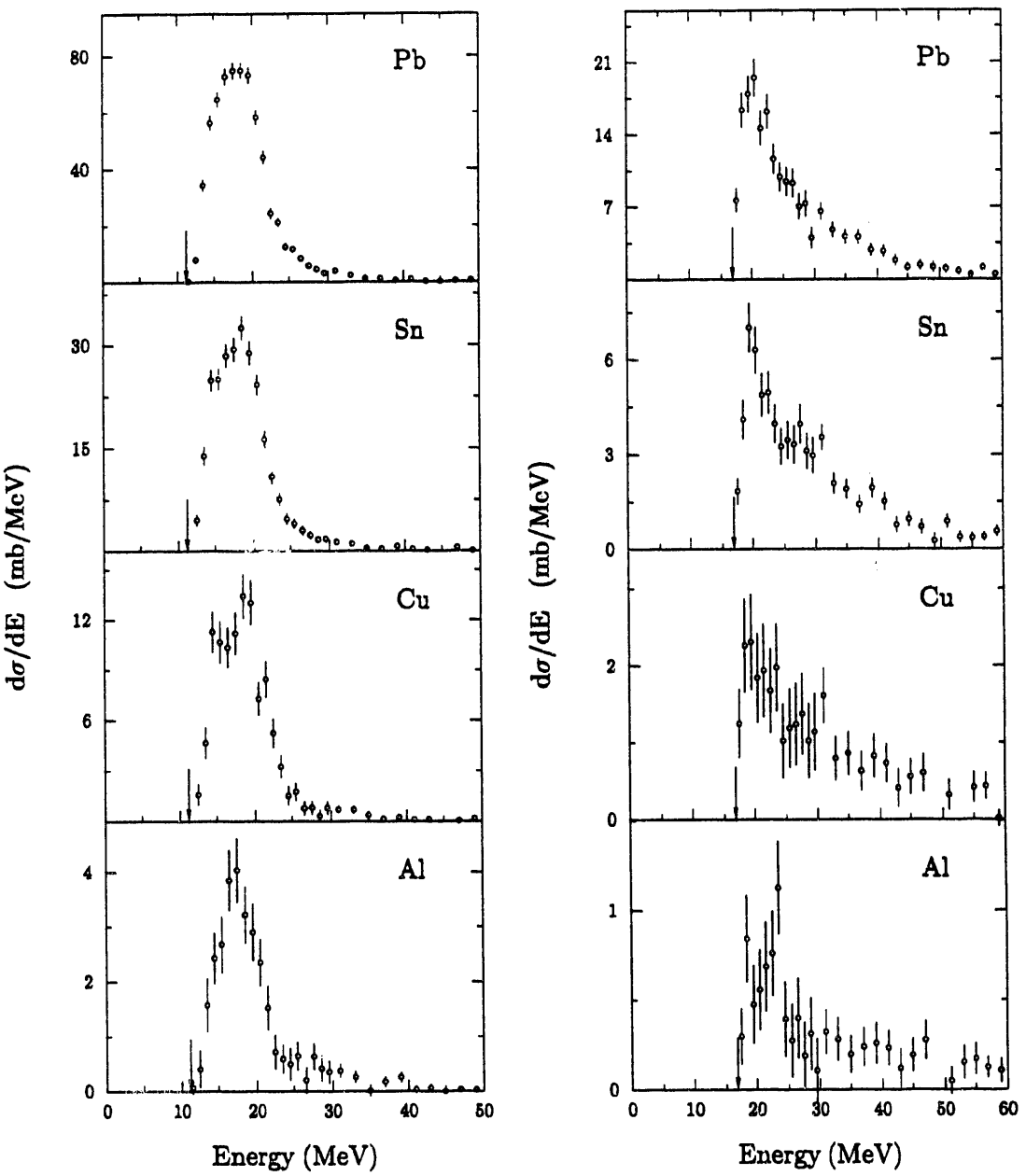

Figure 6.9: Reconstructed raw excitation energy spectra for 4 different targets. The arrows indicate the kinematic thresholds for each reaction. (a) 1p events. (b) 1n events.

correction of $\sim 5\%$ in Pb and $\sim 30\%$ in Al is obtained by the empty target subtraction. Our estimates of the experimental resolution in the invariant mass reconstruction discussed in chapter 5, section 3.2, is evident by the rapid rise of the data near the threshold.

A peak that is centered at about 18 MeV with a relatively narrow width of about 7 MeV is seen for all 1p distributions. These values can be compared with the values of peak position (20 MeV) and width (4.5 MeV) obtained for the GDR in ^{28}Si by the (γ,p) reactions [12, 13]. It should be noted that the virtual photon spectrum of the electromagnetic excitation process is not uniform and hence tends to enhance the low end of the GDR distribution. The decay to excited states in ^{27}Al produce a similar effect on these distributions.

For the 1n distributions the peak position and the width correspond to about 22 MeV and 5 MeV respectively. The available data obtained from the (γ,n) reactions [14] show a good agreement with our measurements. For 1n excitation, the threshold energy is already higher than the peak energy of the GDR and hence shows a sharp rise. The tail of the 1n distributions arises from events which are poorly reconstructed.

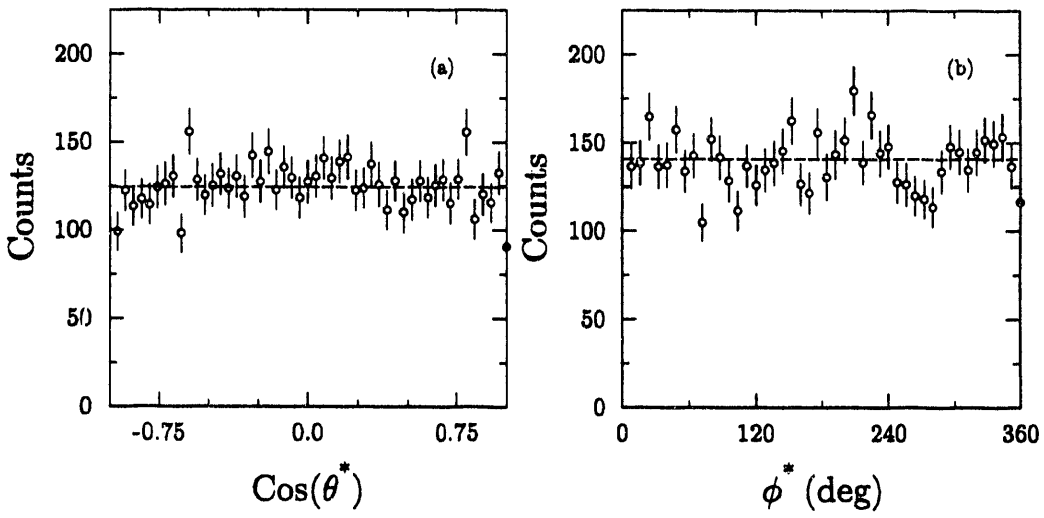

Figure 6.10: Decay angular distributions for reconstructed 1p events taken with a Pb target. The angles are the (a) polar (b) azimuthal center-of-mass angles of the ^{27}Al ion.

1.2 Angular Distributions

The polar (θ^*) and azimuthal (φ^*) center of mass angles of the ^{27}Al ions for the 1p emissions obtained from the kinematic reconstruction are presented in Figures 6.10 (a) and (b). Within statistics, both these distributions are very nearly isotropic (dashed lines) and symmetrical. This symmetry gives us confidence in the event reconstruction techniques used in this analysis. A detailed theoretical calculation of

the expected shape of the decay angular distribution is complicated by the decays proceeding to the excited states of the residual nucleus. However, the preference for emission perpendicular to the beam axis, which is suggested by Bertulani and Baur [11] for spinless projectiles and fragments are not observed in our data.

Due to the poor resolution in the energy and position measurements in the calorimeters, we are unable to extract the center of mass angles for the 1n distributions.

1.3 Ratios of Energy Spectra

By assuming that the process is factorizable, i.e. that the differential cross section is proportional to $N_\gamma \cdot \sigma(\gamma, p)$ where N_γ is related to the excitation mechanism, insight into the dependence of the reaction mechanism on the excitation energy, can be gained by using the ratios of the energy spectra for different targets. For example, if the excitation is purely nuclear, the obtained ratio should be proportional to the sum of the target and the projectile radii, whereas a purely electromagnetic excitation should give a ratio that scales with the target charge as a power of Z_T. For high Z targets, the ratios should be equal to the ratios of the calculated photon spectra since soft nuclear background makes a non negligible contribution.

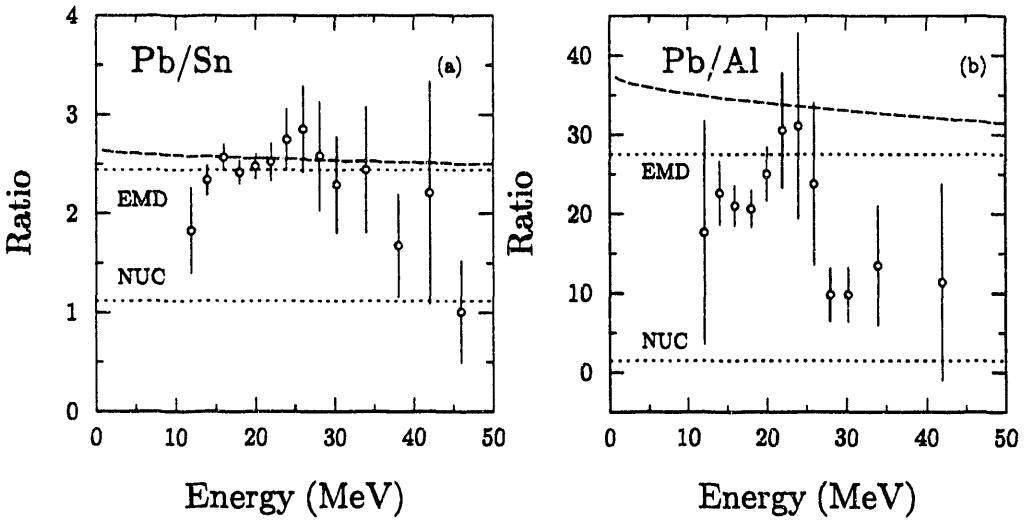

Figure 6.11: Ratio of excitation energy spectra for (a) Pb/Sn and (b) Pb/Al. Two dotted lines indicate the expected ratios for pure nuclear and pure electromagnetic dependence. Dashed lines represent the theoretical ratio obtained by the WW method.

The experimental ratios for Pb/Sn and Pb/Al compared with the ratios expected from the two terms EMD and nuclear (dotted lines) are shown in Figures 6.11 (a) and (b). The two terms are extracted from the fit performed on the integrated 1p cross sections which was discussed earlier. In addition, the ratios of the calculated photon spectra (dashed lines) for the same targets are shown in the figure. It is assumed in

the calculation of the photon spectra that the minimum impact parameter b_{min} is the sum of the target and the projectile radii:

$$b_{min} = 1.2(A_T^{1/3} + A_P^{1/3}).$$

The ratios near the GDR for the Pb/Sn are fairly consistent with the calculated ratio. This is not true for the Pb/Al targets. The experimental ratios obtained for the Pb/Al targets are much lower than the calculated values. At the high end of the energy spectrum (E > 25 MeV), the nuclear background is clearly the dominant process. The data also indicate some background at low excitation energies. Although the ratios of the calculated WW spectrum are consistently higher than the data, at least in the vicinity of the GDR, the ratio of the photon spectra agrees quite well with the data.

A similar behaviour was observed with the 1n data. An enhancement indicating the presence of DGDR in the experimental data for Pb/Al close to an excitation energy of 40 MeV was not observed in both the 1p and the 1n distributions.

1.4 Nuclear Background Subtraction

A technique similar to that used for the integrated cross sections was used to evaluate the contribution of the nuclear background as a function of the excitation energy. This is required since the decay channels originating from nuclear induced interactions and electromagnetic interactions cannot be distinguished on an event by event basis. To initiate this technique, an approximate experimental distribution for the nuclear component was obtained by assuming that the data from the Pb target has a negligible nuclear background (it was shown earlier that the Pb target nuclear contamination is only 2%). This method is applied on the 1p data.

The data in Figure 6.9 (a) were first rebinned into energy bins of width 2-4 MeV (see Table 6.6) to obtain sufficient statistical accuracy. The Pb data were then scaled by the factor $(Z_C/Z_{Pb})^{1.8}$ and subtracted from the data taken with the Carbon target (the excitation energy distribution for the C target is not shown in Figure 6.9). This produced the expected distribution of the nuclear induced component for the C target. This is is shown in Figure 6.12. It was found that a sum of a Gaussian and a Moyal function [2], each with three free parameters, fits this extracted distribution quite well. The function used is

$$f_{NUC} = X_1 e^{-\mu^2/2} + X_2 e^{-(\lambda + e^{-\lambda})/2}$$

in which $\mu = (E - X_3)/X_4$ and $\lambda = (E - X_5)/X_6$.

The procedure is to perform a fit of the following function to the entire data set:

$$d\sigma_k/dE = (A_T^{1/3} + A_P^{1/3}) f_{NUC} + Z^{1.8} C_k(E_k)$$

[2]The selection of these two functions does not have any scientific basis.

in which the 6 nuclear parameters (X_i) and 14 values of C_k (one for each value of the excitation energy E_k) are varied to minimize the χ^2 of the fit.

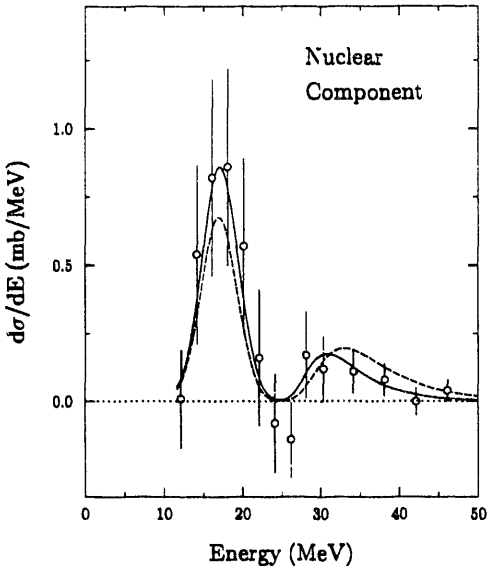

Figure 6.12: Estimated cross section distribution of the surviving nuclear induced component of the cross section for the C target, obtained by subtracting the raw Pb data, scaled by a factor $(Z_C/Z_{Pb})^{1.8}$, from the C data.

To test the method of separating the two components, a fit was performed on the data from the four targets Pb, Sn, Cu, and Al. These results were used to predict the nuclear component of the C data. To obtain sufficient accuracy in this test, it was necessary to represent C_k as a parametrized function. The same form used to represent f_{NUC}, was used to represents C_k in this test. The fit obtained for the above mentioned four targets, is given by the dashed curve in Figure 6.12. No data from the C target was used here. It is clear that the function f_{NUC} found in this fit is consistent with the nuclear component of the C data. This demonstrates the validity of the method. To achieve an optimal accuracy for this subtraction, the C data were included in the final fit. The solid line in Figure 6.12 represents the resulting nuclear component extracted from this fit. The χ^2 for this fit is 31.6 for 50 degrees of freedom. The fitted nuclear component from each of the data points of Figure 6.9 (a) were then subtracted to obtain the experimental EMD cross sections for each target.

Figure 6.13 gives the background-subtracted EMD final energy spectra for the Pb, Sn, Cu and Al targets. The effects of the nuclear excitation were as expected negligible for the heavier targets. The main effect for the Al target was the reduction of the cross section at the peak by approximately 20%, and the reduction of the high energy tail which was quite significant. The EMD component resulting from the fit is given in Table 6.6. Values of the nuclear component are also obtained from this fit, but since the trigger and the event selection procedure have already been applied to remove events of this nature, these cannot be considered as meaningful measurements for nuclear component.

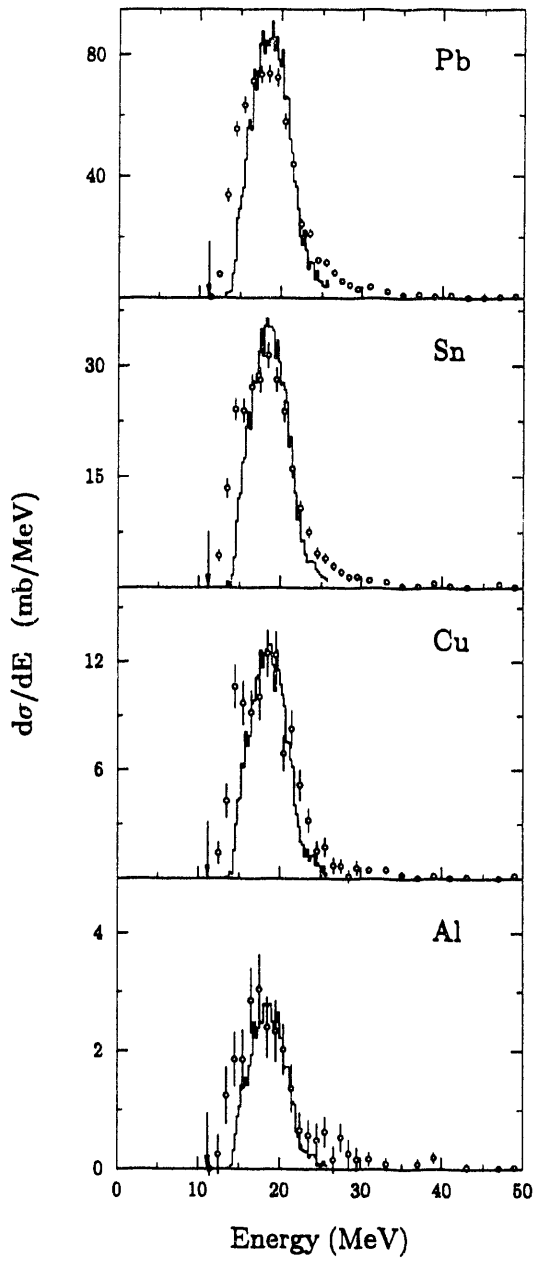

Figure 6.13: Nuclear component subtracted excitation energy spectra for reconstructed 1p events taken with 4 targets. The solid curves are obtained from (γ, p) experimental data multiplied by the WW spectrum and simulated through our apparatus. The arrows indicate the kinematic threshold of the reaction.

Table 6.6: Values of the cross section parameters C_k found in the final fit to the data taken with Pb, Sn, Cu, Al and C targets.

E_k(MeV)	$C_k(\mu b/MeV)$	E_k(MeV)	$C_k(\mu b/MeV)$
11-13	1.54 ± 0.20	25-27	3.36 ± 0.23
13-15	16.22 ± 0.51	27-29	1.69 ± 0.18
15-17	23.42 ± 0.61	29-32	1.16 ± 0.13
17-19	26.28 ± 0.64	32-36	0.56 ± 0.08
19-21	23.09 ± 0.58	36-40	0.31 ± 0.06
21-23	12.26 ± 0.40	40-44	0.18 ± 0.05
23-25	5.77 ± 0.29	44-48	0.09 ± 0.03

2 Comparison with Low Energy Data

2.1 Partial Cross Sections

Comparison of the results of this experiment with data from the photo-nuclear process is required to understand the properties of the virtual photon field. For this comparison, available data on the ^{28}Si(γ,p)^{27}Al reactions [12, 13] can be used. To predict the results expected in our experiment, the WW spectrum was combined with the photo-nuclear cross section measurements using a simulation program. For 1p distributions, this program uses experimental (γ,p) cross sections for ^{28}Si measured up to an energy of E_γ = 26.0 MeV. It takes into account the decay to excited states of ^{27}Al of energy up to 4.5 MeV [12]. The prediction is done as follows.

For each state in ^{27}Al, the (γ,p) differential cross sections are first multiplied with the virtual photon spectrum. This provides the effective final state yields as functions of the photon energy. These yields are then integrated over the photon energy and the resulting values are used to obtain effective branching ratios for each state. The excited state based on these ratios is selected, and a value for the photon energy is generated according to the strength distribution of the state being considered. The decay is assumed to be isotropic. As mentioned before, in the case of decay to an excited state of ^{27}Al, the energy of the proton is reduced, which results in the enhancing of the lower end of the observed excitation energy distribution. The simulation includes the effects of detector resolution and multiple scattering.

Although the invariant mass (which is the excitation energy of the p+^{27}Al system) is measured, the real excitation energy is the sum of the measured energy and the energy of any undetected decay photons from the ^{27}Al nucleus. It is possible to study the relationship between the two by using the simulation code. The expected excitation energy distribution for the calculation described above is shown in Figure 6.14. The sum of the energy of the decay photon and the excitation energy is also shown for comparison. The systematic uncertainty made in interpreting the measured energy as the excitation energy can be estimated by the difference between the two

curves. Only excited states of ^{27}Al of 4.5 MeV or lower are included in this simulation (since they are the only available states which we could find in the literature). The difference between the measured excitation energy and the true excitation energy will be affected by the existence of higher excited states, but for excitation energy values below 20 MeV in ^{28}Si, due to the Q value of the reaction, it is unlikely that states of energy above 4.5 MeV will be excited.

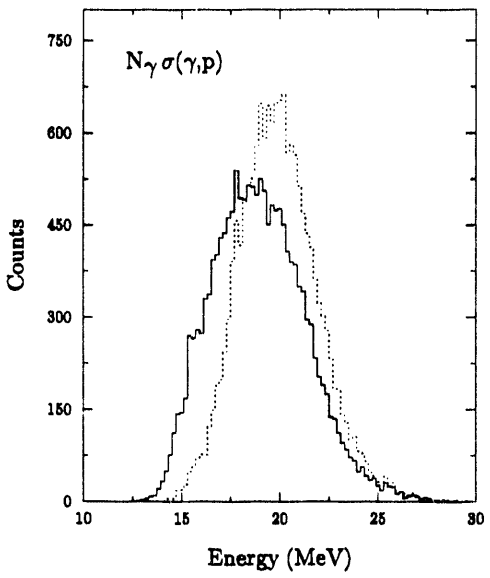

Figure 6.14: Monte Carlo simulation of the measured excitation energy distribution (solid curve) and the true excitation energy distribution (dashed curve), obtained by adding the energy of the decay photon to the measured energy. The calculation is for Pb target.

For comparison, the excitation energy curves obtained from the Monte Carlo simulation are displayed with the data in Figure 6.13. There are no adjustable parameters in this comparison. A comparison beyond 26.0 MeV cannot be made since the simulation, which uses the $\sigma(\gamma, p)$ cross section data are available only in the interval 15.4 - 26.0 MeV. The value obtained by integrating the simulated cross sections over the excitation energy in the interval 16.0-26.0 MeV agrees well with the data. They are shown in Table 6.7.

However, a small discrepancy in shape is observed at the low end of the excitation energy spectrums. By simulating the events using different detector alignments and resolutions, an attempt was made to understand whether this discrepancy was due to instrumental effects. Noticeable differences in the decay angular distributions were produced, but the excitation energy spectrum was insensitive to these changes. The observed discrepancy could be an indication of the inability to explain the excitation of the resonance with a simple WW approximation or, the effect of excited states of ^{27}Al above 4.5 MeV, as mentioned above.

A similar comparison was made between the reconstructed In results and the ^{28}Si(γ,n)^{27}Si data obtained from the reference [14]. Figure 6.15 shows the comparison

Table 6.7: Integrated cross sections in the interval 16.0 to 26.0 MeV. The errors for the simulation are deduced from the available $^{28}Si(\gamma,p)^{27}Al$ photo-absoption cross sections which are used as the input. Errors on the data are statistical.

Target	Data (mb)	Simulation (mb)
Al	20.3 ± 1.6	15 ± 4
Cu	91.4 ± 3.7	72 ± 20
Sn	230.0 ± 4.9	203 ± 55
Pb	581.2 ± 8.3	515 ± 141

for the Pb target. No attempt was made to subtract the nuclear component from the 1n data since it has very little affect on the Pb target (only 2% nuclear contamination). The agreement between our results and the low energy data is satisfactory, showing a similar excess at the upper end of the curve as it seen for the 1p data. The tail out to higher energies (> 40 MeV) is a result of poor reconstruction for 1n events.

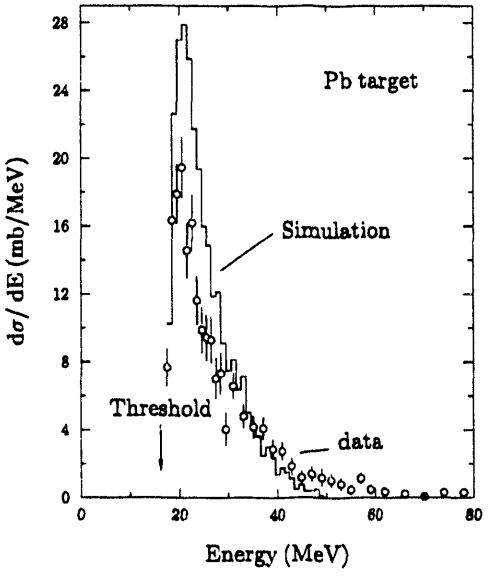

Figure 6.15: Excitation energy for 1n decay (closed circles). The solid curve represents the (γ,n) multiplied by the WW spectrum and convoluted with our experimental resolution. Arrows indicate the kinematic thresholds.

2.2 Verifications of the Total Cross Section Scale

The fragmentation of ^{28}Si at 14.6 GeV/nucleon was previously measured by using plastic nuclear track detectors [23]. These measurements report a total charge changing cross section value of 1190±170 mb since they measured $\Delta Z \geq 1$, missing the 1n cross section. If we correct for this effect, the total EMD cross section will be

1430±180 mb. The integrated EMD from Weizsäcker Williams is 1500 mb which is in very good agreement with the measured data.

From the beam trigger tapes, we measure 1410±100 as the total EMD cross section. This number is an upper limit on all the cross sections we can obtain. The error is quite large due to the poor statistics in the beam trigger tapes. If we add together the cross sections given in Tables 6.2 and 6.3, we obtain about 1250 mb, in agreement with the expected value. The cross section measured for 1p, 1n and 2p channels result in about 1000 mb which is about 70% of the total cross sections. Since we can reconstruct 1p, 1n and 2p channels, we can use the sum of these to compare with the total cross sections measured. Reconstruction of the 2p channel is not part of this thesis, but a precision measurement of this process has been carried out within the collaboration. We use these results only for the present cross section discussion.

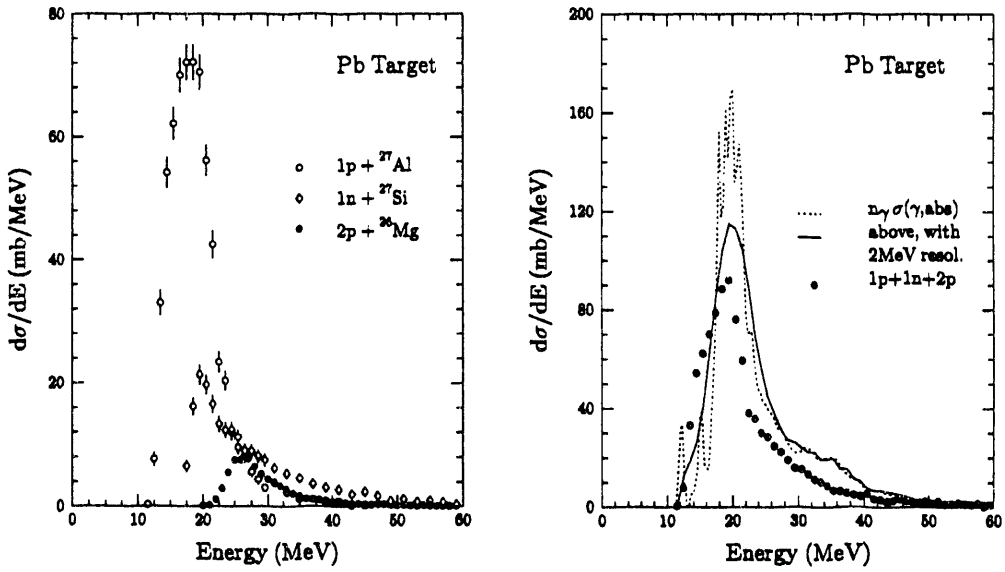

Figure 6.16: (a) Excitation energy distributions of 1p, 1n and 2p decay. (b) Sum of the three distributions compared with (γ.abs) spectra.

Figure 6.16 (a) shows the measured 1p, 1n and 2p excitation energy distributions for the Pb target. Although the distributions rise at different locations due to different thresholds, they agree remarkably well at the trailing edge of the GDR. Figure 6.16 (b) shows the measured total absorption cross section compared with our reconstructed sum of 1p, 1n and 2p distributions. The total absorption cross section curve is convoluted with our resolution. Although we measure only 70% of the total cross section by these three channels, the agreement is quite good.

CHAPTER 7

Conclusions

This work presents the results of an experimental investigation of the electromagnetic dissociation of 14.6 GeV/nucleon ^{28}Si ions. Exclusive cross section measurements for a large number of decay channels and excitation energy reconstruction for two simple decay channels having a single proton and a single neutron in the final state are studied. The reconstruction methods and techniques developed here can be extended to more complex channels quite easily.

In the past, the electromagnetic component was obtained by subtracting the hadronic contribution from the integrated total cross sections, using estimated values based on the concept of limiting fragmentation. Recent experiments, including experiment E814, have used the information from the production of secondary particles to reject the hadronic background electronically. It has been shown here that such techniques are very useful in suppressing the nuclear background and enabling the study of complex electromagnetic dissociation decay channels.

The measured cross sections presented here are in good agreement with those measured previously [31] with the E814 apparatus. Because the two experimental setups differ considerably, particularly in the detectors used to veto nuclear events, the agreement of the two results indicates that the event selection procedure and efficiency estimates are reliable. The observed dependence of the measured cross sections on the target charge Z_T and target mass A_T indicate the electromagnetic nature of the excitation mechanism. The measured cross section ratio $\sigma(\gamma,p)/\sigma(\gamma,n)$ is 2.7±0.7 for E_γ up to 30 MeV [14]. We observe a ratio of 2.81±0.21 for the Pb target and 2.41±0.18 for the Al target indicating a excitation of GDR in ^{28}Si. The measured semi-inclusive cross sections agree well with the previously measured charge changing cross sections [23]. These measurements were obtained by detecting only the heavy fragment and hence set an upper limit to our data. All cross sections show an approximate $Z_T^{1.8}$ behavior which is well reproduced by the WW approximation. The contribution due to the hadronic processes tends to increase for decay channels with higher Q values.

The excitation energy distributions of the decay channels ^{28}Si → 1p+^{27}Al and ^{28}Si → 1n+^{27}Si were reconstructed with geometrically and kinematically constrained fits. With the E814 apparatus, the former was reconstructed with 3 geometrical constraints and 2 kinematical constraints, whereas the latter was reconstructed with 1

geometrical constraint and 1 kinematical constraint (neglecting the energy measurement). Results show that the reconstruction techniques provide a resolution of 0.6-1.1 MeV (depending on the target) for 1p events and $\approx$ 2.0 MeV for 1n events (at $\sim$ 20 MeV of excitation energy) in the invariant mass reconstruction. Center of mass angles for 1p decay were reconstructed to an accuracy of a few degrees. The resolution in both energy and angle is dominated by multiple scattering in the target. Poor resolution in the energy measurement in the calorimeters prevents the reconstruction of angular distributions for 1n decay with good precision.

The soft nuclear-induced background to the EMD in the final state energy distributions for 1p decay was evaluated by representing this component with a simple functional form, whose parameters were determined by a fit to the data for all targets. The effect of the nuclear contribution was negligible for high Z targets, but was substantial for low Z targets. However, the parameters obtained for the nuclear component cannot be taken as meaningful measurements of the nuclear component of the cross section since the trigger and the selection procedure introduce severe biases to this process. The resulting EMD spectrum was compared with the results of a simulation based on a folding of the WW virtual photon spectrum produced by the targets with the inverse photonuclear process ^{28}Si(γ,p)^{27}Al. In general, the agreement is satisfactory, but some discrepancy is observed at low final state energies. A similar effect has been seen in the data on the EMD of ^{16}O at lower beam energies [22]. The same technique can be used to subtract the nuclear-induced background in the 1n excitation energy distributions.

A possibility for two photon excitations in EMD was investigated with a simple parametrization given by equation 6.1. The theoretical calculations suggest that the ratio of single photon excitation to double photon excitation in ^{28}Si at 14.6 GeV/nucleon is extremely small. In addition, successive one photon excitations for two different target nuclei can induce the same signatures as 'real' double photon excitations for a single nuclei. It has been shown that for some decay channels (for example the 3p emission channel) this makes a substantial contribution to the integrated cross section. The extracted parameters indicate that our data provide no evidence for the DGDR excitations in ^{28}Si. The ratios of excitation energy distributions for ^{208}Pb/^{27}Al and ^{208}Pb/^{120}Sn show a similar behavior. The ratios agree quite well with the expected behavior of the WW approximation. However, Q values above 30 MeV ratios show large deviations from the expected WW calculations which indicates that nuclear processes are substantial in this region. This in itself makes observations of DGDR very difficult through a total cross section measurement since the hadronic contribution becomes large in the region where we expect to observe signatures of DGDR.

There are obvious shortcomings in our experiment. We have a substantial inefficiency in detecting particles emitted at angles between 45° and 180° which are covered by the target calorimeter. The estimated leakage of this detector is roughly 50%. Efficiency in U/Cu calorimeters are not very good, especially in the region where the

neutrons are detected (about 90%). This is caused by having two calorimeter modules aligned at the center of the neutron distribution. This makes it extremely difficult to obtain clean samples of events for the reconstruction. in all exclusive EMD decay channels. Poor resolution in the U/Cu calorimeter energy and position measurements too do not allow us to reconstruct neutron channels with good precision. Studies have shown that by reconstructing residual heavy ions to a much higher degree than what is achieved in this thesis. this problem can be eliminated up to some extent. We cannot detect the de-excited γ rays emitted by the excited nucleus which can have a tremendous effect on observing DGDR excitations. In addition. multiple scattering in the target medium contributes substantially to the final reconstruction resolution. This can be easily avoided by using thin targets which would in addition reduce the contribution due to the double interaction background.

In spite of these short comings. the present work has shown that at relativistic energies it is possible to measure the properties of excited heavy ion projectiles with a resolution that is good enough to probe their structure. Other nucleii and decay channels can be studied using the techniques given here. For example. the collective states in the continuum of unstable nuclei. and the existence of collective strength at high excitation energies which are above the GDR can be explored using these techniques. In addition. by using the precision kinematic reconstruction of exclusive channels. it is possible to study the correlation of final states containing identical particles.

REFERENCES

[1] D.L. Olson at el., "Electromagnetic Dissociation of Relativistic ^{18}O Nuclei" *Phys. Rev. C* 24, 1529 (1981).

[2] M.T. Mercier et al., "Electromagnetic Dissociation of ^{59}Co, ^{89}Y and ^{197}Au Targets by Relativistic Heavy Ions to Z = 26" *Phys. Rev. C* 33, 1655 (1986).

[3] J.C. Hill et al., Electromagnetic Dissociation of ^{39}Co and ^{197}Au Targets by Relativistic ^{139}La Projectiles" *Phys. Rev. C* 38, 1722 (1988).

[4] J.C. Hill et al., "Two-Neutron Emission from Electromagnetic Dissociation of ^{59}Co and ^{197}Au Targets by Relativistic Heavy Ions" *Phys. Rev. C* 39, 524 (1989).

[5] T. Kobayashi et al., "Electromagnetic Dissociation and Soft Giant Dipole Resonance of the Neutron-Dripline Nucleus ^{11}Li" *Phys. Lett B* 232, 51 (1989).

[6] H. Takai, "Electromagnetic Dissociation and Projectile Fragmentation of Relativistic heavy Ions" *International Jour. Modern Phys.* (to be published).

[7] K. Goulianos, "Diffractive Interactions of Hadrons at High Energies" *Phys. Rep.* 101, 169 (1983).

[8] W.E. Frahn, "Diffraction Scattering of Charged Particles" *Anna. Phys.* 72, 524 (1972).

[9] H.R. Blieden, Measurement of Small-Angle Elastic Scattering of Pions and Protons by Nuclei" *Phys. Rev. D* 11, 14 (1975).

[10] J.D. Jackson, "Classical Electrodynamics", *Wiley* (1974).

[11] C.A. Bertulani and G. Baur, "Electromagnetic Processes in Relativistic Heavy Ion Collisions", *Phys. Rep.* 163, 299 (1988).

[12] R.L. Gulbranson et al., "Charged Particle Decay of the ^{28}Si Giant Electric Dipole Resonance" *Phys. Rev. C* 27, 470 (1983).

[13] E. Kerkhove et al., "Charged Particle Decay of ^{28}Si Induced by Quasi-Monochromatic Annihilation Photons in the GDR" *Nucl. Phys.* A474, 397 (1987).

[14] R.E. Pywell et al., "Photoneutron Cross Sections for the Silicon Isotopes" *Phys. Rev. C* 27, 960 (1983).

[15] C.J. Benesh et al., "Single Nucleon Removal in Relativistic Nuclear Collisions" *Phys. Rev C* 40, 1198 (1989).

[16] J.W. Norbury, "Charge Dependence and Electric Quadrupole Effects on Single-Nucleon Removal in Relativistic and Intermediate Nuclear Collisions" *Phys. Rev C* 42, 2259 (1990).

[17] J.W. Norbury, Electric Quadrupole Excitations in Relativistic Nucleus-Nucleus Collisions" *Phys. Rev C* 42, 711 (1990).

[18] D. Lissauer and H. Takai, "Z Dependence of Coulomb Dissociation Cross Section in Heavy Ion Reactions" *Phys. Rev. C* 41, 2410 (1990).

[19] W.J. Llope and P. Braun-Munzinger, "Electromagnetic Dissociation of Relativistic Heavy Ions" *Phys. Rev. C* 41, 2644 (1990).

[20] W.J. Llope, "The Dissociation of Relativistic Nuclei", *Ph.D. Thesis*, SUNY at Stony Brook, (1992).

[21] R. Schmidt et al., "Double Giant Dipole Resonance in ^{136}Xe" *Phys. Rev. Lett* (Submitted).

[22] D.L. Olson et al., "Direct Observation of the Giant Dipole Resonance of ^{16}O via Electromagnetic Dissociation" *Phys. Rev. C* 44, 1862 (1991).

[23] C. Brechtmann et al., "Fragmentation Cross Sections of ^{28}Si at 14.6 GeV/nucleon" *Phys. Rev. C* 39, 2222 (1989).

[24] J. Stachel and G. Young, "Relativistic Heavy Ion Physics at CERN and BNL" *Anal. Rev. Nucl. Part. Sci.* 42, 237 (1992).

[25] P. Braun-Munzinger et al., "Study of Extremely Peripheral Collisions and of the Transition from Peripheral to Central Collisions in Reactions Induced by Relativistic Heavy Ions", *E814 proposal submitted to the AGS committee* 56 (1985).

[26] J. Sandweiss et al., "Search for Strange Matter and Antinuclei in E814", *E814 proposal submitted to the GAS committee* (1988).

[27] P. Braun-Munzinger et al., "Transverse Energy Distrubutions in Si-nucleus Collisions at 10GeV/nucleon", *Z. Phys. C* 38, 45 (1988).

[28] J. Barrette et al., "Energy Flow and Stopping in Relativistic Heavy-Ion Collisions at $E_{lab}/A = 14.6$ GeV", *Phys. Rev. Lett.* 64, 1219 (1990).

[29] J. Barrette et al., "Forward Baryons in Relativistic Nucleus-nucleus Collisions", *Phys. Rev. C* 45, 819 (1992).

[30] J. Barrette et al., "Charged Particle Multiplicity in ^{28}Si+Al, Cu and Pb Reactions at E_{lab}/A = 14.6 GeV", *Phys. Rev. C* 46, 312 (1992).

[31] J. Barrette, et al., "Electromagnetic Dissociation of ^{28}Si at E_{lab}/A = 14.6 GeV by Nucleon Emission", *Phys. Rev. C* 41, 1512 (1990).

[32] J. Barrette et al., "Electromagnetic Dissociation of Relativistic ^{28}Si into p+^{27}Al", *Phys. Rev. C* 45, 2427 (1992).

[33] J. Barrette et al., "Production of Neutron-rich Isotopes from the Fragmentation of ^{28}Si Projectiles at P_{lab} = 14.6 GeV/c per nucleon", *Phys. Rev. C* (to be published).

[34] F.S. Rotondo, "Limits on Strange Quark Matter Production" Ph.D. Thesis Yale University (1991).

[35] J. Barrette et al., "Search for Strange Quark Matter in High Energy Heavy Ion Collisions", *Phys. Lett. B* 252, 550 (1990).

[36] J. Barrette et al., "Antiproton Production in Relativistic Si-Nucleus Collisions", *Phys. Rev. C* (to be published).

[37] H. Takai and W.E. Cleland, "Trigger Processor for Experiment 814", *E814 note* 32 (1988).

[38] R.M. Sternheimer, "Methods of Experimental Physics", *Academic Press* Vol. 4A (1961).

[39] P.V. Vavilov, "Ionization Losses of High-Energy Heavy Particles", *Sovi. Phys. JETP* 5, 749 (1957).

[40] G.D. Badhwar, "Calculation of the Vavilov Distribution Allowing for Electron Escape from the Absorber", *Nucl. Inst. Meth.* 109, 119 (1973).

[41] J.H. Adams et al., "Calculation of the Vavilov Distribution", *Nucl. Inst. Meth.* 124, 551 (1975).

[42] T. Akesson et al., "Properties of a Fine-Sampling Uranium-Copper Scintillator Hadron Calorimeter", *Nucl. Inst. Meth.*, A241, 17 (1985).

[43] T. Akesson et al., "Performance of the Uranium/Plastic Scintillator Calorimeter for the HELIOS Experiment at CERN", *Nucl. Inst. Meth.*, A262, 243 (1987).

[44] M. Fatyga et al., "Fast Monte Carlo Simulation of Segmented U/Cu/Scint Calorimeter", *Nucl. Inst. Meth.*, A284, 323 (1989).

[45] R. Debbe et al., "A Study of Wire Chambers with Highly Segmented Cathode Pad Readout for High Multiplicity, Charged Particle Detection", *IEEE Trans. Nucl. Sci.*, NS-37, (1990).

[46] J. Fischer et al., "A Many Particle-Tracking Detector with Drift Planes and Segmented Cathode Readout", *IEEE Trans. Nucl. Sci.*, NS-37 (1990).

[47] M.H. Salamon et al., "Plastic Scintillator response to Relativistic Ne, Ar, Fe Ions" *Nucl. Inst. Meth.* 195, 557 (1982).

[48] R. Dwyer et al., "Plastic Scintillator response to Relativistic Nuclei Z≤28" *Nucl. Inst. Meth.*, A242, 171(1985).

[49] J.B. Birks, "The Theory and Practice of Scintillation counting" *Macmillan*, NY, (1964).

[50] T. Tanimori et al., "A test of 150x20cm^2 wide time of flight scintillation counters" *Nuc. Inst. Meth.*, 216, 57(1983).

[51] T. Sugitate et al., "100cm long time of flight scintillation counters with rms resolution 50ps" *Nuc. Inst. Meth.*, A249, 354(1986).

[52] R. Wigmans et al., "On the Energy Resolution of Uranium and other Hadron Calorimeters" *Preprint Number* CERN/EP 86-141 (1986).

[53] J.P. Dishaw, "The Production of Neutrinos and Neutrinos-like Particles in Proton-Nucleus Interactions" *SLAC Report*, 216, March (1979).

[54] T. Ferbel, "Experimental Techniques in High Energy Physics" *Addison-Wesley Publishing Co.* (1987).

[55] B. Yu, "Gas Proportional Detectors with Interpolating Cathode Pad Readout for High Track Multiplicities" *Ph.D. Thesis*, University of Pittsburgh (1991).

[56] H. Wind, "In Formulae and Methods in Experimental Data Evaluation" *European Phys. Soci.* Vol 3, Chap k (1984).

[57] G. Conforto et al., "A Measurement of the β-parameter in the Charged Nonleptonic of the Λ^o Hyperon" *Nucl. Phys.* B40, 221 (1972).

[58] J.J. Russell et al., "Observation of Muon Trident in Lead and the Statistics of the Muon" *Phys. Rev. Lett.* 26, 46 (1971).

[59] E. Arik et al., "Y^* Production in Σ-Nucleus Reactions" *Phys. Rev. Lett.* 38, 1000 (1977).

[60] W.E. Cooper et al., "Studies in the BNL Negative 21 GeV/c Hyperon Beam I: Σ and Ξ Production Asymmetry in the Decay $\Xi^- \rightarrow \Lambda\pi^-$" *Phys. Rev. D* 21, 12 (1980).

[61] A.H. Wapstra and K. Bos. "Atomic Data and Nuclear Data Tables" Vol 19, 177 (1977).

[62] G. Lutz. "Optimum Track Fitting in the Presence of Multiple Scattering" *Nucl. Inst. Phys. Res.* A273, 349 (1988).

[63] G. Baur. "Multiple Electromagnetic Dissociation with Relativistic Heavy Ions" *Z. Phys. A* 332, 203 (1989).

[64] G. Baur and N. Baron. "Studies on Multiple Electromagnetic Excitation with Fast Heavy Ions: Scaling Properties for the Excitation of Rotational-Vibrational States" *J. Phys. G* 15, 661 (1989).

[65] L. Gonzaga et al., Covariant Formulation of Coulomb Excitation in Heavy Ion Collisions at Untra-Relativistic Energies" *Nucl. Phys.* A499, 837 (1989).

[66] D. Galetti et al., "A QED Description of Relativistic Coulomb Excitation in Heavy Ion Collisions" *Anna. Phys.* 177, 229 (1987).

[67] L.W. Townsend et al., "Calculations of Hadronic Dissociation of ^{28}Si Projectile at 14.6A GeV by Nucleon Emission" *Phys. Rev. C* 43, R2045 (1991).

[68] C. Brechtmann and W. Heinrich. "Fragmentation Cross Sections of ^{32}S at 0.7, 1.2 and 200 GeV/nucleon" *Z. Phys. A* 331, 463 (1988).

[69] C. Brechtmann and W. Heinrich, "Fragmentation Cross Sections of ^{16}O at 60 and 200 GeV/nucleon" *Z. Phys. A* 330, 407 (1988).

END

DATE FILMED

5/13/93